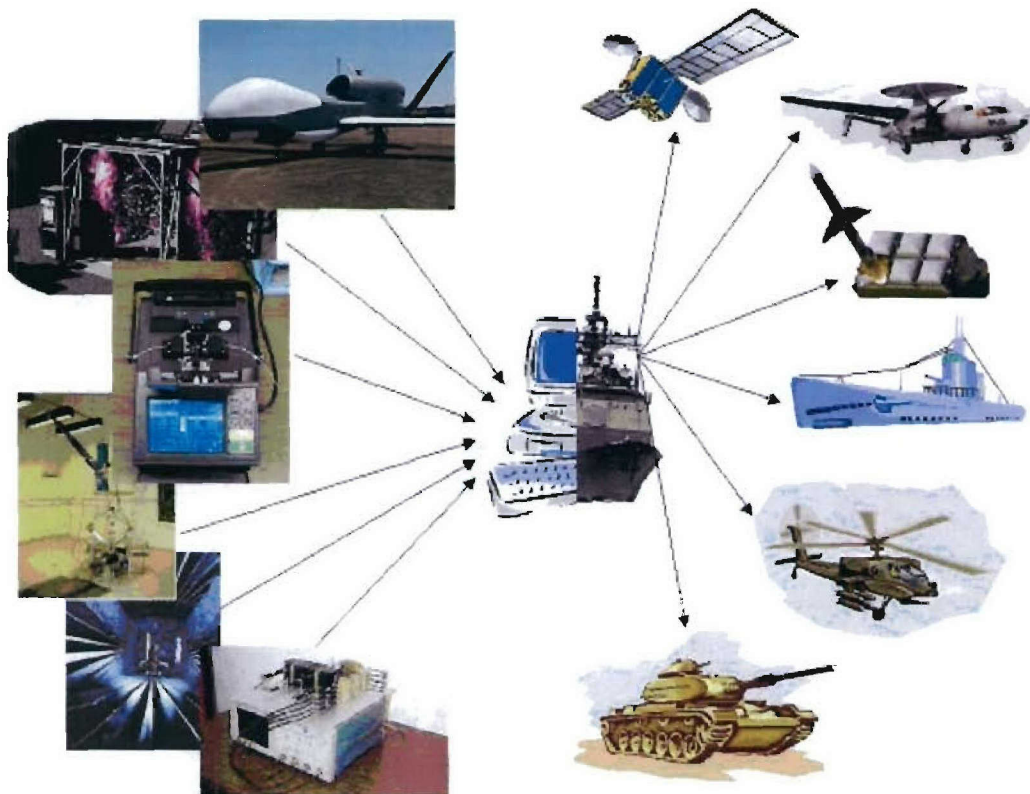


REPORT DOCUMENTATION PAGE				Form Approved OMB No. 0704-0188	
<p>The public reporting burden for this collection of information is estimated to average 1 hour per response, including the time for reviewing instructions, searching existing data sources, gathering and maintaining the data needed, and completing and reviewing the collection of information. Send comments regarding this burden estimate or any other aspect of this collection of information, including suggestions for reducing the burden, to Department of Defense, Washington Headquarters Services, Directorate for Information Operations and Reports (0704-0188), 1215 Jefferson Davis Highway, Suite 1204, Arlington, VA 22202-4302. Respondents should be aware that notwithstanding any other provision of law, no person shall be subject to any penalty for failing to comply with a collection of information if it does not display a currently valid OMB control number.</p> <p>PLEASE DO NOT RETURN YOUR FORM TO THE ABOVE ADDRESS.</p>					
1. REPORT DATE (DD-MM-YYYY) December 31, 2005		2. REPORT TYPE Quarterly Report		3. DATES COVERED (From - To) 1 Oct. to 31 Dec. 2005	
4. TITLE AND SUBTITLE Advanced Wireless Integrated Navy Network (AWINN)				5a. CONTRACT NUMBER N00014-05-1-0179	
				5b. GRANT NUMBER N00014-05-1-0179	
				5c. PROGRAM ELEMENT NUMBER	
				5d. PROJECT NUMBER	
6. AUTHOR(S) Warren Stutzman and Rick Habayeb				5e. TASK NUMBER	
				5f. WORK UNIT NUMBER	
7. PERFORMING ORGANIZATION NAME(S) AND ADDRESS(ES) Virginia Polytechnic Institute and State University Electrical and Computer Engineering Department 302 Whittemore Hall (0111) Blacksburg, VA 24061				8. PERFORMING ORGANIZATION REPORT NUMBER 4	
9. SPONSORING/MONITORING AGENCY NAME(S) AND ADDRESS(ES) Office of Naval Research ONR 313 875 N. Randolph St. Arlington, VA 22203-1995				10. SPONSOR/MONITOR'S ACRONYM(S)	
				11. SPONSOR/MONITOR'S REPORT NUMBER(S)	
12. DISTRIBUTION/AVAILABILITY STATEMENT Approved for public release; distribution unlimited.					
13. SUPPLEMENTARY NOTES The views, opinions and/or findings contained in this report are those of the author(s) and should not be constructed as an official Department of the Navy position, policy or decision, unless so designated by other documentation.					
14. ABSTRACT Quarterly progress report No. 4 on AWINN hardware and software configurations of smart, wideband, multi-function antennas, secure configurable platform, close-in command and control for Sea Basing visualization of wireless technologies, Ad Hoc networks, network protocols, real-time resource allocation, Ultra Wideband (UWB) communications network and ranging sensors, cross layer optimization and network interoperability.					
15. SUBJECT TERMS					
16. SECURITY CLASSIFICATION OF:			17. LIMITATION OF ABSTRACT UL	18. NUMBER OF PAGES	19a. NAME OF RESPONSIBLE PERSON Rick Habayeb
a. REPORT U	b. ABSTRACT U	c. THIS PAGE U			19b. TELEPHONE NUMBER (include area code) 540-231-4353



*Advanced Wireless Integrated Navy Network - **AWINN***

4th Quarterly Report

Virginia Tech

October 1, 2005 – December 31, 2005

TABLE OF CONTENTS

Executive Summary	1
1. TASK 1 Advanced Wireless Technologies	2
1.1 Task 1.1 Advanced Antennas	2
1.2 Task 1.2 Advanced Software Radio	25
1.3 Task 1.3 Collaborative and Secure Wireless Communications.....	50
2. TASK 2 Secure and Robust Networks	64
2.1 Task 2.1 Ad Hoc Networks	64
2.2 Task 2.2 Real-Time Resource Management, Communications, and Middleware	72
2.3 Task 2.3 Network Interoperability and Quality of Service	78
2.4 Task 2.4 Cross-Layer Optimization	80
3. Task 3 Visualization of Wireless Technology and Ad Hoc Networks.....	96
3.1 Overview	96
3.2 Task Activities for the period.....	96
3.3 Importance/Relevance	99
3.4 Productivity	100
4. TASK 4 Testing and Demonstrations.....	101
4.1 TIP#1 Distributed MIMO UWB sensor networks incorporating software radio	101
4.2 TIP#2 Close-in UWB wireless application to Sea Basing	115
4.3 TIP#3 Secure Ad Hoc Networks	119
4.4 TIP#4 Integration of Close-in UWB Wireless with ESM Crane for Sea Basing Applications	124
5. FINANCIAL REPORT.....	126

Executive Summary

This fourth quarterly report provides summaries on the activities and productivity of the AWINN team at Virginia Tech. The report covers the following thrust areas:

- Advanced Wireless Technology
- Secure and Robust Networks
- Visualization of Wireless Technology and Ad Hoc Networks
- Technology Integration Projects

During this reporting period, the AWINN team successfully conducted the first demonstration of technology integration. The positive interaction between the diverse AWINN technologies provides good insights into the engineering of useful products. The Antenna group provided tailored antennas to the UWB and SDR groups.. The group's analysis shows that Tapered Slot / Vivaldi, Impulse Radiating Antennas (IRA), and TEM Horn antennas are good candidates for Wideband and UWB applications. The SDR team focused on the development of prototype transceivers and algorithms to support UWB, MIMO communications, position location and ranging. The SDR initial algorithms were developed and tested in a proof-of-concept laboratory environment. The results show that ranging accuracy should be within a few inches and that position location by evaluating the multipath delay profile is possible. The algorithms will be modified to provide full 3-D ranging and positioning information. The MIMO UWB group investigated the Third Order Intercept Point IP3 issue for the I-UWB receiver. IP3 is the point at which the output powers of the fundamental signal and the third harmonic are equal. Tests conducted by the group confirm that time-interleaved sampling of UWB pulses using off-the-shelf components is feasible. The Collaborative and Secure Communications team is developing protocols for inter and intra communications between network nodes. They are investigating methods for improving the communication link performance between a mobile base station and distributed mobile sensor network. The Reconfigurable Computing group developed a technique to enhance the processing speed of the SDR transceiver. The technique is based on creating data paths to handle high data rates using COTS FPGAs. The effort of the Cross-Layer Optimization group is focused on cross-layer design of UWB for position location networks PoLoNet and collaborative radio networks. The Networking group is investigating various protocols for QoS, security, mobile routing, and cross-layer optimization. The team is integrating the routing and MAC (medium access control) protocols for ad hoc networks of multiple channel operations to support both IPv4 and IPv6. The Real-Time team is concentrating on the standard for the Distributed Real-Time Specification of Java (DRTSJ), the time utility function, and the implementation of distributed Thread Polling algorithm. The Visualization of Wireless Technology team is completing an investigation of a UWB contactless sensor for close-in operations. Early results indicate that UWB sensor technology is applicable to the close-in environment. The Technology Integration Projects (TIP) are developing various merging approaches to integrate and demonstrate the AWINNN technologies.

1. TASK 1 Advanced Wireless Technologies

1.1 Task 1.1 Advanced Antennas

Overview

Task Goal: This task investigates new antenna technologies that may be applicable to Navy missions and provide hardware for AWINN integration projects.

Organization: This task is managed by Director of Virginia Tech Antenna Group (VTAG) using the following personnel:

Bill Davis, Director
Warren Stutzman, Faculty
Randall Nealy, Engineer
Taeyoung Yang, GRA
Scott Bates, GRA
John Kim, GRA
Gaurav Joshi, GRA

Summary: This quarter's progress continued the development of small antennas for other tasks using UWB and small antennas. Identification of specific requirements for antennas to support the AWINN demonstrations has been completed and prototypes provided for the projects. In this report, antenna models for the digital ship task are considered, as are processes of developing baluns and feed networks. Lastly, thoughts on modeling a ship propagation environment are provided with techniques for measurement using UWB.

Task Activities for the Period

Task objective: Investigate new antenna technologies applicable to Navy missions and provide hardware for AWINN integration projects.

Links to other tasks: Tasks 1.2, 1.3, 3, and 4

Subtask 1.1a Investigation of compact antennas for handheld and mobile terminals

Task objective: Design compact planar UWB antennas for various applications and systems.

Accomplishments during reporting period: This task develops antennas for use in handheld and mobile terminals that require compact size and robust performance for both fixed and portable systems. The concepts will be extended to include fixed and portable terminal needs with emphasis on smart antennas, wideband antennas, and UWB antennas in support of the AWINN demonstrations. Directive terminal antennas allow improved anti-jamming effectiveness by limiting the radiation pattern with directional elements, possibly in a partitioned array.

This quarter, the effort was directed to the design and characterization of UWB tape helix antennas (Figure 1.1-1a and b) antennas. The tape helix is a good candidate for UWB handheld and mobile terminals that require directional radiation. The metal pattern of the tape helix can be printed on flexible, printed-circuit board material, supporting easy fabrication and mass production. In addition, an impulse-radiating antenna (Figure 1.1-1c) was designed and its performance was evaluated through simulations. The designed impulse-radiating antenna will be used for demonstrating some new aspects of the fundamental-limit theory on antennas.

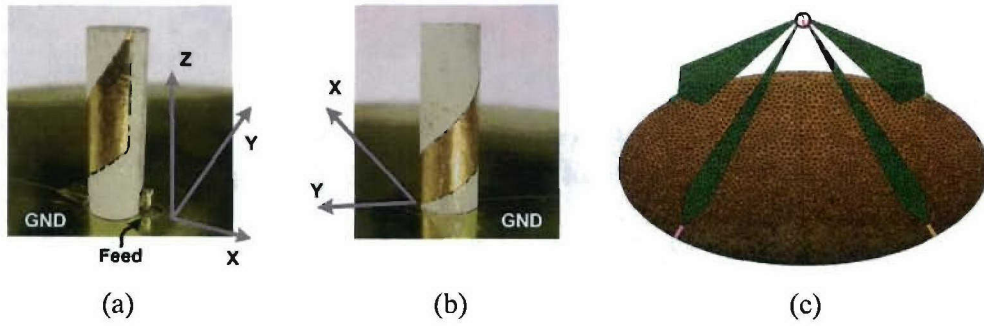


Figure 1.1-1 Fabricated UWB tape helix (a, b) and designed impulse-radiating antenna (c).

A new effort in UWB antennas will include the characterization of the antennas for use in transient or wideband simulation and design. The characterization provides a minimal parameter description of the antenna properties that is also useful in frequency domain antenna and propagation simulations. The UWB offers a large potential for channel modeling, as well as multipath mitigation over short distances. Support will also be given to Task 3 in developing a physics/engineering-based template for radar simulation in an operational setting, including common EW techniques such as angle and range walk-off. Lastly, some effort will be devoted to the development of appropriate feed networks for the wideband balanced antenna systems developed under the NAVCIITI program.

Various planar, monopole-like, ultra-wideband antennas have been proposed in the literature as shown in Figure 1.1-2. The antennas include monopoles of rectangular shape (Figure 1.1-2a), inverted triangular form similar to the bow-tie dipole (Figure 1.1-2b), triangular (Figure 1.1-2c), disk (Figure 1.1-2d), elliptical (Figure 1.1-2e), half-disk (Figure 1.1-2f), and inverted cone with holes (Figure 1.1-2g). Typically, the ratio of height-to-width of these antennas is in the range of 2 to 1. However, the footprint for some portable UWB applications requires a higher ratio, making the width a more critical specification than height. To meet this need, several sample structures were constructed in a rolled form to create UWB antennas with a higher ratio. The bi-arm rolled monopole (Figure 1.1-2h) is created by wrapping the rectangular monopole to achieve about a 5.3:1 height-to-width ratio and showing a good impulse response with a fast-decay ringing. The monopole with a twist (Figure 1.1-2i) is created by wrapping the half of a triangular monopole to obtain about a 2:1 ratio. However, the metal patterns of both antennas are not located on the surface of the cylinder with fixed radius, which may cause some difficulties when trying to print those antennas on flexible printed circuit boards or on thin film for mass production. The manufacturing limitations motivated us to investigate a logarithmic tape helix with equiangular width. The metal pattern is located on the surface of the cylinder with fixed radius.

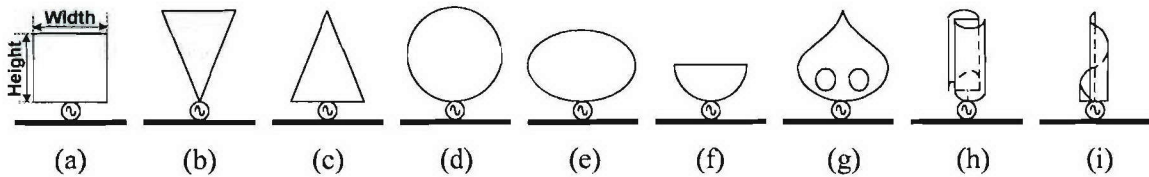


Figure 1.1-2 Various structures of proposed ultra-wideband monopole antennas.

As shown in **Figure 1.1-3a**, the tape helix is exponentially tapered with an equiangular, azimuthal width, whereas the fat monopole has no taper and the monopole with a twist has a linear taper.

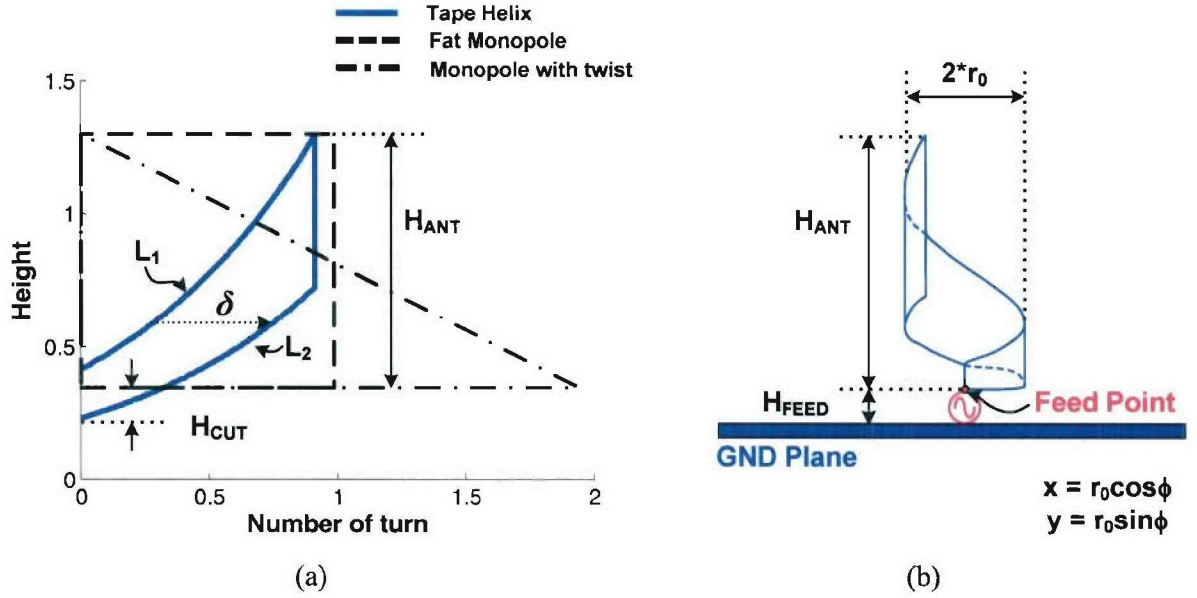


Figure 1.1-3 Geometry of the tape helix and the associated parameters.

The heights of two generating lines for L_1 and L_2 versus ϕ are determined by the following equations:

$$z_{L_1} = \alpha r_0 e^{b\phi} \quad (1.1-1)$$

$$z_{L_2} = \alpha r_0 e^{b(\phi-\delta)} \quad (1.1-2)$$

where α is linear scaling factor, r_0 is radius, b is wrapping rate and δ is angular width. The parameters α and δ control the overall antenna input impedance and bandwidth. The bottom of the tape helix starts at H_{CUT} . Both H_{FEED} and H_{CUT} are used to control the capacitance between the antenna structure and ground so that it provides a better impedance match to the reference impedance. The height of the tape helix structure is H_{ANT} and the overall height including feed gap is $H_{ANT} + H_{FEED}$, as shown in Figure 1.1-3b. A tape helix for the indoor/handheld UWB frequency range, 3.1-10.6 GHz, and a related fat monopole with the same overall dimensions were prepared for a performance comparison. The associated parameter values for each antenna are tabulated in

Table 1.1-1 and the pictures are shown in Figure 1.1-4.

Table 1.1-1 Summary of the Assigned Parameters for the Test Antennas

	A	r_0	b	Δ	H_{ANT}	H_{CUT}	H_{FEED}
Tape Helix	2.7475	150 mil	0.2	0.291 radian	965 mil	100 mil	25 mil
Fat Monopole	×	150 mil	×	×	940 mil	×	50 mil

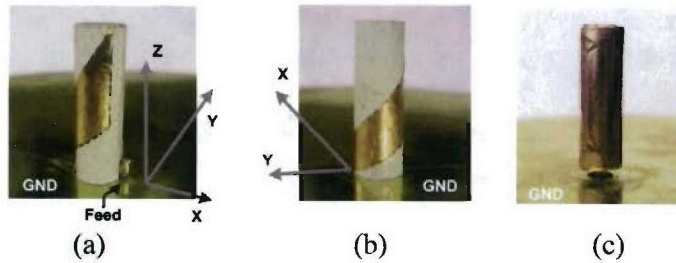


Figure 1.1-4 Picture of tape (a & b) and fat (c) monopoles (size: 150 mill radius and 0.99" height for both antennas, including feed gap) on a 3" radius ground metal.

The measured, return-loss comparison between the fat monopole and tape helix is depicted in Figure 1.1-5. The impedance bandwidth (VSWR < 3) of the fabricated tape helix is about 2.5 – 12 GHz, whereas the return loss characteristic of the fat monopole fluctuates over the frequencies of interest.

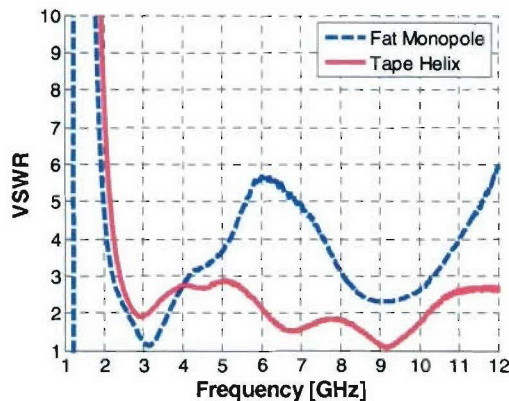


Figure 1.1-5 Comparison of the measured return loss for the fat monopole and tape helix of Figure 1.1-4.

Links to other tasks: This task supports the Task 1.2 and Task 4

Schedule: This effort continued through December 2005. Some future work may still occur on this task, but not as a major effort.

Personnel: Taeyoung Yang, GRA

Subtask 1.1b Antenna Characterization – transient & wideband

Task objective: Provide antenna characterization methods in both frequency and time domain

Accomplishments during reporting period:

Some experimental and simulation results in both time and frequency domains were obtained to characterize the designed UWB tape helix antenna. Using a HP 8720, the transient response and the group delay were determined. Two identical co-polarized antennas (both for the tape helix and the fat monopole) were used and separated by 40" in order to be in the far-field region. A Gaussian pulse, with a 50 ps, 50% pulse width, was used to excite the antennas.

As shown in Figure 1.1-6, the group delay of the tape helix measured at four different azimuth angles are fairly constant to about 11 GHz, while the fat monopole has a constant group delay to about 8 GHz. However, typically this non-constant group delay at high frequencies does not influence the peak amplitude and pulse width of the impulse response significantly, because the peak amplitude and late time response are dominated by the low-end frequency response. As a

result, all measured transient responses in Figure 1.1-8 for both the fat monopole and tape helix show a narrow pulse width and a non-dispersive pulse shape.

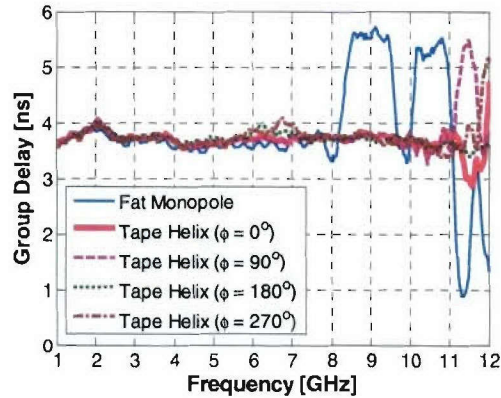


Figure 1.1-6 Comparison of the measured group delay between fat monopole and tape helix antennas of Figure 1.1-4.

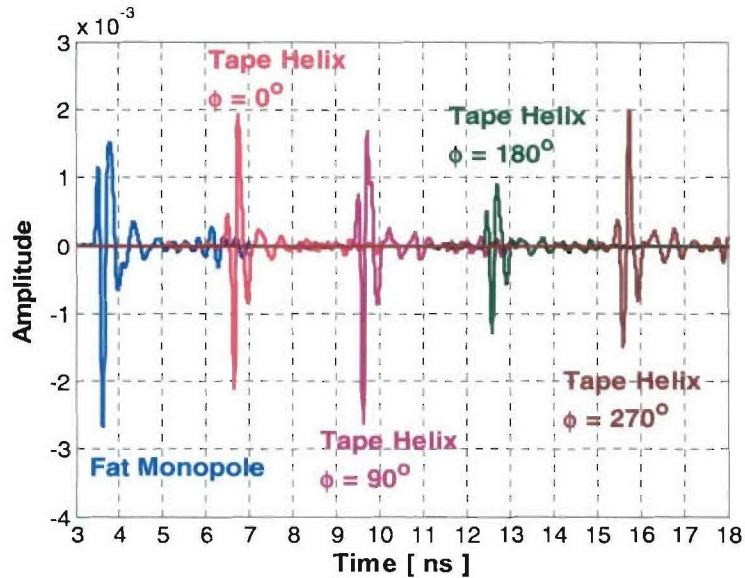


Figure 1.1-7 Comparison of the measured transient responses for tape helix and fat monopole antennas of Figure 1.1-4 (note that the 3 ns time shift is added between transient responses in order to clearly distinguish each pulse shape).

A minor ringing for each transient response is observed in the late time response. The transient pulse shape of the tape helix varies with angle because the tape helix does not have a symmetrical shape. This suggests that the radiation patterns are not omni-directional at all operating frequencies. At $\phi = 0^\circ$, the impulse response of the tape helix shows a nice doublet. Interestingly, the impulse response of the tape helix at $\phi = 90^\circ$ is very similar to the response of fat monopole and has the largest peak amplitude among the considered directions. This means that most of the low-frequency components radiate at $\phi = 90^\circ$ and $\theta = 90^\circ$. The transient response at $\phi = 180^\circ$ has the smallest peak amplitude, which is in the opposite direction of feed point.

The radiation patterns measured at 3, 6.5, and 10 GHz are depicted in Figure 1.1-8. At 3 GHz, the radiation pattern is omni-directional and the tape helix works in the normal mode. As frequency

increases, the field component E_ϕ increases and its peak directivity is similar to E_θ at the surface of the ground plane. This result and the simulated axial ratio using a commercial FDTD code (Zeland Fidelity[®]) imply that the tape helix at high frequencies provides circular polarization in the axial mode. In addition, the radiation patterns in Figure 1.1-8 show that the tape helix does not support omni-directional patterns at higher frequencies as suggested by the impulse response, which may be useful for some applications. For example, cell phones, with a UWB communication capability, can provide a reduced specific absorption rate (SAR) to the human head and mitigate interference to hearing aids if the tape helix is used as the antenna.

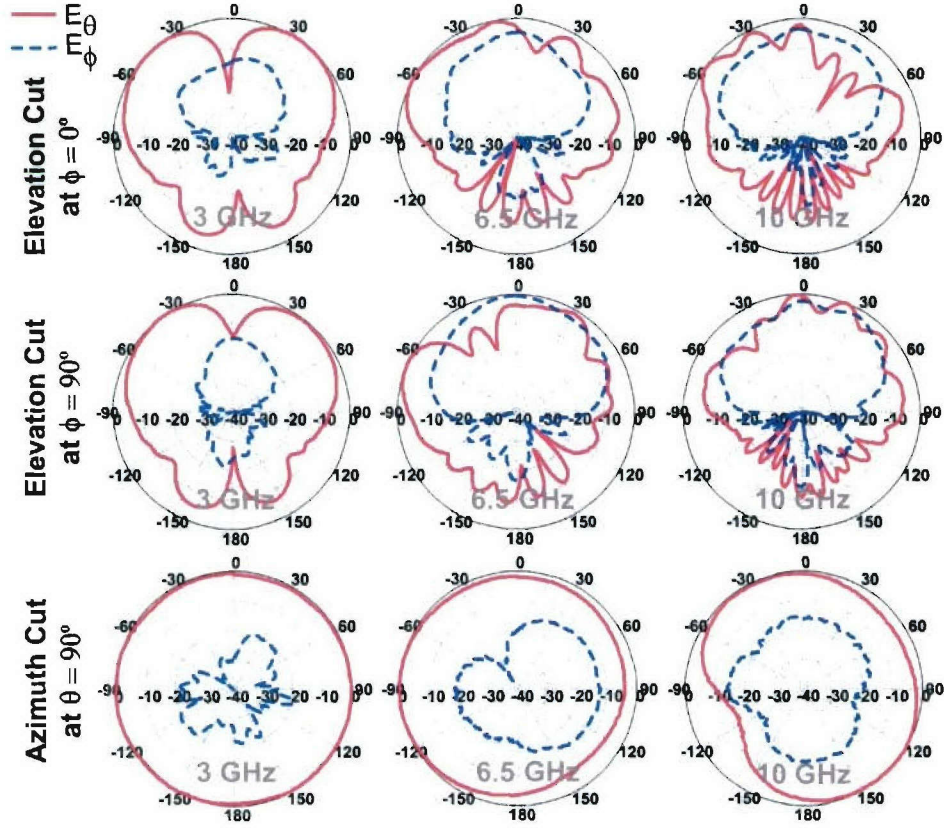


Figure 1.1-8 Comparison of the measured normalized radiation directivity patterns of the tape helix at 3, 6.5, and 10 GHz.

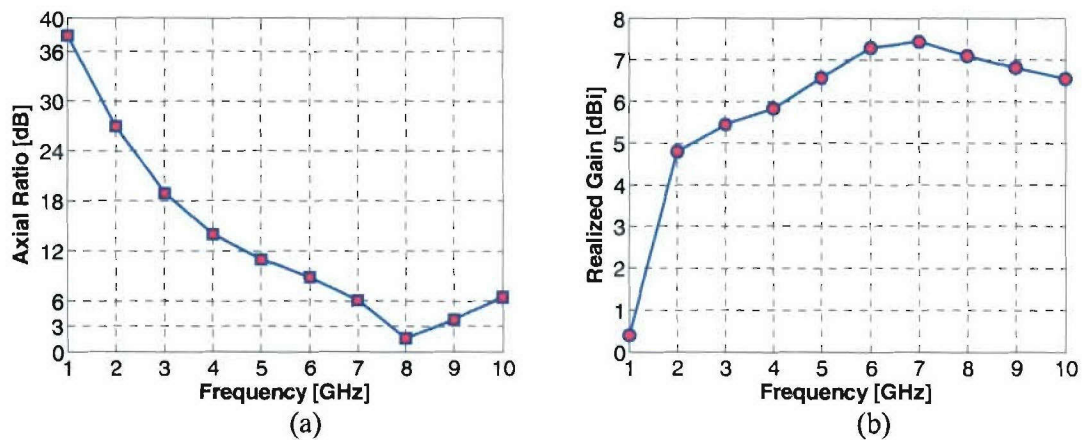


Figure 1.1-9 Simulation results for the designed tape helix antenna of Figure 1.1-4 a and b on an infinite ground plane – (a) Axial ratio at the normal direction to the ground plane ($\theta=0$) and (b) Realized gain.

The calculated axial ratio and realized gain are plotted in Figure 1.1-9. As frequency increases, the realized gain increases through 7 GHz, which is about the frequency that the axial mode is exited. After 7 GHz, the realized gain decreases.

Test antennas for the tape helix and a fat monopole supporting the indoor/ handheld UWB range (3.1-10.6 GHz) were fabricated, characterized, and compared in both the frequency and time domains using both measurements and simulations. The ratio of height-to-diameter for the tape helix with a height of 0.9" was 3. Even though the test helix was not optimized, the measurement results showed an impedance bandwidth (VSWR <3) of 2.5 – 12 GHz and a group delay fairly flat to 11 GHz. The measured impulse response was marginally directional in azimuth and had a narrow pulse width (less than 500 picoseconds for 50 ps Gaussian source) without dispersion. The computed realized gain was over 5 dBi for the 2.5 – 12 GHz range.

Thus, the tape helix is a good candidate for UWB applications requiring directional radiation. The metal pattern of the tape helix can be printed on flexible printed circuits boards, for easy fabrication and mass production.

Links to other tasks: This task supports the task 1.1a, b, c, and e.

Schedule: This task will continue through the contract, with coupling to Subtask 1.1d.

Personnel: Taeyoung Yang, GRA

Subtask 1.1c UWB antenna design (support of AWINN demonstrations)

Task objective: Design various UWB and other antennas needed for AWINN demonstrations

Accomplishments during reporting period:

The objective of the current work is to develop an antenna for a directional SDR (software-defined radio) receiver. The specifications for the antenna are listed in Table 1.1-2. Some of the possible antenna candidates are presented in the following subsections.

Table 1.1-2 Specifications of the Needed Antenna

Size	Not a major constraint but an antenna dimension fitting inside a 6" x 6" x 6" is desired
Transmitted Pulse Width	Given a 500 ps pulse input, the transmitted pulse width should be 1000-1500ps, with minimal pulse dispersion or ringing
Gain	Not a major constraint
Weight	Not a concern
Absolute Frequency Range	Any range that is required to achieve the pulse width needed

Antenna Selection

For this task, a tapered-slot antenna (TSA) was chosen. An impulse-radiating antenna (IRA) and a TEM-horn antenna were also considered. The IRA and TEM horn can be designed to meet the necessary electrical requirements but the biggest concern was the size of the antenna. With the specified dimensions, the TSA was the best candidate for this task. There are two major components that need to be designed in order to build the antenna: a balun and the TSA.

Balun/Feed Technique

Almost always, a TSA is excited by a slotline. In order to incorporate the antenna into a system, the antenna has to be integrated with other microwave circuits or common transmission media such as coaxial cable or microstrip line. Since a TSA is a balanced structure, the use of a balun is required in order to make transition between the slot line and any unbalanced transmission media.

Some of the feed schemes considered were a coax to slotline transition, a microstrip to slotline transition, use of an antipodal TSA, and use of a double-Y balun [1.1-5]. The coax to slotline transition shown in Figure 0-10 is a very simple setup to build. The outer conductor is simply electrically connected to one side of the slotline and the center conductor is connected to the other side of the slotline. The problem is this setup has a high return loss due to self inductance in the feed [2], making the transition unsuitable. The microstrip to slotline transition is shown in Figure 1.1-11. The printed transmission structure makes integration easy.

However, the length of the stubs are $\lambda/4$, limiting the bandwidth of the transition. There are other microstrip to slotline transitions, but the physical dimension and ease of construction typical increase for those structures.

The antipodal TSA (ATSA) is constructed with the two slot sides on opposite sides of the substrate. A diagram of the construction is shown in Figure 1.1-12. It has a good VSWR and radiation pattern, but as the frequency increases there is a substantial amount of cross polarization [4]. This cross polarization lowers the upper limit of the antenna bandwidth.

The double-Y balun is used in many different transitions, including the microstrip to stripline transition. A diagram of double-Y balun is shown in Figure 1.1-13. This balun shows a very wide bandwidth with very little return loss. The performance of the double-Y balun mainly depends on the quality of the short and the open at the end of the stubs [5]. With its overall performance and the ease of construction, the use of double-Y balun was selected.

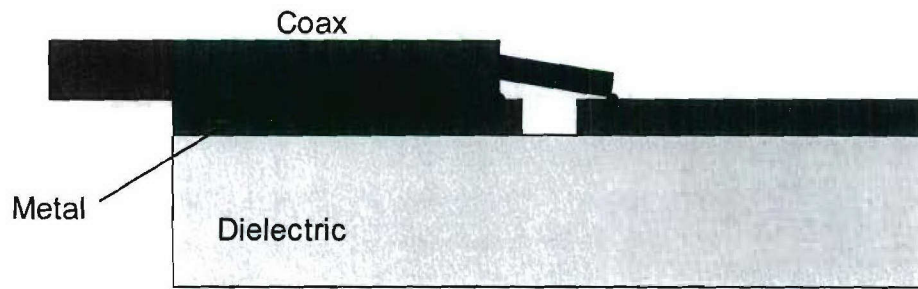


Figure 1.1-10 Coax to slotline transition.

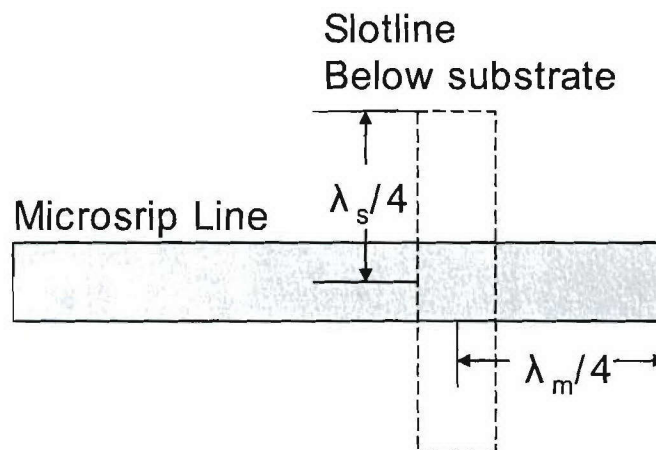


Figure 1.1-11 Microstrip to slotline transition.

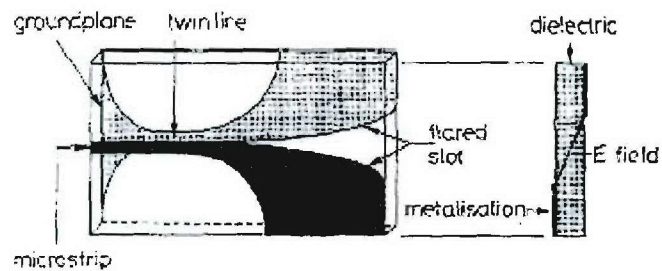


Figure 1.1-12 Antipodal Vivaldi antenna [4].

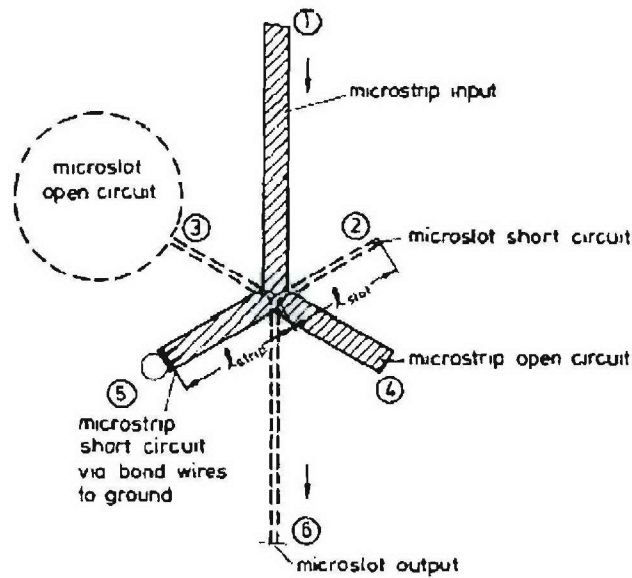


Figure 1.1-13 Double-Y balun [5].

Simulation and Testing

The general block diagram of the antenna setup is shown in Figure 1.1-14. Currently the antenna and the feed setup is simulated with different sizes and shapes using the FDTD method on a commercial package, Fidelity© from Zeland™, to obtain the radiation pattern, return loss, and time domain response. Once a suitable antenna shape and feed structure are determined, a prototype will be built and tested to verify the simulation result.

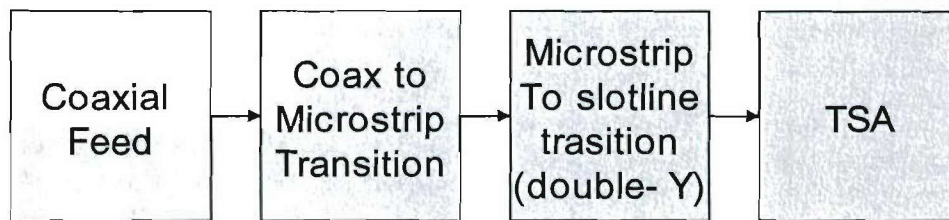


Figure 1.1-14 Block diagram of antenna setup.

References

1. K. F. Lee and W. Chen, ed, *Advances in Microstrip and Printed Antennas*. New York:John Wiley & Sons, Inc., 1997.
2. J. B. Knorr, "Slot-Line Transitions." *IEEE Transactions on Microwave Theory and Techniques*, vol. 22, Issue 5, pp. 548-554, May 1974.
3. E. Gazit, "Improved Design of the Vivaldi Antenna" *IEE Proceedings*, Pt. H, vol. 135, Issue 2, pp. 89-92, April 1988.
4. J. D. S. Langley, P. S. Hall, and P. Newham, "Balanced Antipodal Vivaldi Antenna for Wide Bandwidth Phased Array." *IEE Proceedings, Microwaves, Antennas and Propagation*, vol. 143, Issue 2, pp. 97 – 102, April 1996.

5. B. Schiek and J. Kohler, "An Improved Microstrip-to-Microslot Transition" *IEEE Transactions on Microwave Theory and Techniques*, vol. 24, Issue 4, pp. 231-233, April 1976.

Links to other tasks: This task supports the Task 1.2 and Task 4

Schedule: This subtask is a major part of task in the spring and will continue in support of the other AWINN tasks with prototype antennas, both simulated and built.

Personnel: John Kim (GRA), Randall Nealy (Engineer), and W. Davis (PI)

Subtask 1.1d Antennas providing polarization, spatial, and pattern diversity – Evaluation of antennas in a MIMO environment

Task objective: Base station/access point antennas providing polarization, spatial and pattern diversity useful in supporting MIMO and space-time coding processing. Evaluation of antennas in a MIMO environment.

Accomplishments during reporting period: As part of the ongoing emphasis on the characterization of wideband propagation environments on the topside/upper-deck and even interior of a warship or destroyer, this month's efforts focused on ultra-wideband (UWB) pulse measurements in a building hallway. The topside of a navy warship or destroyer is rich in metallic scatterers, which can be approximately characterized by the large number of arbitrarily shaped scatterers in an indoor environment. Three scenarios were evaluated for ultra-wideband communication over short distances and include all of the information needed for single frequency applications of choice:

- (a) Line-of-Sight (LOS) hallway environment for variable range
- (b) Single scatterer controlled hallway environment
- (c) UWB propagation around a hallway corner

In this month's report, the first case of the line-of-sight UWB propagation environment inside a hallway for various distances between transmit and receive antennas is reported.

Measurement Setup and Antennas

Ultra-wideband pulse measurements were conducted in a controlled hallway environment with scatterers introduced in to the scenario, one-by-one. The UWB pulse is a Gaussian pulse corresponding to a frequency range of 50 MHz – 13 GHz. The measurements were conducted using the vector network analyzer (VNA 8510) inside one of the rooms and the cables extending to the two planar TEM horn antennas in the hallway. The measurement setup and an approximate antenna structure are shown in Figure 1.1-15.

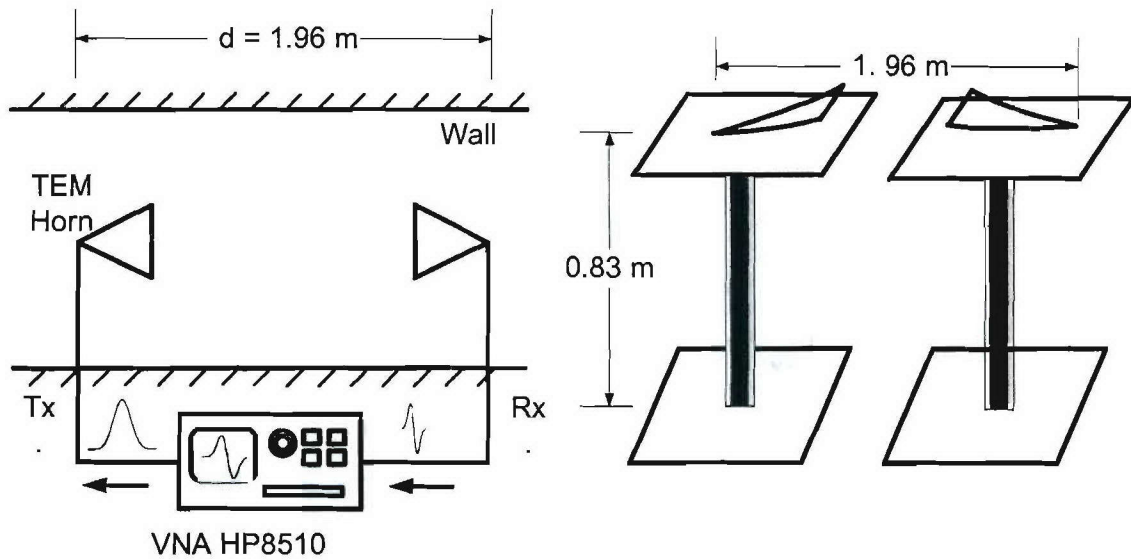


Figure 1.1-15 Measurement setup using two planar TEM horn antennas mounted on pedestals in a hallway environment oriented for direct line-of-sight (LOS).

The frequency response of the link was measured using two planar TEM horn antennas mounted on pedestals at a height of 0.83 m and at a reference distance of 1.96 m as shown in Figure 1.1-16. The distance is the separation between the two feed-points. The TEM horns provide directional properties with typically better than 6 dBi of gain.

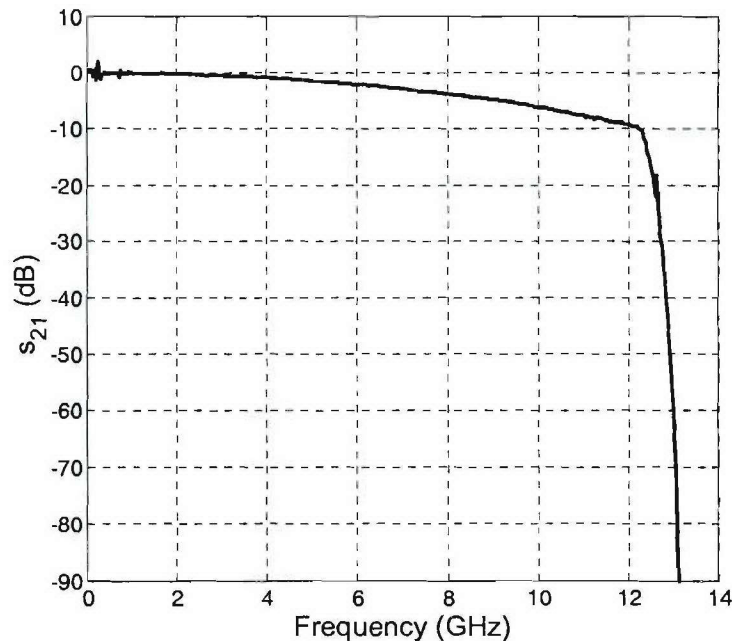


Figure 1.1-16 Frequency response of the LOS link between two planar TEM horn antennas mounted on pedestals at a distance of 1.96 m from the feed-points.

At the reference distance of 1.96 m the corresponding time-domain received signal consisted only of the direct response from the transmitting antenna. The reflections from the floor, walls or the ceiling were not observed due to the close proximity of the antennas. However, when the distance was increased to 2.90 m is shown in Figure 1.1-17, reflections from the floor and the ceiling were

observed, but not from the walls due to the directivity of the antennas. Similar observations were made when the distance was further increased to 5.7 m (not shown). The observed results are consistent with the dimensions of the hallway measurement setup as shown in Table 1.1-3.

Table 1.1-3 Time-delay Analysis of the LOS Hallway Environment

Case:	Component (Absolute Distance, meters)	Relative Distance from Ref ⁿ		Time-delay (ns)
		(meters)	(ft' and inch'')	
Ref ⁿ LOS	1.96	0	0	0
LOS 1 d = 2.9 m	Direct (2.90 m)	0.94	3' 1"	3.12
	Floor (3.54 m)	1.58	5' 2"	5.28
	Ceiling (3.90 m)	1.94	6' 4"	6.03
LOS 2 d = 5.7 m	Direct (5.72 m)	3.76	12' 4"	12.35
	Floor (6.08 m)	4.12	13' 6"	13.55
	Ceiling (6.23 m)	4.27	14' 0"	13.97

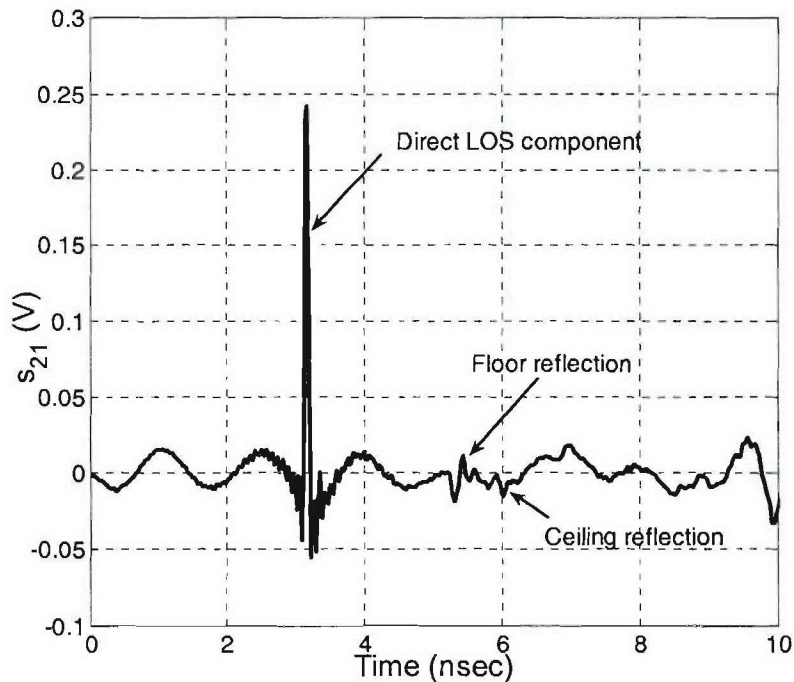


Figure 1.1-17 Time-domain response of the LOS link between two planar TEM horn antennas mounted on pedestals of height 0.83 m at a distance of 5.18 m from the feed-points.

The results are indicative of the presence of a specular response from indoor structures such as the floor, walls and the ceiling. Note that for a 2.90 m distance between the antennas, the furthest multipath component arrives 2.93 ns after the first direct LOS component. As the distance between the antennas increases to 5.70 m, the relative path difference between the direct and

multipath component reflected off the hallway structure reduces. The furthest multipath component arrives 1.62 ns after the first direct LOS component. This has serious implications when the antenna is resonant, in which case the direct LOS component and the multipath components overlap to distort the received signal.

Since these measurements were conducted in the absence of any scatterer, the resonance scatterer response was not observed. The objective of the next month efforts is to introduce scatterers one-by-one and observe the received signal.

Links to other tasks: This topic may impact on the frequency selection and interaction of the measurements used for the Sea-Based cargo systems being considered in Task 3.

Schedule: The majority of the work on this task follows the development of the antennas and is a major subtask in the Spring 2006.

Personnel: Garauv Joshi, GRA

Subtask 1.1e Support physics/engineering-based models for Digital Ships

Task objective: Support of Task 3 to develop physics/engineering-based templates for Digital Ships for radar simulation, including EW techniques.

Accomplishments during reporting period: To provide some potential modeling input for the Digital Ship task, some simple modeling of antennas has been undertaken as a small task. The orientation is a model of an antenna based on a pole-residue description presented in the dissertation of Stani Licul, Virginia Tech, 2004. Since Wheeler (*Proc. IEEE*, vol. 69, pp. 1479-1484, 1947) introduced the concept of fundamental limits on small antennas, there have been efforts to find an exact formulation for minimum radiation Q . Chu (*J. Appl. Phys.* vol 19, pp. 1163-1175, 1948) derived a minimum radiation Q expression using circuit models corresponding to spherical-mode wave impedances. Later, Collin (*IEEE Trans. on AP*, vol. 12, pp. 23-27, 1964) derived expressions for the radiation Q based on the evanescent energy stored near an antenna that are not restricted to the spherical modes and also were developed for cylindrical waves. Fante (*IEEE Trans. on AP*, vol. 17, pp. 151-155, 1969) used the same approach for considering excitation of both TM and TE modes. Foltz and Mclean (IEEE AP Symposium, 1999) extended the fundamental-limit theory to antennas with a large aspect ratio. Grimes (*Radio Science*, 34, pp. 281-296, 1999) investigated radiation Q with a time-domain approach. The work since Chu has often included conceptual errors in the definition of radiated energy which resulted in higher estimates of the Q than is proper. The results of Chu are still found to provide the most reliable estimates.

Fundamental-limit theory shows that the designer must trade off factors of antenna size, gain, and bandwidth, and that significant improvement of all quantities in the same design is impossible. Efforts over the past half century have focused on the accuracy of the theory. Only the TM_{01} spherical mode has been emphasized because the TM_{01} mode provides the minimum radiation Q , although such a mode also provides an omni-directional radiation pattern.

Through the on-going study, we explore some new variations on the fundamental-limit theory of antenna performance. These include an equivalent pole-residue model of Chu's circuit model, some implicit assumptions of bandwidth and pattern related to the specific mode of consideration, and the radiated power of electrically-small antennas with a function of antenna size and source conditions (voltage, current, and power sources). These new variations on the fundamental-limit theory of antenna performance provide a new approach to design a optimize antenna which is close to the theoretical limit of antenna performance.

As a start, we designed the impulse radiating antenna (IRA) which we expect this particular antenna is close to the response of the ideal antenna that the Chu's model suggested. The detail antenna configuration and design parameters are shown in Figure 1.1-18a. In order to reduce the meshes and computer memories required in simulation, we applied both electric and magnetic symmetries (see Figure 1.1-18b) so that we only simulate the quarter part of the original antenna size.

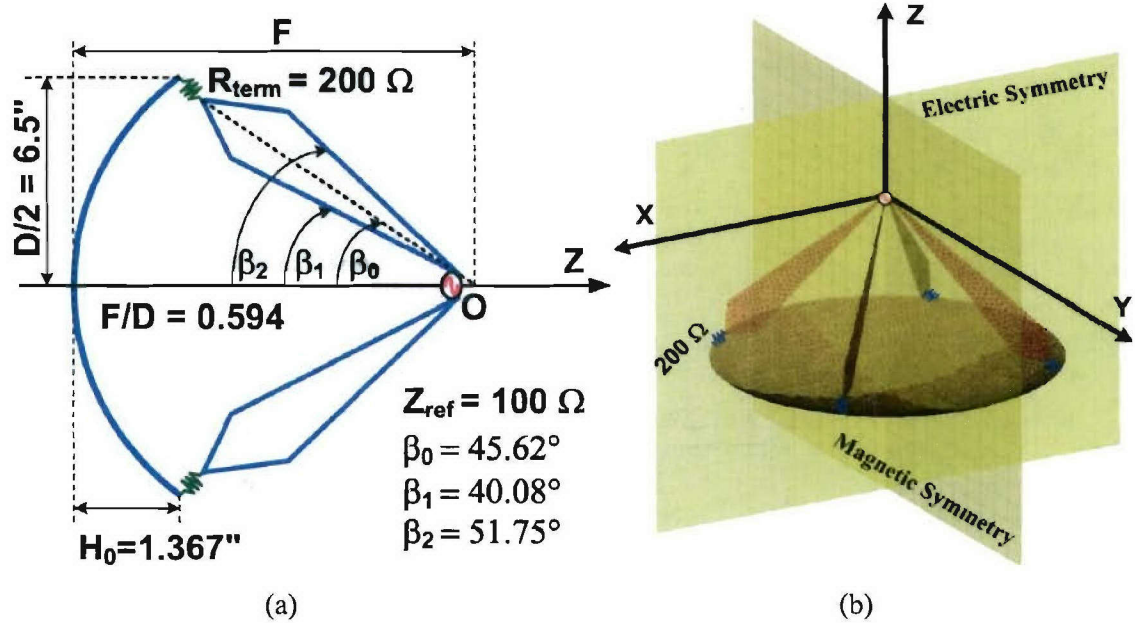
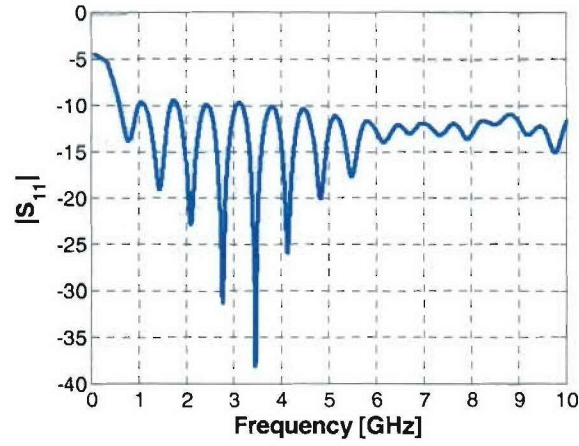
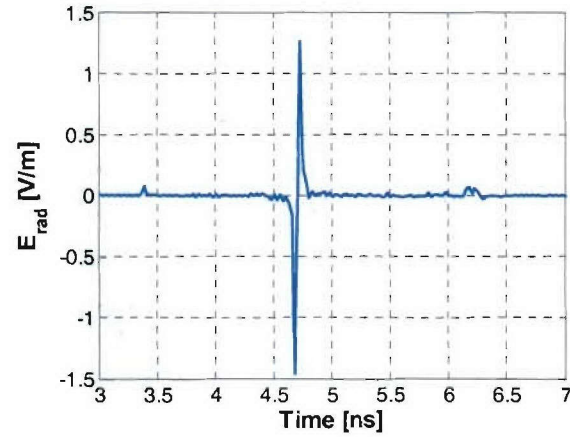


Figure 1.1-18 Geometry of Impulse Radiating Antenna (a) and its symmetry planes (b).

Using a commercial method of moment code (FEKO), the return loss (Figure 1.1-19a) and the impulse response (Figure 1.1-19b) were calculated. The designed IRA matches 50 Ohms well from 500 MHz to 10 GHz and shows some mismatch below 500 MHz. The minor mismatch in the band can be improved with a different value of termination resistor or surface resistance, providing a smooth resistance change. The impulse response has a couple of glitches around 3.4 ns and 6.3 ns as expected. These were caused from the direct radiation of feed arms and reflections of mismatched termination resistors.



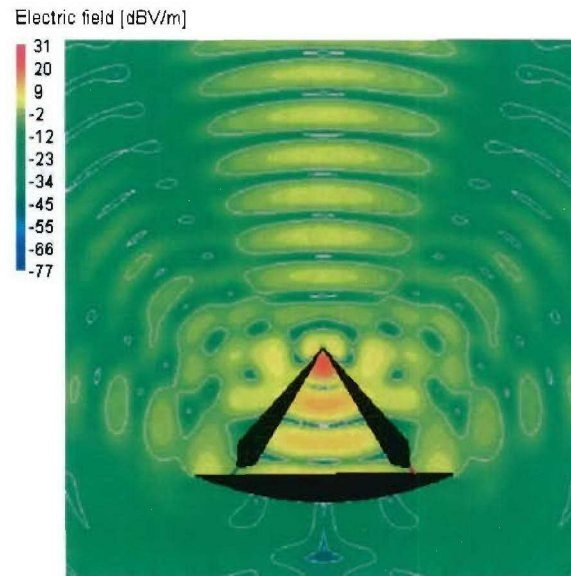
(a)



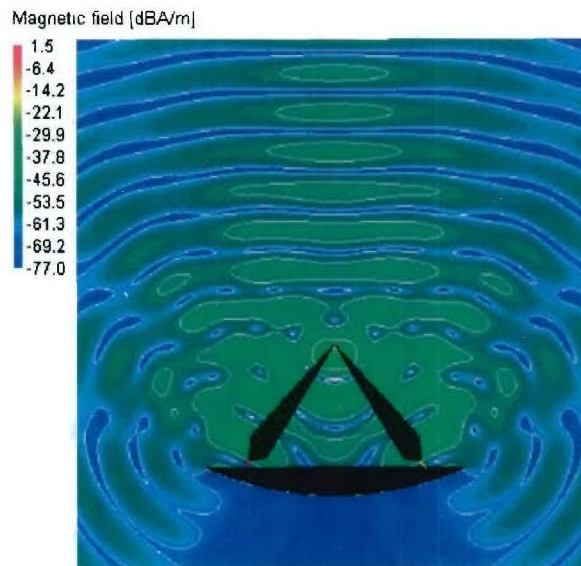
(b)

Figure 1.1-19 Return loss (a) and impulse response of the impulse radiating antenna (b) of Figure 1.1-18 obtained using the FEKO simulation package.

In order to observe whether the IRA generates a plane waves after the focal point, instantaneous electric and magnetic fields were calculated at 3 GHz. As shown in Figure 1.1-20, it is apparent that the reflected waves become the plane wave in Figure 1.1-20, but there is also some interaction caused from the feed region.



(a) YZ plane



(b) XZ plane

Figure 1.1-20 Distribution of instantaneous (a) electric and (b) magnetic fields with $\omega t = 90^\circ$ at 3 GHz.

The radiation gain pattern was also calculated and is shown in Figure 1.1-21. The IRA has maximum gain at boresight and we observe a few side lobes caused from the feed reaction.

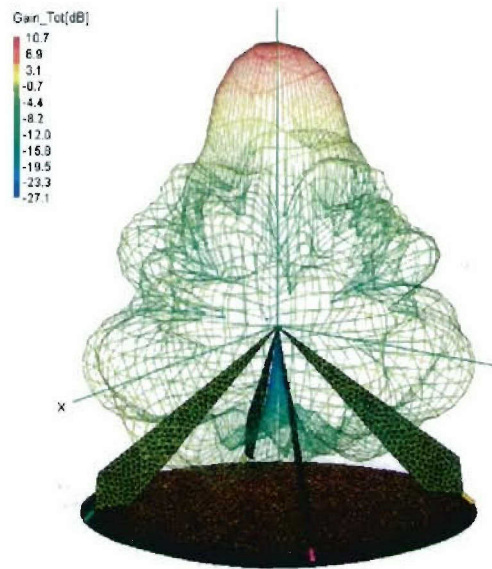


Figure 1.1-21 Radiation gain pattern at 3 GHz of the IAA antenna of Figure 1.1-19.

Links to other tasks: Supports Task 3

Schedule: As requested by the personnel of Task 3. Some work may continue because it is useful to Task 3.

Personnel: Taeyoung Yang, GRA

Subtask 1.1f Wideband balanced antenna/array feed networks

Task objective: Development of array feed networks for wideband balanced antenna systems such as the Fourpoint antenna investigated in the NAVCIITI program

Accomplishments during reporting period: Last semester was spent becoming acquainted with baluns: why they are needed, what types exist, and effective measurement techniques. This report will give a quick summary of potentially useful balun designs for wideband and ultra-wideband applications. In the course of researching the various balun designs it became apparent that there exist various ways of verifying the efficacy of a balun. Some methods appear to provide a more thorough analysis of balun performance than other methods. Antenna array feed-networks will also be addressed.

Wide Band Baluns

As a quick review, an antenna system generally includes a coaxial feed line at some point in the feed network. Coaxial cables are inherently unbalanced. Feeding a balanced antenna with an unbalanced line can have an undesirable effect on the antenna pattern, due to radiation of currents on the exterior of the coax. A balun is used to convert the unbalanced signal from the coaxial cable into a balanced signal that does not adversely affect a balanced antenna pattern.

There are a plethora of different balun designs available. Many of the antenna designs of interest on this project are of the compact planar variety. As a result, we have concentrated on balun designs that have a planar form factor. We also concentrated on investigating baluns which are popular and versatile. By "popular," we mean balun designs that have broad exposure in the literature. Also of interest during this search were the bandwidth characteristics of the various balun designs.

To date, we have found 5 general and well known balun types that can be used to balance wideband to ultra-wideband antenna designs. This group can accommodate both planar designs and parallel designs (antennas that have elements on the top and bottom of a dielectric substrate) as shown in Table 1.1-4.

Table 1.1-4 Wideband and Ultra-Wideband baluns

Balun Type	Bandwidth
Tapered	50:1 to 100:1
Double-Y	6:1
Marchand	2:1 to 4:1
CPW-to-CPS, CPW-to-slot line	2:1

Balun Measurement

It is of interest to know if a balun design provides an intended amount of balance over some required frequency range. Several methods are presently in wide use. One method for determining balance is to integrate the balun with the desired antenna system and acquire a pattern for the antenna. This assumes that a balanced antenna pattern is known *a priori*. A comparison between the acquired patterns, incorporating the balun, with that of the expected pattern is then made. Even if the pattern is not known *a priori*, a symmetric pattern offers evidence of proper balun operation. Often, for various reasons, it is desirable to characterize the balun directly without integration into a system. The second method accomplishes this goal by considering the balun as a two or three-port device and taking measurements using a vector network analyzer. An example of a three-port balun would be a 180° hybrid. The input port accepts the unbalanced signal and produces two output signals that have the same magnitude but phases differing by 180° . In this case, the output currents are balanced in comparison to one another. This type of balun can be measured in a straightforward manner as a three-port device. The amount of balance can be determined by looking at the magnitudes and phases of S_{21} and S_{31} . For balance, we expect $|S_{21}| = |S_{31}|$ and $|\theta_{31} - \theta_{21}| = 180^\circ$. Impedance issues are also easily considered.

In contrast, a two-port balun accepts an unbalanced signal at the input port and produces a single balanced signal at the output port. This poses a problem in terms of output port measurement because most measurement instruments are connected to the device under test using a length of coaxial cable, which is inherently unbalanced. To overcome this issue a standard practice has been to directly connect two of the baluns to be measured such that the balanced output port of one feeds the balanced port of the other, leaving the unbalanced port on the output side to connect to the unbalanced line from the measurement device. This arrangement is known as a back-to-back measurement.

We have been investigating the details of the standard back-to-back measurement for extraction of critical balance information. A method is being developed for increasing the amount of information acquired to help determine a more accurate measure of balance, across some specified bandwidth. This method, called direct-invert, requires two back-to-back measurements such that the orientations with respect to the balanced port terminals are switched between the two measurements. We hope to produce a measurement technique which is easy to carry out and potentially provides a full display of balun performance.

Feed Networks

An antenna can consist of a single element or many elements. The complexity of the network that feeds the antenna has a direct relationship to the antenna complexity. As indicated above, the feed-network can have a direct effect on the performance of a balanced, single-element antenna. Because multi-element array antennas many times use not only the amplitude of the signal but also the phase of the signal at each element to produce a desired field pattern, they can be even more sensitive to feed-network design.

The essential role of a feed network is to allow an antenna to receive the maximum desired signal at its input port or ports without reflections or other adverse affects to the pattern. For single element antennas the feed network can have several functions. Correcting any balance issues is one. Many times there is also an impedance mismatch between the feed line and the antenna. In this case an impedance matching network is needed to prevent unwanted reflections. In the case of an antenna array, the geometry of the more complicated feed network can introduce unwanted phase changes in the signal as it arrives at each element. One result of this can be that portions of the antenna that in theory have quite deep nulls are now filled. As the number of array elements increases, the complexity and length of the feed network increases. Ohmic and dielectric losses might become an issue for complicated, and hence long, networks, which can degrade the signals reaching the elements. Mitigating these two issues in concert with any matching and balancing functions that the array feed-network must accomplish make them that much more complicated to design for array antennas. An additional factor that must be considered for arrays is the mutual coupling between elements. Many designers go to extreme lengths to minimize mutual coupling, while proper accounting of the mutual coupling can actually be used to enhance the array performance and even extend the bandwidth limits of the array.

Thus far much time has been invested in considering various planar balun designs for broadband applications. If properly designed, many of the baluns can incorporate impedance matching functions as well. These elements can, in turn, be incorporated into array feed networks.

Goals for this Semester

The goals for this semester are three fold: 1) Complete the details of the balun measurement study; 2) Design, build and measure two different balun types; and 3) Look more closely at array feed networks with the idea of including any necessary impedance matching elements and baluns into the network.

Links to other tasks: In support of Task 3 on Digital Ships

Schedule: This subtask will continue through Spring 2006 in support of methods of feeding antenna structures and arrays. The emphasis will continue as baluns, but feed networks will be considered also.

Personnel: Scott Bates, GRA

Importance/Relevance

The designed UWB tape helix antennas can well accommodate the current needs for the handheld and mobile terminals requiring directional radiation and small width form factor.

The designed impulse radiation antenna (IRA) will provide the concept of the ideal antenna, which is corresponding to the fundamental-limit theory on antenna performance.

The designed compact planar UWB antennas can well accommodate the current needs for the handheld and mobile terminals. The designed frequency notch UWB antennas might provide a solution to reduce the inference to the existing other narrow band applications.

Specific requirements have been identified to set the antenna specifications for the software defined radio and sea-based tasks. This has been described in the task summary for this quarter.

A review of both wideband antennas and baluns has been performed to provide a focus of effort toward the antenna needs of the project.

The information of desktop antenna and propagation prediction is an item of critical interest in the design of topside platform configurations. Propagation measurements to estimate performance effects will continue.

Productivity

Conference publications

1. Taeyoung Yang, William A. Davis, and Warren L. Stutzman, "Normal-Mode, Logarithmic, Ultra-Wideband Tape Helix," *IEEE International Workshop on Antenna Technology: Small Antennas and Novel Metamaterials*, to appear, Mar., 2006.
2. Taeyoung Yang, William A. Davis, and Warren L. Stutzman, "Some New Aspects of Fundamental-Limit Theory on Antennas," *IEEE AP-S/URSI International Symposium*, submitted, July 3-8, 2006.
3. Taeyoung Yang and William A. Davis, "Miniaturization Of Planar Two-Arm Spiral Antennas Using Slow-Wave Enhancements," 2006 National Radio Science Meeting, Boulder, CO, 3-8 Jan.
4. Gaurav Yang, William A. Davis, and Warren L. Stutzman, "Statistical & 'Fuzzy Pole' Characterization of the complex poles of a Thin Wire and a Conducting Sphere," 2006 National Radio Science Meeting, Boulder, CO, 3-8 Jan.

Honors and Recognitions

1. W. A. Davis, MC of the Institute for Defense and Government Advancement: Military Antenna Systems, 20-21 Sep 2005, Arlington, VA

Students supported

Taeyoung Yang, Scott Bates, John Kim: Aug 15, 2005 – present
Terry Vogler, Gaurav Joshi: January 1, 2006 – present

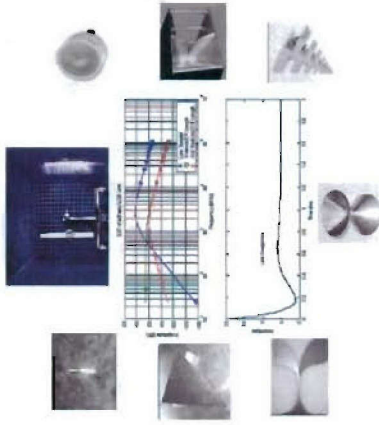
Faculty supported

Dr. William A. Davis, VTAG Director, Jan. 15, 2005 – present
Dr. Warren L. Stutzman, Faculty, Jan. 15, 2005 – present

Staff and other personnel supported

Mr. Randall Nealy, VTAG Engineer, Jan. 15, 2005 - present

Advanced Wireless Integrated Navy Network (AWINN)



Technical Significance

- To support the design and Implementation of a flexible, reconfigurable wireless network with multiple frequency requirements, including the capabilities of ultra-wideband (UWB) radio technology and indoor/topside propagation
- The modeling and design techniques will improve the time to production of antennas to meet the Navy mission for a multitude of needs

Major Performers

Virginia Polytechnic Inst. and St. U.,
Dr. William Davis
Dr. Warren Stutzman

TASK 1 Advanced Wireless Technologies

New antenna technologies applicable to Navy missions & hardware for AWINN Integration projects.

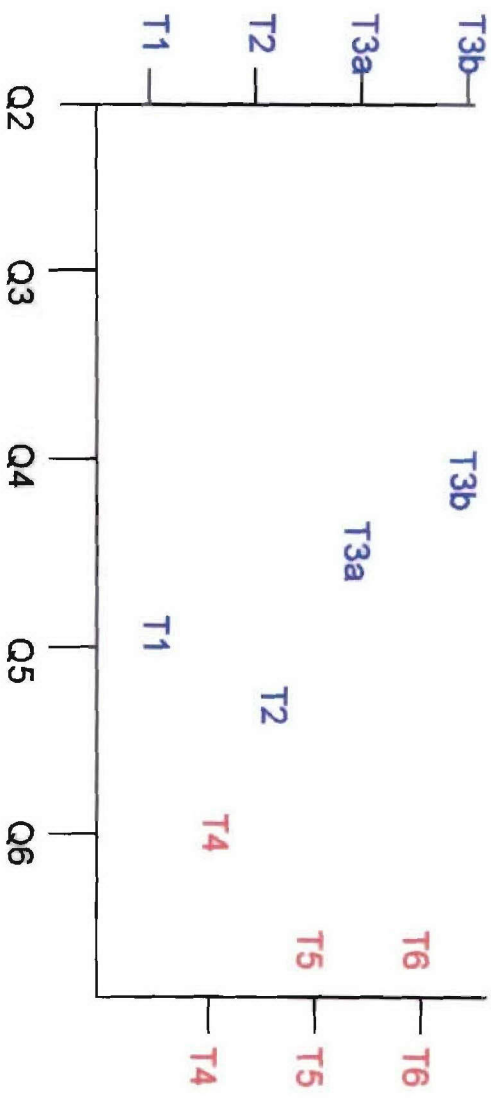
Task 1.1 Advanced Antennas

- Investigation of compact antennas for handheld and mobile terminals
- Antenna Characterization – transient & wideband
- UWB antenna design (support of AWINN demonstrations)
- Antennas providing polarization, spatial, and pattern diversity – Evaluation of antennas in a MIMO environment
- Support physics/engineering-based models for Digital Ships
- Wideband balanced antenna/array feed networks

Impact

- Potential new techniques for design of antennas and propagation channels to more effectively used the mission environment, particularly for applications requiring small antennas if frequency flexibility. The techniques also offer the potential of simplifying the topside design of the electromagnetic environment.

Task 1 Advanced Wireless Technologies
Task 1.1 Advanced Antennas



T1: Mobile Design **T2: Characterization** **T3a: SDR Antennas** **T3b: Sea-Base Antennas**

T4: Diversity **T5: Physics Models** **T6: Wideband Array Feeds**

1.2 Task 1.2 Advanced Software Radio

1.2.1 Overview

Task Goal: This task investigates an advanced Software Defined Radio (SDR) which can take advantage of the unique properties of Ultra Wideband communication—such as precision position location, ranging, and low probability of intercept—for Navy applications.

Organization: This task is managed by the Deputy Director of the Mobile and Portable Radio Research Group (MPRG) using the following personnel:

Jeffrey H. Reed, director
R. Michael Buehrer, faculty
William H. Tranter, faculty
Chris R. Anderson, GRA
Swaroop Venkatesh, GRA
Jihad Ibrahim, GRA
Maruf Mohammad, GRA

Summary: This quarter we focused on evaluating the prototype SDR receiver. For ranging and position location, initial algorithms were developed and tested in a simple proof-of-concept laboratory environment. The results indicate that ranging accuracy should be within a few inches, and that position location via evaluation of the multipath delay profile is possible. These algorithms are currently being updated to provide full 3-D ranging and positioning information, as well as to incorporate the use of the SDR receiver.

1.2.2 Task Activities for the Period

Subtask 1.2a Develop flexible software radio platforms that include cross-layer optimization with capabilities for UWB and ad hoc networking

Task objective: The overall goal of this subtask is to design an advanced software-defined/reconfigurable radio which is optimized for ultra wideband communication, and then implement the system using off-the-shelf components. The software-defined radio implementation provides tremendous flexibility compared to a single hardware implementation—for example, providing the capability to utilize one of several different popular UWB modulation or multiple access schemes, to operate in one of several modes (communication, ranging, or data capture), as well as to utilize more traditional broadband communication schemes.

Accomplishments during reporting period: This quarter we focused on the development of the RF Front End of the UWB Transceiver Testbed. In keeping with the design objective to produce an extremely flexible, general-purpose transceiver, the RF front end consists of only the most basic elements: a transmitter/receiver switch, low noise amplifiers and filters, and a digital step attenuator. To save cost and time, the RF front end was implemented with discrete MiniCircuits components, although a provision was included for a custom-designed RF board to be added at a later time. A block diagram of the RF Front end is given in Figure 1.2-1. The specific components, along with some important parameters used in each block, are listed in Table 1.2-1.

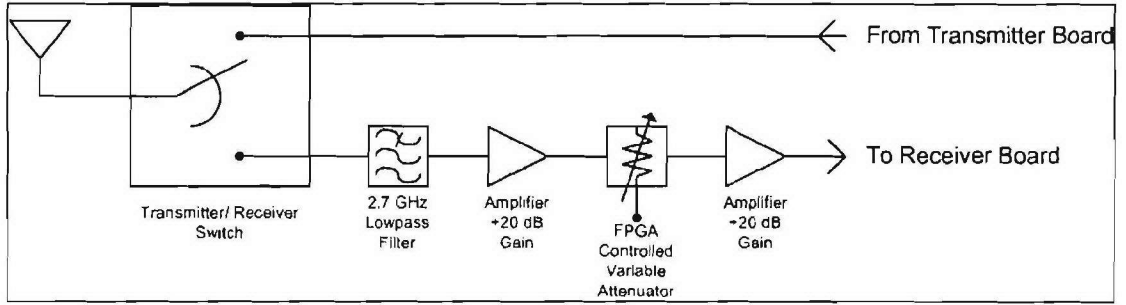


Figure 1.2-1 A block diagram of the RF Front End of the UWB Transceiver Testbed.

Table 1.2-1 Components and Component Parameters for the UWB SDR RF Front End					
	Part Number	Gain (dB)	Noise Figure (dB)	Bandwidth (MHz)	IP3 (dBm)
Tx/Rx Switch*	ZSDR-230	-1.3	1.3	10-3000	N/A
Lowpass Filter*	SLP-2950	-0.4	0.4	DC – 2950	N/A
RF Amplifier*	ZX60-3018G	20	2.7	0.02 – 3000	25.0
Variable Attenuator**	HMC307QS16G	-1.8 – -31	-1.8 – -31	DC – 4000	N/A

* MiniCircuits Part

** Hittite Microwave Part

- Receiver Sensitivity, Gain, and Linearity

One of the important design tradeoffs in the RF front end was to provide enough gain to allow the receiver to operate at or near the desired 10 meter range while still preserving an approximately 40 dB dynamic range. At 2 GHz, free space path loss is roughly 60 dB, which provided a starting point for the design. The first step in the design process was to calculate the noise floor for the receiver, using the following equation:

$$P_N = kTB$$

where P_N is the noise floor (Watts) k is Boltzmann's constant ($1.38 \times 10^{-23} \text{ J/K}$), T is the effective noise temperature of the receiver (expressed in Kelvin), and B is the receiver's bandwidth (Hz).

The overall receiver's noise figure is given by the following equation:

$$nf_{\text{cascade}} = nf_1 + \sum_{i=2}^N \frac{nf_i - 1}{\prod_{j=1}^{i-1} g_j}$$

where N is the number of noise-producing elements in the receiver chain, nf_i is the noise figure of the i^{th} element (in linear units), and g_j is the gain of the j^{th} element in the receiver chain (in linear units). Note that for passive devices (e.g., an attenuator, or a filter), the noise figure is

equal to the loss of the device. The noise figure of the cascaded system can then be converted into an effective noise temperature via the following equation:

$$T_N = 290(nf_{\text{cascade}} - 1)$$

where T is the effective noise temperature (in Kelvin) and nf_{cascade} is the overall receiver's noise figure (in linear units).

Using two amplifiers in the RF front end results in a noise figure of

$$NF = 4.8 \text{ dB}$$

$$T_N = 586 \text{ }^\circ\text{K}$$

and a noise floor of

$$P_N = -77.5 \text{ dBm}$$

Because the amplifiers amplify both the noise and the desired signal, the maximum amount of gain that can be supplied by the RF front end is:

$$G_{\text{Max}} = ADC_{\text{MAX}} - DR - P_N$$

where ADC_{MAX} is the maximum allowed input to the receiver's ADC array, DR is the desired dynamic range of the receiver, and P_N is the noise floor of the receiver.

Since the MAX104 ADC can tolerate a maximum input signal strength of 0 dBm (an input amplitude of +/- 250 mV), from the above equations, it can be seen that the RF front end can have a gain of no greater than 37.5 dB, which is met by the above configuration. A gain of ~40 dB is, however, insufficient for the receiver to operate at the desired maximum range of 10 meters. Fortunately, the expected peak transmitter power is in the range of 15-19 dBm, which should be adequate for LOS or low-multipath channels, depending on the gains/losses of the antennas. In NLOS or dense multipath environments, it may be necessary to either add a power amplifier to the transmitter, or compromise the dynamic range of the receiver by adding an additional amplifier to the RF front end.

Another important parameter of the RF front end is amplifier linearity, which can be characterized by the third-order intercept point (IP3). IP3 is a figure-of-merit for amplifier linearity or distortion, where higher IP3 means better linearity and less distortion. In mathematical terms, IP3 is a theoretical input power point at which the fundamental and third-order harmonic distortion (which is generated due to nonlinearities in the amplifier) output lines intersect, as illustrated in Figure 1.2-2a. In practice, the IP3 determines the amplitude of the third-order harmonic signals relative to the amplitude of the fundamental signal, as illustrated in Figure 1.2-2b.

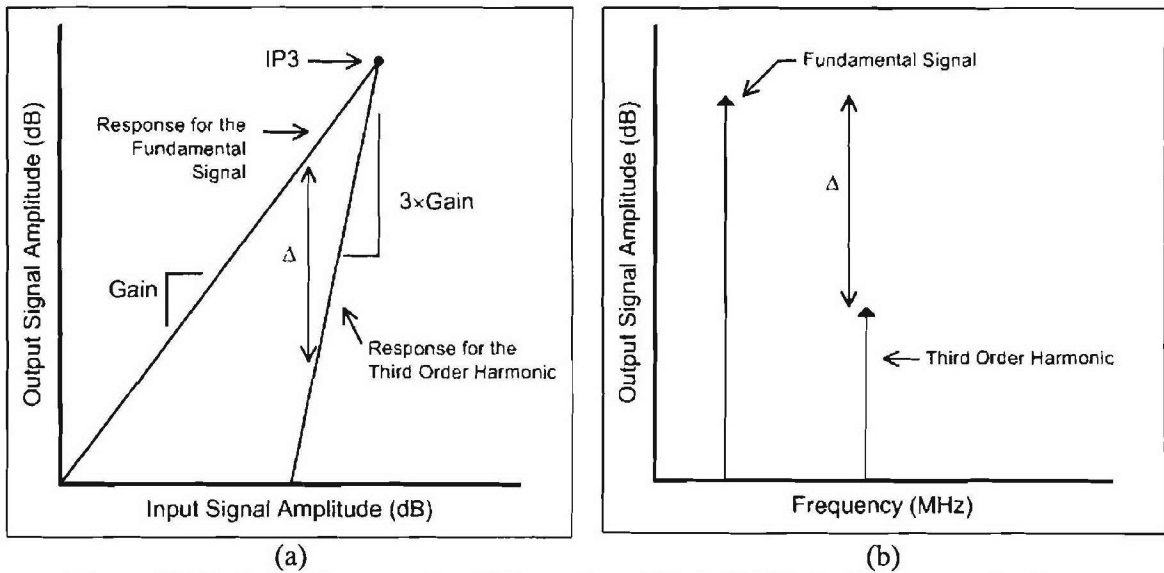


Figure 1.2-2 A simple narrowband illustration of the Third Order Intercept point for an amplifier. (a) For a given input signal and amplitude, the amplifier produces an amplified output signal, along with a third harmonic signal. The point at which the output powers of the fundamental signal and the third harmonic are equal is the IP3. (b) Illustration of the relative amplitude of the fundamental signal and the third order harmonic.

UWB signals, on the other hand, have no single fundamental signal—although they could be broken into a sum of sinusoids via a Fourier Series. Hence, the third-order harmonic signals will all fall within the UWB signal’s bandwidth, resulting in a distortion of the UWB pulse. Thus, for UWB signals, instead of measuring the relative amplitude of the third-order signals, the amount of pulse distortion for a given amplifier IP3 must be characterized.

To characterize the impact of IP3 on the UWB pulse input to the RF front end, a series of simulations were performed in Agilent’s EESof ADS. A schematic diagram of the simulation (which consisted of the 2.95 GHz input filter, two amplifiers, and the 2.4 GHz filter on the Digital Board) is given in Figure 1.2-3. The amplitude of the UWB pulse input to the RF front end was set such that the output pulse would have an amplitude equal to the maximum allowed input for the MAX104 ADCs (i.e., +/- 250 mV). Four different simulations were performed, with IP3’s ranging from 0 dBm to +25 dBm (which corresponds to the IP3 for the MiniCircuits ZX60-3018G). Simulation results are shown in Figure 1.2-4. Note that very low values for IP3 (0 dBm and +5 dBm) generate a tremendous amount of distortion; however, for IP3’s above +10 dBm, the amplifier imparts almost no distortion on the UWB pulse.

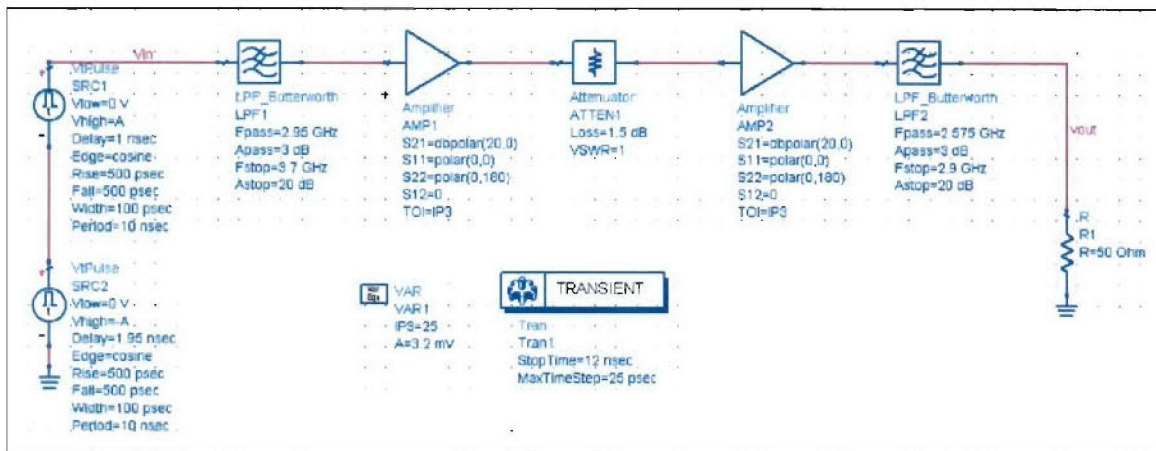


Figure 1.2-3 ADS Schematic diagram of the UWB Receiver RF Front End for simulating the UWB pulse distortion caused by amplifier IP3.

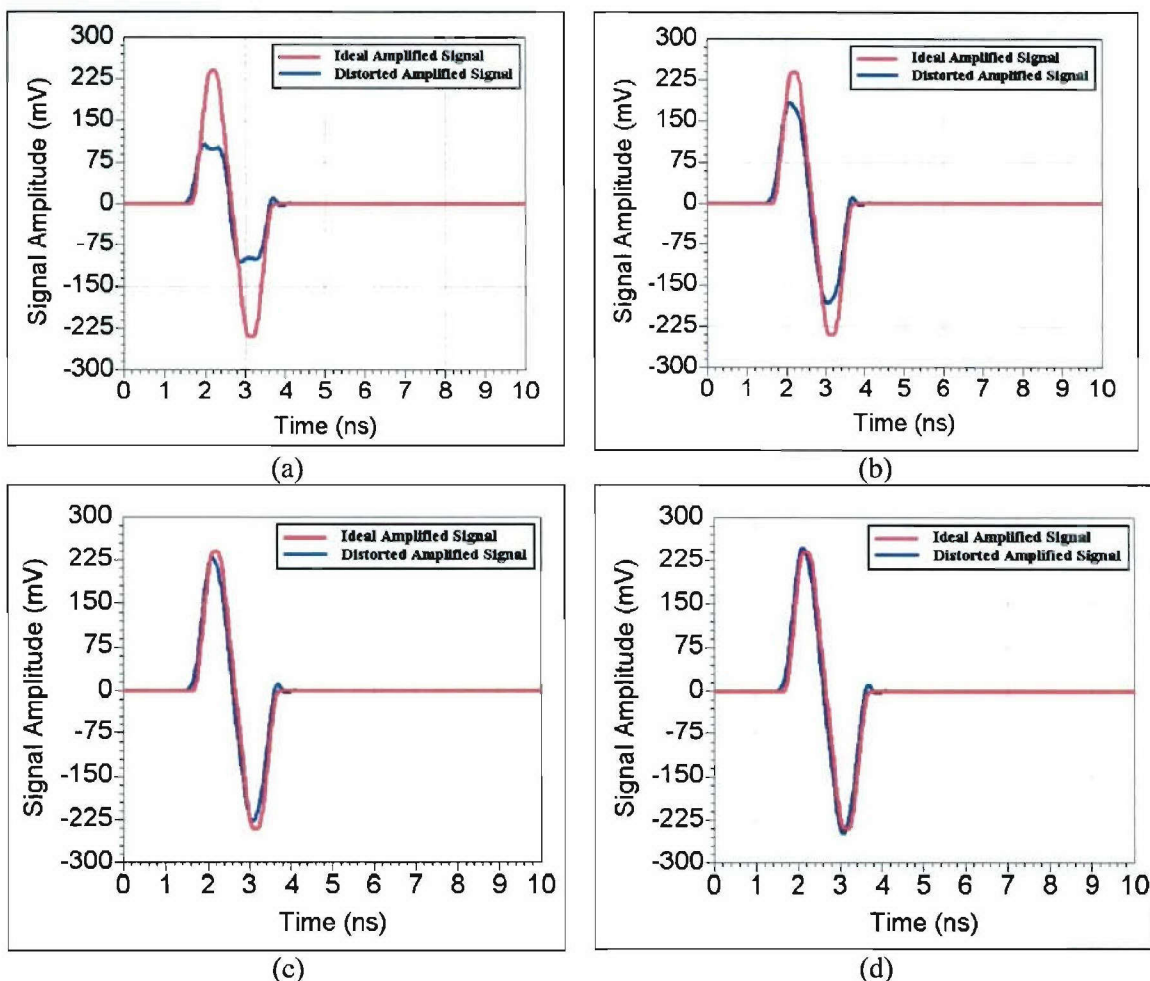


Figure 1.2-4 Illustration of pulse distortion due to the effects of amplifier IP3. Distorted pulses are shown along with the ideal amplified pulse (i.e., if the amplifier had infinite IP3). (a) Amplifier IP3 of 0 dBm, (b) Amplifier IP3 of +5 dBm, (c) Amplifier IP3 of +10 dBm, and (d) Amplifier IP3 of +25 dBm.

- Filter and Attenuator

The Mini-Circuits SLP-2950 low pass filter simply serves as a bandlimiting pre-select filter on the RF front end. Its purpose is to prevent out-of-band signals from overdriving either the RF amplifiers or the ADCs. Additionally, it serves to help bandlimit the amount of noise allowed to enter the receiver, an important feature given the dynamic range requirements and noise issues discussed above. Note that the 3 dB bandwidth of the SLP-2950 (2.95 GHz) is significantly greater than the 3 dB bandwidth of the MAX104 ADCs (2.2 GHz). However, the SLP-2950 provides an extremely flat frequency response across the entire DC-2.2 GHz range (< XXX dB ripple), and thus should impart minimal or no distortion to the received signal. Additional filtering, if desired, can be added to the RF front end, or on the Digital Board.

Finally, The Hittite Microwave HMC307QS16G is a DC-4 GHz digital step attenuator that provides 2 – 32 dB of attenuation in 1 dB step sizes. The variable attenuator is used in the RF front end as an automatic gain control (AGC). The UWB SDR transceiver uses a very basic AGC algorithm by monitoring the ADCs overrange bits, as well as the ADCs two most significant bits. If the overrange bit is set for any one of the ADCs, then the receiver will increase the attenuation. Conversely, if the received signal fails to assert the two most significant bits in any of the ADCs, the receiver will decrease the attenuation. More sophisticated ADC algorithms can easily be implemented as well, due to the highly programmable/reconfigurable nature of the transceiver.

Schedule:

-
- January-June 2006
 - Develop 8-ADC Full Receiver
 - Begin Integration of Receiver with Other AWINN Activities
- January - March 2006
 - Fabricate 8-ADC Full Receiver
 - Fabricate Transmitter Design
 - Fabricate RF Front End
 - Fabricate DC Power Board
 - Verify Operation of Receiver Hardware and FPGA Code
- April – June 2006
 - Demonstrate Transceiver Operation
 - Integrate Transceiver with Other AWINN Activities
-

Personnel:

Chris R. Anderson – Transmitter and Receiver Hardware Development
 Matt Blanton – Receiver FPGA Code Development

Subtask 1.2b Software radio research applied to UWB, including design parameter space exploration.

Task objective: The objective of this task is to investigate innovative SDR architectures and algorithms for both traditional broadband and UWB communications. These algorithms will be implemented on the advanced SDR receiver developed in Subtask 1.2a.

Accomplishments during reporting period: The previous work on NBI mitigation based on a selection diversity system (Figure 1.2-5) was based on an ideal UWB receiver, where perfect channel knowledge was assumed. The template of the UWB correlator-receiver was set to the received UWB signal shape, and thus complete energy capture was achieved.

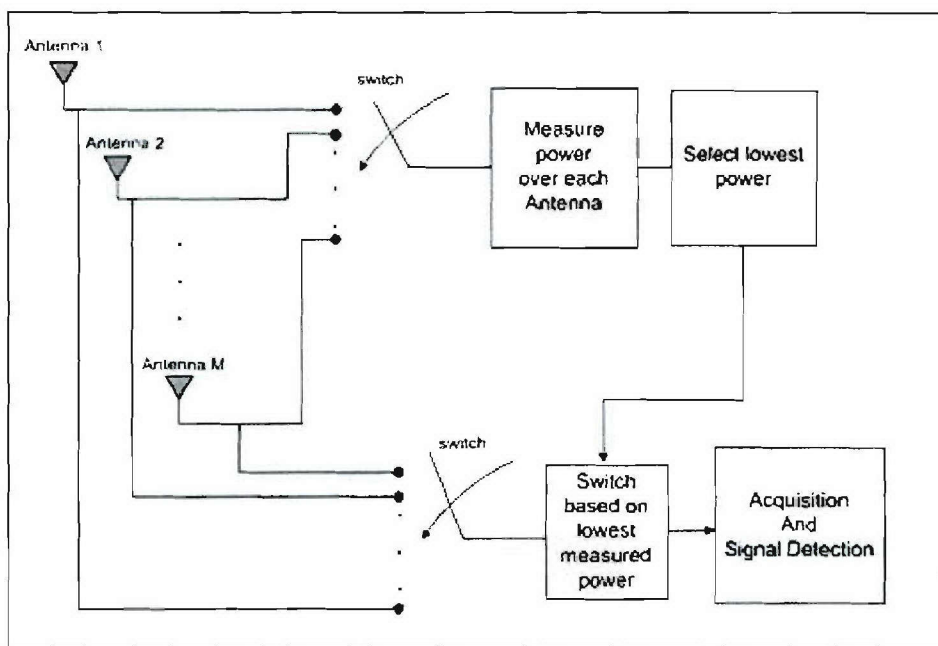


Figure 1.2-5 Selection Diversity System Model.

Here, the work is extended to a more realistic UWB Rake receiver with F fingers, employing MRC. It is assumed that the delay and magnitude of the F strongest multipath components are known, and the energy contained in these F components is gathered at the receiver.

- Antenna Energy Variation for a Rake Receiver

Recall that, under the assumption of perfect energy capture, the variance of the measured UWB power across receiver antennas is very small, and power is assumed constant across all antennas. If a Rake receiver is used, more energy fluctuation is predicted across antennas.

The energy capture for a Rake receiver employing F fingers was analyzed. The cumulative normalized energy harnessed by these fingers was recorded for multiple locations over a 1 m^2 grid. It was shown that the Rake energy level varies more significantly than the total energy capture case. For example, the energy variance for a 10-finger Rake when normalized to unit mean is equal to 0.0273, compared to a variance of 0.0035 for the perfect energy capture case. However, the energy variance is still relatively small compared to the NBI case. Moreover, it was

found that the energy capture, d , across multiple antennas may be approximated by a Laplace random variable; see Figure 1.2-6 with distribution given by:

$$f_d(x) = \frac{1}{\sigma_d \sqrt{2}} e^{-\frac{\sqrt{2}|x-\bar{d}|}{\sigma_d}}, \text{ where } \bar{d} \text{ is the average energy capture, } \sigma_d^2 \text{ is the energy capture}$$

variance, and $||\cdot||$ is the absolute value operator.

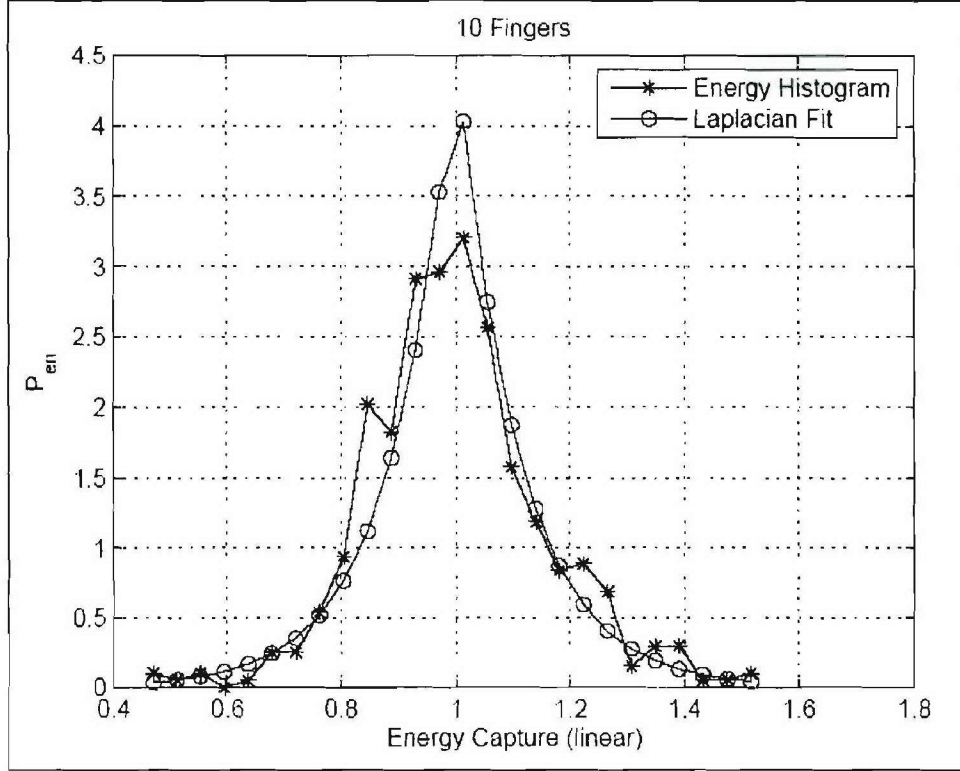


Figure 1.2-6 Normalized received UWB signal energy over a 1 m² area. 10-Finger Rake receiver.

A Kolmogorov-Smirnov statistical goodness of fit test was performed to test the Laplace distribution hypothesis, and the hypothesis passed the test for 5, 10, 15 and 20 fingers (Table 1.2-2). Thus we will use a Laplacian model for the captured Rake received energy with a variance dependent on the number of Rake fingers.

Table 1.2-2 Kolmogorov-Smirnov test for Laplacian fit of rake receiver energy capture. 580 sample points.

$$\text{Significance level} = 0.05. \text{ Test Threshold} = \sqrt{-\frac{1}{2 \times 580} \log\left(\frac{0.05}{2}\right)} = 0.0564$$

Receiver	σ_d^2	Test Statistic	Passed Test?
5-finger Rake	0.0439	0.0548	YES
10-finger Rake	0.0273	0.0454	YES
15-finger Rake	0.0199	0.0540	YES
20-finger Rake	0.0155	0.0477	YES

- Probability of Error

The probability of error of the proposed Rake system was derived. Similar to previous analysis performed for perfect channel knowledge, the decision statistic may be written as:

$r_m = \sqrt{E_p} b_0 d_m + i_m$, where E_p is the bit energy, b_0 is the bit, d_m is the desired UWB component, and i_m is the NBI component.

Assuming NBI Rayleigh fading, i_m is found to be a zero-mean Gaussian random variable with variance:

$\sigma_i^2 = 2N_f(a^2 + b^2)\frac{\sigma^2}{M}$, where N_f is the NBI power spectral density, a and b are constant

parameters depending on the NBI center frequency and on the correlator template, σ^2 is the NBI Rayleigh parameter, and M is the number of antennas. d_m is a Laplacian random variable as discussed earlier.

It can be shown that the probability of error of this system is given by:

$$P_e = Q\left(\sqrt{\frac{E_p \bar{d}^2}{\sigma_i^2}}\right) - \frac{1}{4} e^{-\frac{\sqrt{2}\bar{d}}{\sigma_d}} + \frac{1}{2} e^{\frac{\sigma_i^2}{E_p \sigma_d^2} \frac{\sqrt{2}\bar{d}}{\sigma_d}} \left[Q\left(\frac{-\sqrt{2}\sigma_i}{\sqrt{E_p \sigma_d}}\right) - Q\left(\sqrt{\frac{E_p \bar{d}^2}{\sigma_i^2}} - \frac{\sqrt{2}\sigma_i}{\sqrt{E_p \sigma_d}}\right) \right] - \frac{1}{2} \frac{\frac{\sigma_i^2}{E_p \sigma_d^2} + \frac{\sqrt{2}\bar{d}}{\sigma_d}}{Q\left(\sqrt{\frac{E_p \bar{d}^2}{\sigma_i^2}} + \frac{\sqrt{2}\sigma_i}{\sqrt{E_p \sigma_d}}\right)}.$$

For derivation details, the reader is referred to the reference at end of section.

Note that, in case of full energy capture (which is equivalent to a perfect Rake receiver with complete knowledge of the desired received UWB pulse shape), the desired component of the decision statistic may be assumed constant over M antennas. Equivalently, $\sigma_d = 0$, and the probability of error becomes:

$$P_e = Q\left(\sqrt{\frac{E_p M \bar{d}^2}{2N_f(a^2 + b^2)\sigma^2}}\right)$$

- Simulation Results

Performance of the proposed SD system applied to a 20-finger Rake receiver employing MRC combining is tested for NBI Rayleigh fading in Figure 1.2-7. The performance is plotted for simulation results, theoretical results assuming a Laplacian distribution for the desired signal component, and theoretical results assuming constant energy capture. Notice that, at low SIR values, diversity gains are practically equal to 3-dB when doubling M , and that both assumptions yield almost same performance. The variation in energy capture across antennas is negligible compared to the variation of the interference energy, and gains are similar to the full energy capture case. However, for high SIR values, the energy capture variation impacts performance, and the simulated probability of error is closer to the Laplacian approximation. At high SIR, the interference power variance across antennas becomes negligible, and performance is dominated by the fluctuation in UWB energy. Note that since SIR is measured at the output of the correlator, the average Rake energy capture is incorporated into SIR. In other words, we are interested in the variance of the energy over a local area, and not in its mean value. Also, it is important to note the distinction between the SD process applied at the power selection level, and the MRC process which occurs at the Rake finger combination level; the two processes are independent and must not be confused.

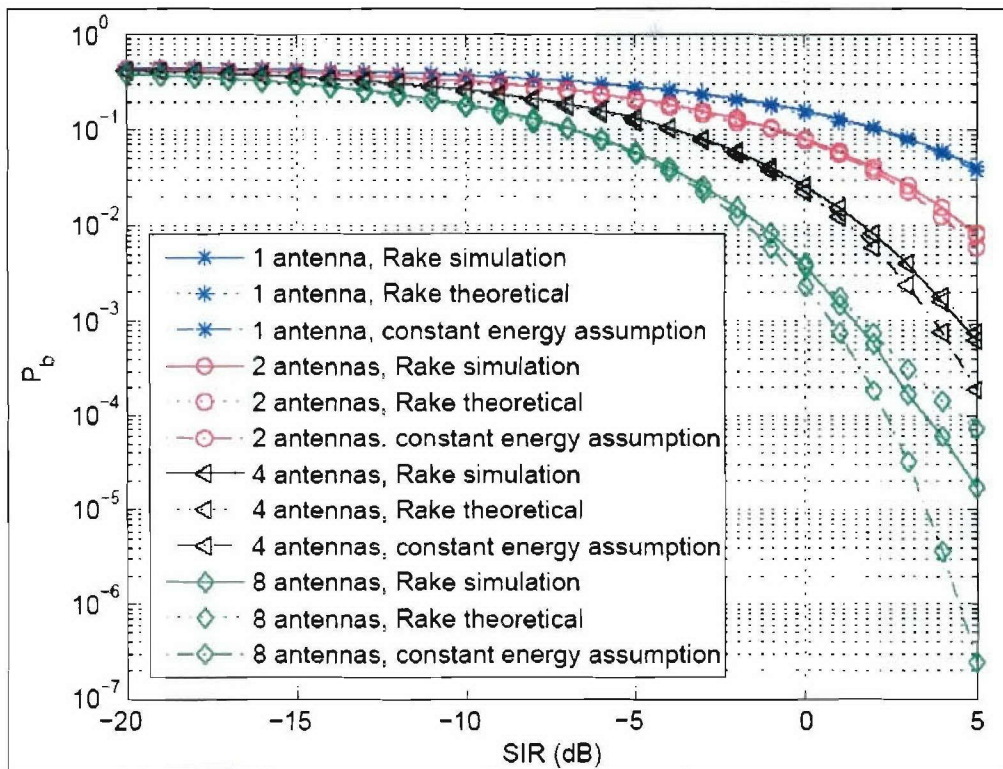


Figure 1.2-7 SD under NBI Rayleigh fading with a 20-Finger Rake for 1, 2, 4 and 8 antennas.

- Reference

J. Ibrahim and R.M. Buehrer, "NBI Mitigation for UWB Systems Using Multiple Antenna Selection Diversity," submitted to IEEE Transactions on Vehicular Technology, December 2005.

Subtask 1.2c Software radio designs for collaborative systems that take advantage of this radio, particularly for interference environments.

Please refer to Task 4, TIP #1.

Subtask 1.2d Vector channel models, including Markov Models, and supporting channel measurements.

Task objective: The objective of this task is to study techniques to find efficient ways to model error traces generated by real world wireless channels. Different discrete channel modeling methods will be implemented and their accuracy, consistency and robustness will be studied.

Accomplishments during reporting period: Real world wireless channels often contain memory and hence cannot be treated as an independent random process. It is not possible to model such data by using standard random variables available in literature. In such situations, Markov models have proved themselves to be a valuable tool in analyzing and modeling/reproducing the observed data. The natural candidates for this purpose are Markov Chains (MC) and hidden Markov models (HMMs) [Feller, Turin]. Both MC and HMMs are flexible enough to fit a wide variety of experimental data with high accuracy. Although we usually use MC and HMMs for modeling experimental data, semi-hidden Markov models (S-HMMs) have also become popular especially in the field of telecommunications [Howard, Turin]. This is primarily because of their significant rapidness in parameter estimation as compared to traditional Markov models.

To develop a certain Markov model based an observation, we need to estimate its parameters, i.e. the probability of transitioning from one state to another and the emission probabilities of every state (in HMM case). For this purpose, maximum likelihood estimate is used for MCs and Baum-Welch algorithm (BWA), a special case of Expectation Maximization (EM) algorithm, is usually used for HMM parameter estimation [Akbar]. A derived form of BWA is used for the parameter estimation of S-HMMs [Sivaprakasam, Turin]. Note that in all these estimation problems, we first have to assume a fixed number of states.

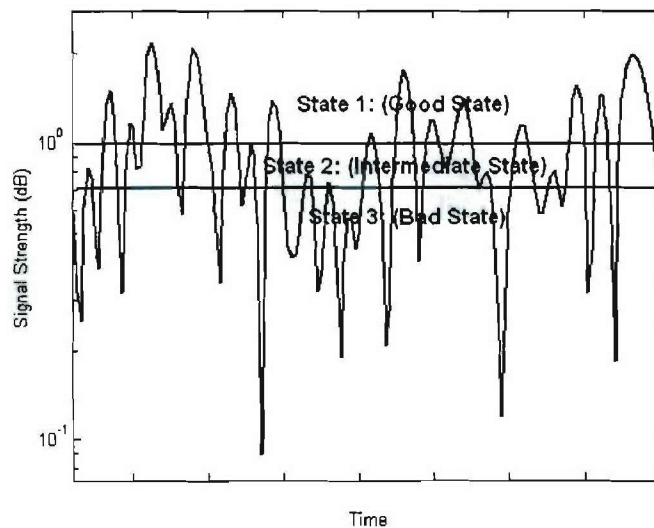


Figure 1.2-8 HMM realization of a fading envelope.

Although the theory of parameter estimation for the case of Markov processes is well established and understood, the work on estimating the order of these models just started in early 1990s. Finesso, in 1991, used the Law of Iterated Logarithms (LIL) and Information Theoretic measures to estimate the order of MCs and HMMs [Finesso]. Khundapur and Narayan recently proposed an

S-HMM order estimation [Khundapur] technique that assumes that the model has only one bad state. Recall that the order of a Markov process is defined as the minimum number of states required to model the data accurately. In MCs, this corresponds to the depth of memory of the process whereas in HMMs, the order corresponds to the number of quantized state levels. The state transition diagram of an N -state Markov process is shown in Figure 1.2-8.

The realization of HMM states in wireless channel is illustrated in Figure 1.2-9. The number of quantization levels of fading envelope constitutes different states, and every state can produce both 0s (no errors) and 1s (errors). However, in a good state, the probability of producing 0s is much higher than producing 1s. Note that even if we further divide a state into two sub-states (or in other words if we increase the number of states of HMM), the depth of the memory still remains the same.

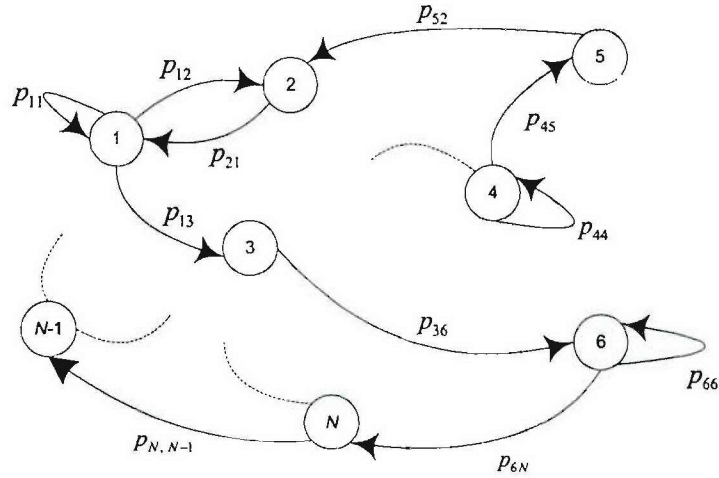


Figure 1.2-9 Illustration of different states of a Markov process and their transitions.

In this report we analyze the use of two important criteria that are used in estimating the order of Markov processes. These techniques are known as Bayesian information criterion (BIC) and Akaike's information criterion (AIC) [[MacDonald, Cappé]. Although there are some recent progress concerning the consistency of Markov chain BIC order estimation, the consistency of BIC in HMM order estimation is yet to be established satisfactorily [Cappé]. We have studied these two criteria in modeling and simulation of binary vector channels and we present some preliminary results on the order estimation of binary MC and HMMs using these two methods.

In the previous report, we investigated the problem of estimating the order of Markov chain using goodness of fit statistics. Recall that if $n(e_1, e_2, \dots, e_{k+1})$ denotes the frequency of transitions of error patterns e_1, e_2, \dots, e_{k+1} and $\hat{p}_{e_1 e_2 \dots e_{k+1}}$ are the corresponding probabilities, then we can write [Anderson, Billingsley]

$$I = \sum_{e_1, e_2, \dots, e_{k+1}} n(e_1, e_2, \dots, e_{k+1}) \ln(\hat{p}_{e_1 e_2 \dots e_{k+1}} / \hat{p}_{e_2 e_3 \dots e_{k+1}})$$

Here I is distributed asymptotically as $0.5 \chi^2$. The χ^2 criterion can also be written as

$$\chi^2 = \sum_{e_1, e_2, \dots, e_{k+1}} n^*(e_1, e_2, \dots, e_{k+1}) (\hat{p}_{e_1 e_2 \dots e_{k+1}} - \hat{p}_{e_2 e_3 \dots e_{k+1}})^2 / \hat{p}_{e_2 e_3 \dots e_{k+1}}$$

For large data samples we can replace $n^*(e_1, e_2, \dots, e_{k+1})$ with $n(e_1, e_2, \dots, e_{k+1})$. It is shown in [Turin] that for large data samples, $2I$ and χ^2 criteria are approximately equal.

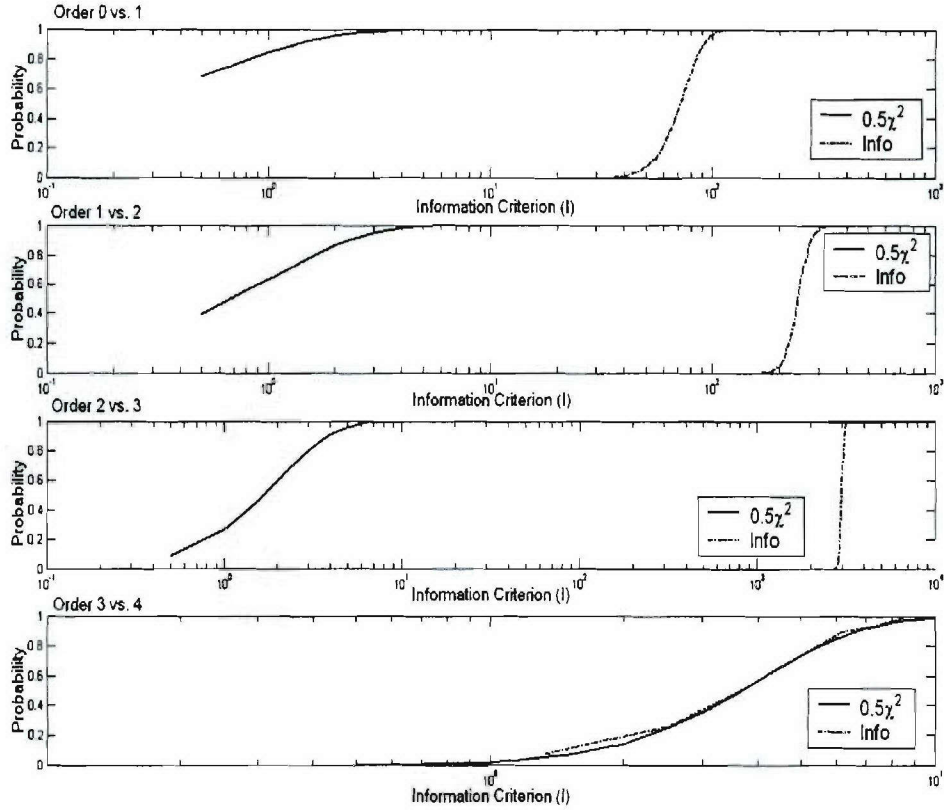


Figure 1.2-10 Markov chain order estimation using χ^2 goodness of fit criterion (true order is 3).

In a goodness of fit approach, we start with the hypothesis that the sequence is obtained from a binary symmetric channel with no memory and test this hypothesis against the hypothesis that it is obtained from a first-order Markov chain. If the above hypothesis is rejected, then we test the hypothesis that the sequence is drawn from a second-order Markov chain against the hypothesis that it is drawn from a first-order Markov chain. We keep testing until the correct order fits the experimental data reasonably well. A typical Markov chain order estimation result in which the true sequence is a third-order MC is shown in Figure 1.2-10. The goodness of fit method, although very accurate and consistent, requires very long simulation runtime. This is because we need to have large number of sequences to compare the resulting distribution with χ^2 statistics. In other words, we can not estimate the order of MC if we have a single or a limited number of observation sequences.

Identifiability Problem of a Binary Process

A random process Y is said to have a mixture distribution if its distribution depends on a quantity that also has a distribution. The density of random process Y given the density of g mixture components can be written as

$$f_Y(y) = \sum_{i=1}^g m_i f_i(y)$$

Where $f_i(y)$ are the densities, m_i are nonnegative quantities that sum to one and g is the number of mixture components. It is interesting to note that marginal distributions of Y (where Y is a HMP) given X , the underlying state sequence, is a finite mixture process [McLachlan].

$$f_Y(y_t) = \sum_{k=1}^N \pi_k f_Y(Y_t = y_t | X_t = k)$$

Here π_k is the stationary distribution of states and N is the total number of states.

Most of the order estimation techniques that we have studied so far are based on the fact that the marginal distribution of the observation sequence is a finite mixture model and estimating the order of the HMM corresponds to the estimation of the number of mixture components. This requires the finite mixture model to be identifiable. A function is “identifiable” if and only if it is one-to-one [Rao]. Mathematically, for any function to be identifiable,

$$f(\eta) = f(\mu) \Leftrightarrow \eta = \mu \quad \forall \eta, \mu$$

This is not true for binary processes and can be shown by a simple example. If a process Y can be modeled as a mixture of binomial distributions with parameters p_1 and p_2 , then we can write

$$\begin{aligned} f_Y(y) &= \Pr(Y = y) \\ &= \Pr(Y = y | p_1) \Pr(p = p_1) + \Pr(Y = y | p_2) \Pr(p = p_2) \quad y = 0, 1 \\ &= \binom{1}{y} p_1^y (1 - p_1)^{1-y} \Pr(p = p_1) + \binom{1}{y} p_2^y (1 - p_2)^{1-y} \Pr(p = p_2) \end{aligned}$$

Let $\Pr(p_1) = \alpha$, then $\Pr(p_2) = 1 - \alpha$

$$\begin{aligned} \Pr(Y = 0) &= \binom{1}{0} p_1^0 (1 - p_1)^{1-0} \alpha + \binom{1}{0} p_2^0 (1 - p_2)^{1-0} (1 - \alpha) \\ &= \alpha(1 - p_1) + (1 - \alpha)(1 - p_2) \\ \Pr(Y = 1) &= \binom{1}{1} p_1^1 (1 - p_1)^{1-1} \alpha + \binom{1}{1} p_2^1 (1 - p_2)^{1-1} (1 - \alpha) \\ &= \alpha p_1 + (1 - \alpha) p_2 \end{aligned}$$

Here there are two equations and three unknowns, so we can have infinite solutions.

Likelihood of Binary Markov Processes

If we denote by n_{ij} the number of transitions from state i to state j and a_{ij} as their corresponding probabilities, then the likelihood of process e_1, e_2, \dots, e_T can be written as

$$P(e_{1:T}) = \sum_{i=1:N} \sum_{j=1:N} n_{ij} \log(a_{ij})$$

Given an error sequence, the parameters and likelihood of MC of certain order are fixed numbers, and can be obtained by assigning different basis sequences to different states and observing the number of times a particular state is visited. This is not the case with HMMs where the likelihood is calculated as

$$P(e_{1:T}) = \sum_{i_1=1:N} \dots \sum_{i_T=1:N} \pi \mathbf{B}(e_1) \mathbf{P} \mathbf{B}(e_2) \mathbf{P} \dots \mathbf{P} \mathbf{B}(e_T) \mathbf{1}'$$

Here π is the stationary distribution of states and $\mathbf{B}(e_i) = \text{diag}(\mathbf{b}_{e_i+1})$.

The likelihood of a Markov process increases as we increase the number of states [Finesso, Gassiat]. This is always found to be true in MC case but not in HMMs as the Baum-Welch algorithm, used for estimating the parameters of HMMs, can be stuck at local maxima of likelihood, and the likelihood in this case could be less than the likelihood found for HMMs of smaller order. To fix this problem, we run BWA several times with different initial conditions and pick the hidden Markov model (of a certain order) that gives the maximum value of likelihood. However, note that this doesn't guarantee to obtain an optimum model (global maximum) because there are infinite possibilities of initial conditions and checking all of them is quite impossible.

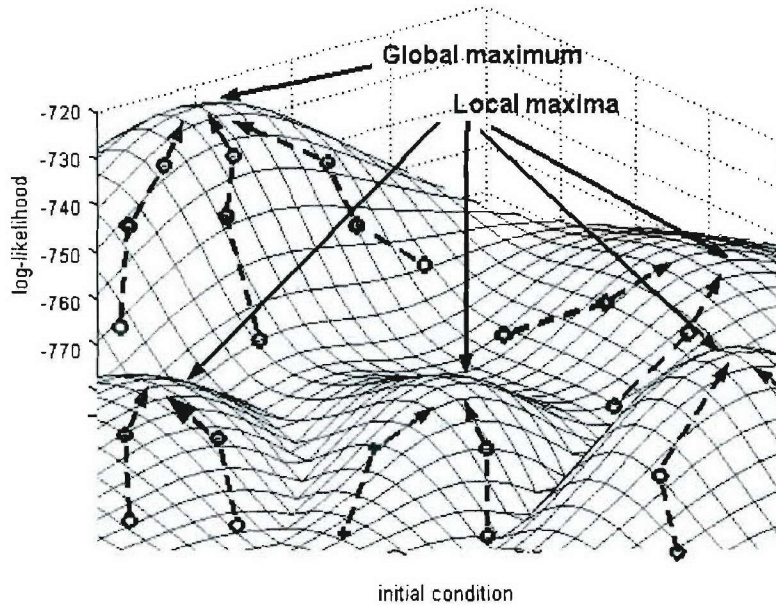


Figure 1.2-11 Profile of log-likelihood surface during HMM parameter estimation using BWA.

A graphical illustration of BWA estimation of HMM parameters and its convergence on log-likelihood surface is shown in Figure 1.2-11.

Auto-Correlation Functions of Markov Processes

The Markov chain state transition matrix \mathbf{P} can be decomposed in Jordan canonical form and can be written as $\mathbf{V}\mathbf{J}\mathbf{V}^{-1}$.

$$\mathbf{V} = [\mathbf{1}' \ \mathbf{R}], \quad \mathbf{V}^{-1} = \begin{bmatrix} \boldsymbol{\pi} \\ \mathbf{W} \end{bmatrix} \quad \mathbf{J} = \begin{bmatrix} 1 & 0 \\ \mathbf{0}' & \boldsymbol{\Psi} \end{bmatrix}$$

If we let $\mathbf{v} = [1 \ 2 \ 3 \dots N]$ and $\mathbf{V} = \text{diag}(\mathbf{v})$, then the auto-correlation function (ACF) of MC can be written as

$$\rho_k = \frac{(\boldsymbol{\pi} \mathbf{V} \mathbf{R}) \boldsymbol{\Psi}^k (\mathbf{W} \mathbf{v}')}{\boldsymbol{\pi} \mathbf{V} \mathbf{R} \mathbf{W} \mathbf{v}'}$$

For the case of binary HMM, we treat a binary hidden Markov processes as a binomial(n, d) random process with number of trials $n = 1$ (basically a Bernoulli trial conditioned on current state) and let d_i as the probability of generating an error in state i . If we define a vector $\mathbf{d} = [d_1 \ d_2 \dots d_m]$ and a matrix $\mathbf{D} = \text{diag}(\mathbf{d})$, with the elements of \mathbf{d} on the main diagonal, then the auto-correlation function of a HMM can be written as

$$\rho_k = \frac{(\boldsymbol{\pi} \mathbf{D} \mathbf{P} \mathbf{d}) - (\boldsymbol{\pi} \mathbf{d}')^2}{(\boldsymbol{\pi} \mathbf{d}') - (\boldsymbol{\pi} \mathbf{d}')^2}$$

Bayesian Information Criterion and Akaike's Information Criterion

Let k be the dimension of a Markov model and n be the length of observation sequence, then the BIC order estimator is defined as

$$\hat{r}_n := \arg \min_{P \in M^r} \left[-2(\sup \log P(y_{1:n})) + k \log(n) \right]$$

The BIC is a special case of penalized maximum likelihood order estimators. It was introduced by Schwarz in late 1970s using Bayesian reasoning. For MCs, this theorem is established by Csiszár and Shields [Csiszár]

For a stationary irreducible Markov chain process with distribution P^* and of order r^* , the BIC order estimator converges to r^* - almost surely.

For a complete proof of this theorem, refer to [Cappé, Csiszár]. At this point, we don't have any proof on the consistency of BIC HMM order estimator, but we are hopeful to follow the theory of BIC estimator for MC to establish the consistency of BIC order estimator in general HMM setting.

The AIC is defined as

$$\hat{r}_n := \arg \min_{P \in M^r} \left[-2(\sup \log P(y_{1:n})) + 2k \right]$$

In the next section, we present some simulation results on Markov order estimation on some artificially generated data.

Simulation Results

Case 1: First-Order Markov Chain

An error sequence is generated from a second-order Markov chain. Different MCs and HMMs are developed and AIC and BIC are then calculated for each of these models based on their likelihood. The results are shown in Table 1.2-3.

Table 1.2-3 AIC and BIC results for different Markov Processes (original sequence is a first-order binary Markov Chain)

model	k	$-l$	AIC	BIC
Independent	1	768.9626	1.5339×10^3	1.5455×10^3
first-order MC	2	732.9876	1.4661×10^3	1.4773×10^3
second-order MC	4	732.1630	1.4701×10^3	1.4925×10^3
third-order MC	8	726.8199	1.4781×10^3	1.5229×10^3
2-state HMM	4	733.8313	1.4757×10^3	1.4981×10^3
3-state HMM	9	731.6999	1.4814×10^3	1.5318×10^3
4-state HMM	1	731.0626	1.4941×10^3	1.5837×10^3

6

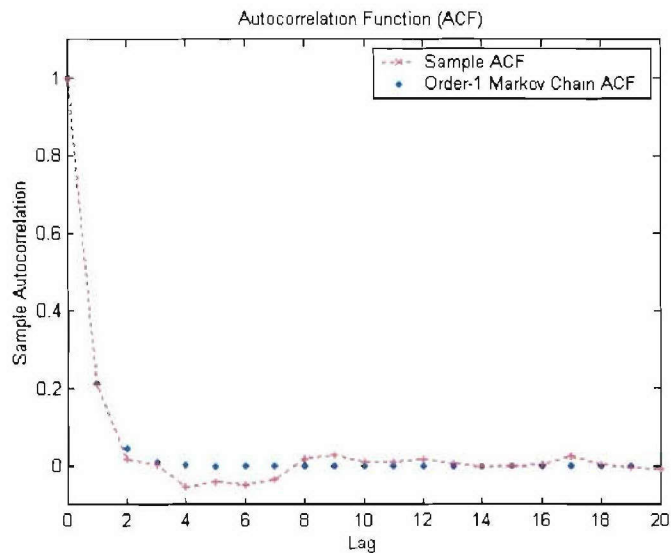


Figure 1.2-12 First 20 lags of sample ACF and order-1 MC ACF.

It is found that the AIC and BIC both select first-order Markov Chain as the best candidate to model the given data. The ACFs of first-order MC, 2-state HMM and 3-state HMM are plotted in Figures 1.2-12, 1.2-13, and 1.2-14 and compared with the sample auto-correlation.

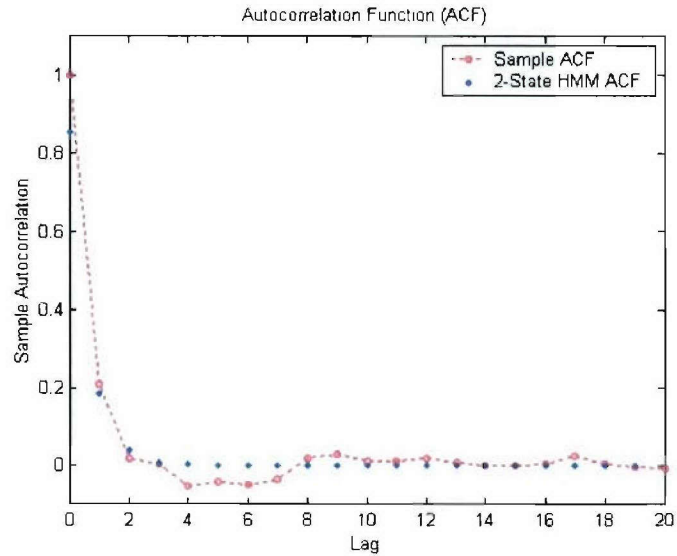


Figure 1.2-13 First 20 lags sample ACF and 2-state HMM ACF.

It can be seen from the plots that first-order MC and 2-state HMM map the original ACF better than a 3-state HMM.

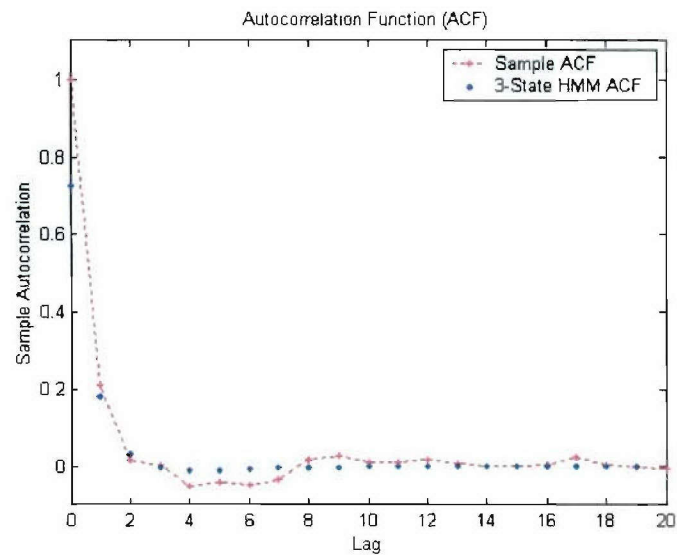


Figure 1.2-14 First 20 lags of sample ACF and 3-state HMM ACF.

Case 2: Second-Order Markov Chain

In the second case, a second-order MC is generated and different Markov models are developed. Table 1.2-4 shows the values of AIC and BIC obtained for these models. Both AIC and BIC pick the second-order MC as the best candidate.

Table 1.2-4 AIC and BIC results for different Markov Processes (original sequence is a second-order binary Markov Chain)

model	k	$-l$	AIC	BIC
independent	1	735.7232	1.4374×10^3	1.4789×10^3
first-order MC	2	734.7704	1.4735×10^3	1.4844×10^3
Second-order MC	4	672.4514	1.3529×10^3	1.3747×10^3
third-order MC	8	670.2456	1.3565×10^3	1.4000×10^3
2-state HMM	4	724.1406	1.4563×10^3	1.4780×10^3
3-state HMM	9	697.5232	1.4130×10^3	1.4620×10^3
4-state HMM	1	677.4835	1.3870×10^3	1.4740×10^3

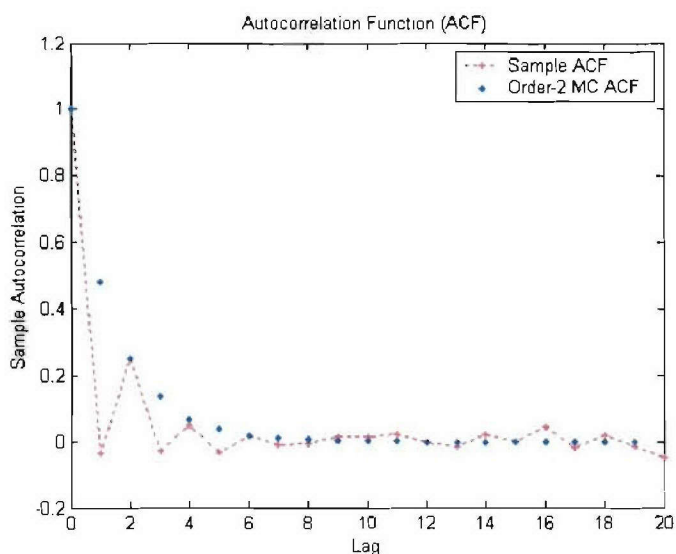


Figure 1.2-15 First 20 lags of sample ACF and second-order MC ACF.

First-order MC, second-order MC and 4-state HMM ACFs are calculated and plotted along with the ACF generated from the observation sequence. The second-order MC seems to be the best fit here.

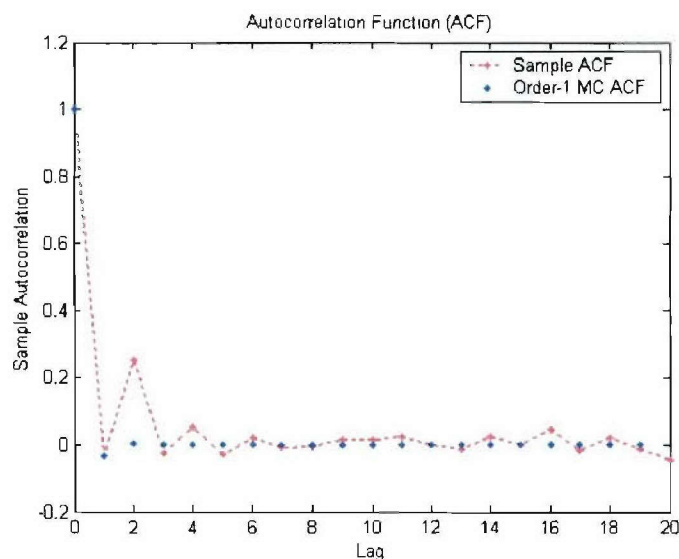


Figure 1.2-16 First 20 lags of sample ACF and first-order MC ACF.

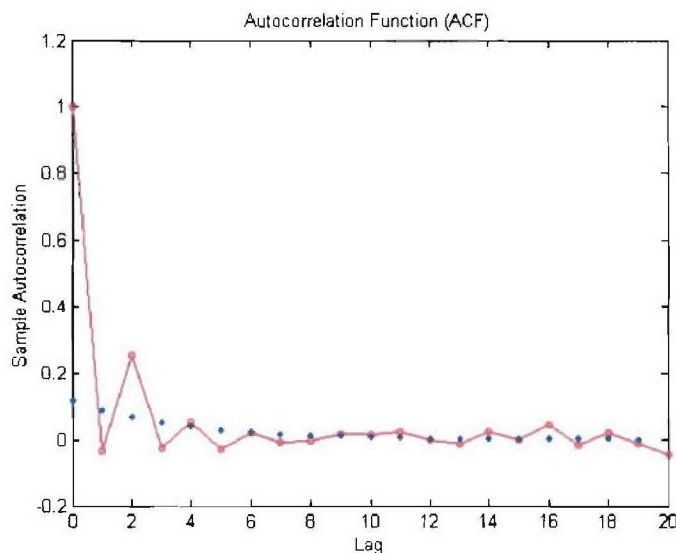


Figure 1.2-17 First 20 lags of sample ACF and 4-state HMM ACF.

Case 3: Three-State HMM

In case 3, a three-state HMM is generated. In this case, both AIC and BIC pick a 2-state HMM instead of a 3-state HMM as the best candidate. This is a consistent result that we have found that in case of binary HMM, AIC and BIC both usually pick a 2-state HMM as the best candidate. We are further investigating this in more detail and we wish to find the theoretical reasoning of this behavior of AIC and BIC order estimator.

Table 1.2-5 AIC and BIC results for different Markov Processes (original sequence is a three-state binary HMP)

model	k	$-l$	AIC	BIC
independent	1	776.6481	1.5553×10^3	1.5605×10^3
first-order MC	2	760.2741	1.5245×10^3	1.5349×10^3
Second-order MC	4	752.1174	1.5122×10^3	1.5329×10^3
third-order MC	8	734.0367	1.4841×10^3	1.5254×10^3
2-state HMM	4	734.4222	1.4768×10^3	1.4975×10^3
3-state HMM	9	734.4220	1.4868×10^3	1.5334×10^3
4-state HMM	1	729.6323	1.4913×10^3	1.5740×10^3

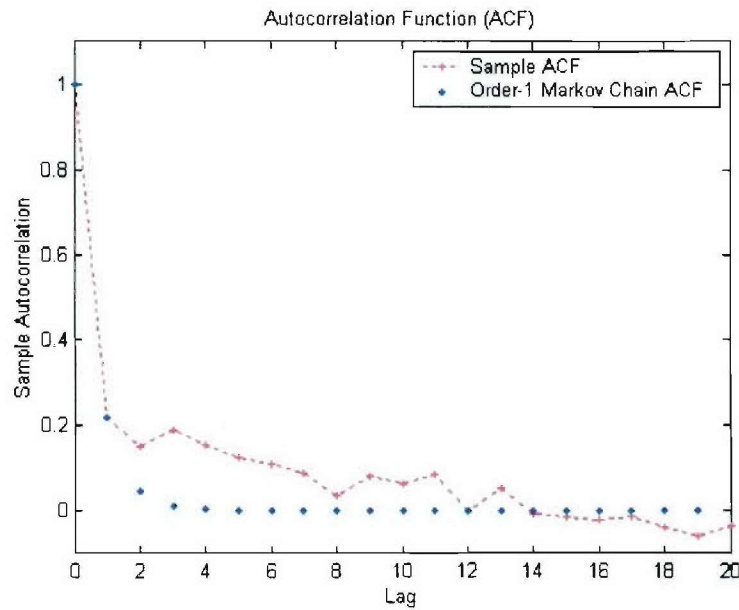


Figure 1.2-18 First 20 lags of sample ACF and first-order MC ACF.

ACFs are plotted in Figures 1.2-18, 1.2-19 and 1.2-20. The first-order MC (having relatively high values of AIC and BIC) doesn't seem to fit the sample data.

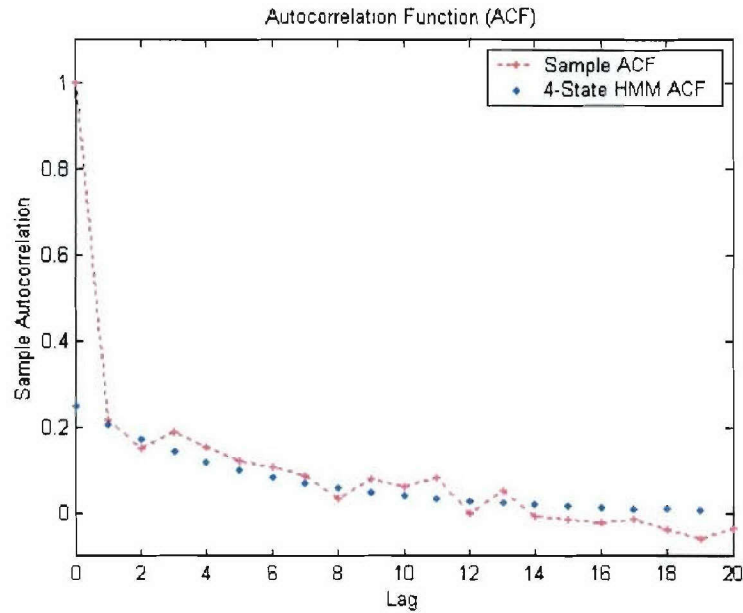


Figure 1.2-19 First 20 lags of sample ACF and 4-state HMM ACF.

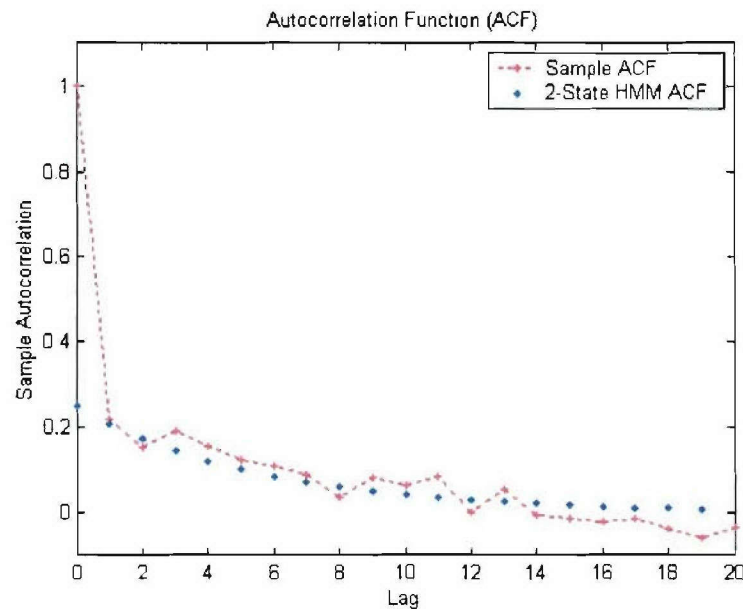


Figure 1.2-20 First 20 lags of sample ACF and 2-state HMM ACF.

Conclusion

We studied AIC and BIC order estimation techniques on artificially generated error sequences and have observed their accuracy. AIC and BIC pick the true order in case of MC and usually pick a 2-state HMM as the best model when data is generated using a HMM (irrespective of the order used for data generation). Auto-correlation function is also studied as a way of selecting the right model. It is observed that the auto-correlation function can also give some insight into the

problem of Markov order selection. We will further investigate these issues and will study the consistency of AIC and BIC order estimation techniques.

References

I. Akbar, Markov Modeling of Third Generation Wireless Channels, M.S. Thesis, Virginia Tech, 2003.

T. W. Anderson and L. A. Goodman, "Statistical inference about Markov chains," Ann. Math. Statist., vol. 28, 1957, pp. 89-110.

P. Billingsley, "Statistical methods in Markov chains," Ann. Math. Statist., vol. 32, 1961, pp. 12-40.

Oliver Cappé, Eric Moulines & Tobias Rydén, Inference in Hidden Markov Models, Springer, 2005.

I. Csiszár & P. Shields, "The consistency of BIC Markov order estimator," Ann. Statist., vol. 28, pp. 1601-1619.

W. Feller, Introduction to Probability Theory and Its Applications, vol. 1, John Wiley & Sons, 1950.

L. Finesso, "Consistent Estimation of the Order for Markov and Hidden Markov Models", Ph.D. Dissertation, University of Maryland, 1990.

E. Gassiat & S. Boucheron, "Optimal error exponent in hidden Markov models order estimation," IEEE Trans. Inform. Theory, 49, 2003, 964-980.

R. A. Howard, Dynamic Probabilistic Systems, Volume I: Markov Models, John Wiley and Sons Inc., 1971.

R. A. Howard, Dynamic Probabilistic Systems, Volume. II: SemiMarkov and Decision Processes, John Wiley and Sons Inc., 1971.

S. Khundapur & P. Narayan, "Order Estimation of Hidden Markov Sources and Binary Renewal Processes," IEEE Trans. Inform. Theory, 48, 2002, pp. 1704-1713.

I. L. MacDonald & W. Zucchini, Hidden Markov and Other Models for Discrete-valued Time Series, Chapman & Hill, 1997.

J. McLachlan & D. Peel, *Finite Mixture Models*. New York, John Wiley & Sons Ltd., 2000.

B. L. S. P. Rao, Identifiability in Stochastic Process: Characterization of Probability Distributions, Academic Press, 1992.

S. M. Ross, Stochastic Processes, Second Edition, Wiley, 1996.

S. Sivaprakasam and K. S. Shanmugan, "An Equivalent model for burst errors in digital channels," IEEE Trans. Comm., vol. 43, April 1995, pp. 1345-1355.

W. Turin, Digital Transmission Systems: Performance Analysis and Modeling, McGraw-Hill, 1998.

Subtask 1.2e Software radio integration into the AWINN demonstrations.

Task objective: The goal of this subtask is to integrate the software radio developed in Subtask 1.2a into AWINN activities. To achieve this objective, the software radio is being designed with two distinct modes of operation: a communication mode and a data capture mode. The communication mode is currently optimized for impulse UWB signals, however, it is capable of operating using any broadband communication technique (such as DSSS or OFDM). The only limitations on the types of signals that the receiver can handle are: (1) the 2.2 GHz analog input bandwidth limitation of the MAX104 ADCs, (2) the 8 GHz effective receiver sampling frequency, and (3) the processing power of the FPGA.

In the data capture mode, the receiver will simply capture ADC samples and store them in the FPGAs RAM memory. The data can then be processed in non-real time using one of the FPGAs PowerPC processors, or the sample values can be transmitted to a host computer via the USB interface. The number of samples that can be captured is limited by the amount of high-speed RAM memory that can be allocated, but is currently estimated to be around 256,000-512,000 samples—corresponding to about 32-64 μ sec of captured data. A trigger signal input allows the receiver to estimate the time of arrival of received samples for ranging, and the ability to synchronize multiple receivers to a common clock signal allows for precise position location.

Accomplishments during reporting period: Several provisions for integrating the software radio into the AWINN activities have been included in the design of both the prototype and full receiver. To facilitate synchronization of several receivers, the clock distribution network was modified to allow for several receivers to be synchronized to a single clock source. A trigger signal input allows the receiver to operate in the data capture mode and measure the time of arrival for UWB pulses. A trigger output allows the FPGA to control an external UWB pulse generator, to facilitate evaluation of the communication system, ranging, and position location algorithms. Finally, FPGA code for the data capture mode is under development and will be implemented on the prototype receiver board.

Schedule:

- August/September 2005 – Evaluate Prototype Receiver
 - Verify the Receiver Operates in All Modes
 - Verify FPGA Code for Data Capture as well as PowerPC Processing
- October-December 2005 – Refine FPGA/PowerPC code for ranging and/or position location
 - Support Code Development with Measurements either from Lab Equipment or the Prototype Receiver
- Spring 2006 – Integrate Full Receiver into AWINN Activities
 - Crane Demonstration
 - Position Location
 - Imaging
 - Channel Measurements

Personnel:

Chris R. Anderson – Transmitter and Receiver Hardware Development

Subtask 1.2f UWB applications to technology development applicable to Sea-Basing: position location, ranging, and imaging.

Please refer to Task 4, TIP #2

1.2.3 Importance/Relevance

The simulation results from the SDR testbed simulations demonstrate that the time-interleaved sampling approach is a viable hardware architecture. The use of TI-Sampling with digital demodulation provides a tremendous amount of flexibility in the receiver operation. Even though the receiver is optimized for impulse UWB communication, it should be capable of using almost any broadband communication scheme.

The UWB SDR algorithm design is investigating ways of improving signal acquisition and tracking, as well as operation in multipath environments. Ship-based environment tend to generate a large number of multipath signals and represent a tremendous amount of energy available for the receiver to capture. Using a pilot-based matched filter topology, the receiver can capture a large percentage of the available energy without resorting to the complex tracking algorithms required by Rake receivers.

The distributed MIMO architecture investigated in this task will allow a number of UAVs to coordinate their transmissions and take advantage of space-time coding performance gains. These performance gains are available even if the various UAVs are not perfectly synchronized—an important consideration if the transmission involves a UWB signal. Combining UWB with distributed MIMO, we believe that long-range transmissions should be possible while still maintaining the LPI properties of UWB signals.

Finally, UWB signals have been demonstrated to have precision ranging and position location properties. Combining 3D ranging information with the crane control system should allow for sea-based ship-ship cargo transfer. Additionally, the position location abilities of UWB will allow for inventory control and tracking, as well as the precision maneuvering required to establish the ship-ship cargo transfer.

1.2.4 Productivity

Personnel

Chris R. Anderson, Jan. 15, 2005 – present
Jihad Ibrahim, Jan. 15, 2005 – present
Swaroop Venkatesh, Jan. 15, 2005 – present
Maruf Mohammad, Jan. 15, 2005 – present

Faculty supported

Jeffrey H. Reed, Jan. 15, 2005 – present
R. Michael Buehrer, Jan. 15, 2005 – present
William H. Tranter, Jan. 15, 2005 – present

1.3 Task 1.3 Collaborative and Secure Wireless Communications

1.3.1 Overview

The Task 1.3 research team was given the duty of deriving an approach to allow independent mobile transceivers to operate collaboratively to improve communications link dynamics for far-field exchanges. By doing so, this approach will improve communication range, improve communication quality, reduce power consumption, and/or reduce sensor weight. The proposed solution will utilize the spatial distribution of the sensor network by creating a large virtual antenna. The team will utilize beamforming techniques to accomplish this; however, the proposed approach differs from contemporary approaches in two ways. First, traditional approaches rely on having a set of antennas that have a fixed spatial relationship with each other, such as a line, circle, or other set formation. Here, the antennas are on mobile transceivers (1 per device), and their position relative to the other mobile nodes and the base station change over time. Second, traditional approaches rely on having either a single transceiver or a set of transceivers that are tightly coupled. Mobile transceivers are independent and can only coordinate spatial and temporal information with each other wirelessly. Beamforming using mobile transceivers will thus require an entirely new approach.

Organization: This task is managed by Directors of Virginia Tech Configurable Computing Lab using the following personnel:

Peter Athanas, Co-Director
Mark Jones, Co-Director
Deepak Agarwal, MSEE (graduated)
Brian Marshall, MSEE (graduated)
Todd Flemming, PhD student
Tingting Meng, PhD student
Yousef Islander, PhD student
James Webb, MSEE student
Matthew Blanton, MSEE student
Marc Somers, MSEE student
Lael Matthews, MSEE student

1.3.2 Task Activity Summary

Effort this quarter was directed towards Task 1.3a and Task 1.3b. This section summarizes the activities of these two tasks over the past quarter.

1.3.2.1 Collaborative Communications Methods

In this task, the team is investigating a method of improving the communication link performance between a (mobile) base station and a spatially distributed, and possibly mobile, sensor network. The team will exploit the collective behavior of the sensor network to solve specific communications problems collaboratively. A new technique for querying distant mobile sensor networks is being investigated. In doing so, multiple mobile stations work together to send a shared message to the querying base-station. There are important advantages to this approach:

The power requirements for a single mobile are small since the burden of transmission is shared among all nodes. Due to the nature of directed energy, the overall system has low detectability (or for security, low interference). The system is highly fault-tolerant and doesn't rely on the operation of any given node.

During the examination of three alternative designs, we developed a fourth design and carried it forward to a testbed implementation. This design has many of the same advantages (other than directed energy) as the other three alternatives but avoids the use of beamforming. It still follows the general framework in Figure 1.3-1, but does not attempt to synchronize phase and only very roughly synchronizes phase.

The difficulty with beamforming schemes is the precision to which phases at each transmitter must align at the receiver. Our new scheme employs a band-limited random signal at each transmitter. As illustrated below mathematically, two sinusoidal signals of the same frequency can cancel one another at the receiver if their phases are not synchronized, but random signals have a very high expectation of reasonable energy arriving at the receiver.

Consider $m_1 = m(t) = a \cos(2\pi ft)$, $m_2 = m(t + t_d) = a \cos(2\pi ft + 2\pi ft_d) = a \cos(2\pi ft + \varphi)$, two sinusoidal signals,

$$P_{m1} = \frac{1}{T} \int_{-T/2}^{T/2} m^2(t) dt = \frac{1}{T} \int_{-T/2}^{T/2} a^2 \cos^2(2\pi ft) dt = \frac{a^2}{T} \int_{-T/2}^{T/2} \frac{1}{2} dt + \frac{a^2}{T} \int_{-T/2}^{T/2} \frac{\cos(4\pi ft)}{2} dt = \frac{a^2}{2}$$

$$\begin{aligned} P_{m2} &= \frac{1}{T} \int_{-T/2}^{T/2} m^2(t + t_d) dt = \frac{1}{T} \int_{-T/2}^{T/2} a^2 \cos^2(2\pi ft + \varphi) dt \\ &= \frac{a^2}{T} \int_{-T/2}^{T/2} \frac{1}{2} dt + \frac{a^2}{T} \int_{-T/2}^{T/2} \frac{\cos(4\pi ft + 2\varphi)}{2} dt = \frac{a^2}{2} \end{aligned}$$

$$M(t) = m(t) + m(t + \varphi) = a \cos(2\pi ft) + a \cos(2\pi ft + \varphi) = 2a \cos\left(\frac{4\pi ft + \varphi}{2}\right) \cos\left(\frac{\varphi}{2}\right)$$

$$\begin{aligned} P_M &= \frac{1}{T} \int_{-T/2}^{T/2} M^2(t) dt = \frac{1}{T} \int_{-T/2}^{T/2} \left[2a \cos\left(\frac{4\pi ft + \varphi}{2}\right) \cos\left(\frac{\varphi}{2}\right) \right]^2 dt \\ &= \frac{4a^2}{T} \cos^2\left(\frac{\varphi}{2}\right) \int_{-T/2}^{T/2} \cos^2\left(\frac{4\pi ft + \varphi}{2}\right) dt = 4a^2 \cos^2\left(\frac{\varphi}{2}\right) \frac{1}{2} \end{aligned}$$

$$P_M / P_{m1} = (4a^2 \cos^2(\frac{\varphi}{2}) \frac{1}{2}) / \frac{a^2}{2} = 4 \cos^2(\frac{\varphi}{2}).$$

The combined power is tightly related to the delay / phase shift. When φ is equal to 0, i.e. perfect synchronization, we can obtain 4 times power gain by combining the two. But when φ is equal to π , i.e. the delay is half of the T, and the two waveforms would cancel. Because we cannot control the delay perfectly for our expected frequency (2.05 GHz), the combination gain is not guaranteed.

Consider two band-limited random signals, $N_1 = a(t)N(t)$, $N_2 = b(t)N(t + t_d)$, and combine

$$\text{them together } N_1 + N_2 = \begin{cases} a(t)N(t) & 0 \leq t < t_d \\ \{a(t) + b(t)\}N(t) & t_d \leq t < T_s \\ b(t)N(t) & T_s \leq t < T_s + t_d \end{cases}.$$

$$P_{N1} = \frac{1}{T} \int_0^T a(t)^2 N(t)^2 dt = P_1, \quad P_{N2} = \frac{1}{T} \int_0^T b(t)^2 N(t)^2 dt = P_2$$

Because the band-limited random signal waveform has similar characteristics to additive Gaussian Noise for power combination, they are linearly additive.

$$\begin{aligned}
 P_{N_1+N_2} &= \frac{1}{T} \int_0^T a(t)^2 N(t)^2 dt + \frac{1}{T} \int_0^T \{a(t) + b(t)\}^2 N^2(t) dt + \frac{1}{T} \int_0^T b(t)^2 N^2(t) dt \\
 &= \frac{1}{T} \int_0^T a(t)^2 N(t)^2 dt + \frac{1}{T} \int_0^T \{a^2(t) + 2a(t)b(t) + b^2(t)\} N^2(t) dt + \frac{1}{T} \int_0^T b(t)^2 N^2(t) dt \\
 &= \frac{1}{T} \int_0^T a(t)^2 N(t)^2 dt + \frac{1}{T} \int_0^T a^2(t) N(t) dt + \frac{1}{T} \int_0^T b(t)^2 N^2(t) dt + \frac{1}{T} \int_0^T b(t)^2 N^2(t) dt \\
 &= P_1 + P_2
 \end{aligned}$$

The combination of band-limited signal does not yield the gain of $y = x^2$, like the sinusoidal signal combination with perfect synchronization. In the non-perfect synchronization condition, it can achieve an expected linear gain of $y = x_1 + x_2 + \dots$ independent of phase synchronization.

Multiple Transmitter Single Receiver Beam Forming

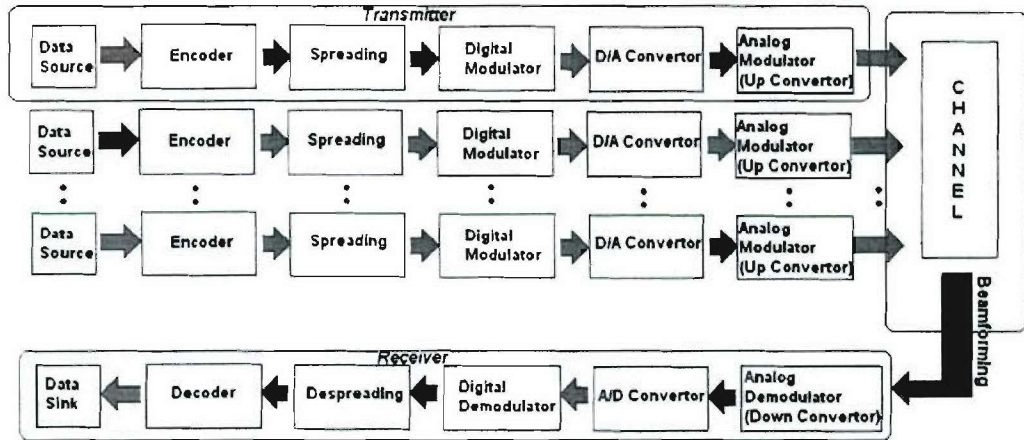


Figure 1.3-1 Conceptual MISO sensor-network query model where multiple mobile transmitters are combined at a single base station.

We developed a simulation testbed for the band-limited random signal algorithm to further investigate its performance. The following cases and figures illustrate various aspects of the performance of this algorithm as compared to BPSK in various scenarios.

Case 1: The performance of OOK with a single band-limited random signal and that of BPSK with a single sinusoidal signal is compared in Figure 1.3-2. In this figure, the blue curve crosses the red curve at 0 dB. This means in the stronger signal environment where $\text{SNR} > 0$ dB, the performance of a single band-limited random signal is better than that of a single sinusoidal signal and vice versa. The theoretical BPSK curve is also shown as a baseline.

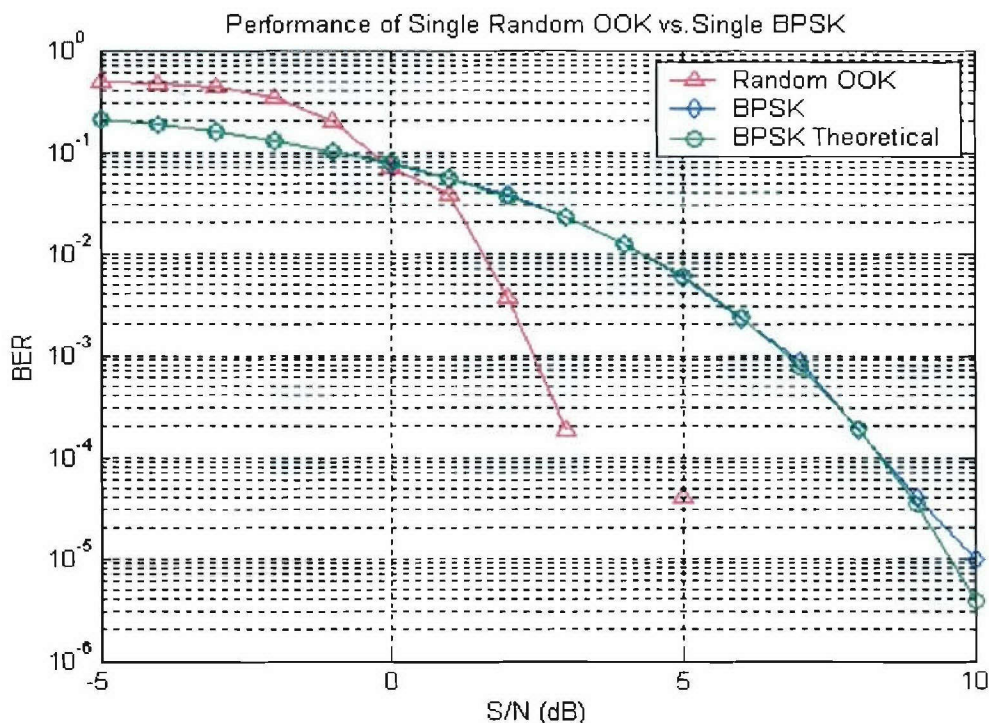


Figure 1.3-2 The performance of single signal (Case 1).

Case 2: The performance of OOK with two band-limited random signals and that of BPSK with two sinusoidal signals is compared. Here, perfect synchronization between two signals is assumed. As shown in Figure 1.3-3, the 1 dB point on the blue curve and the 7 dB point on the green curve have almost the same BER around 8×10^{-4} . It can be observed that a power gain of four times is achieved from adding a second BPSK signal. There is a 3 dB gain between the red and the pink curves. It can be concluded that a power gain of two times is achieved from adding a second random signal.

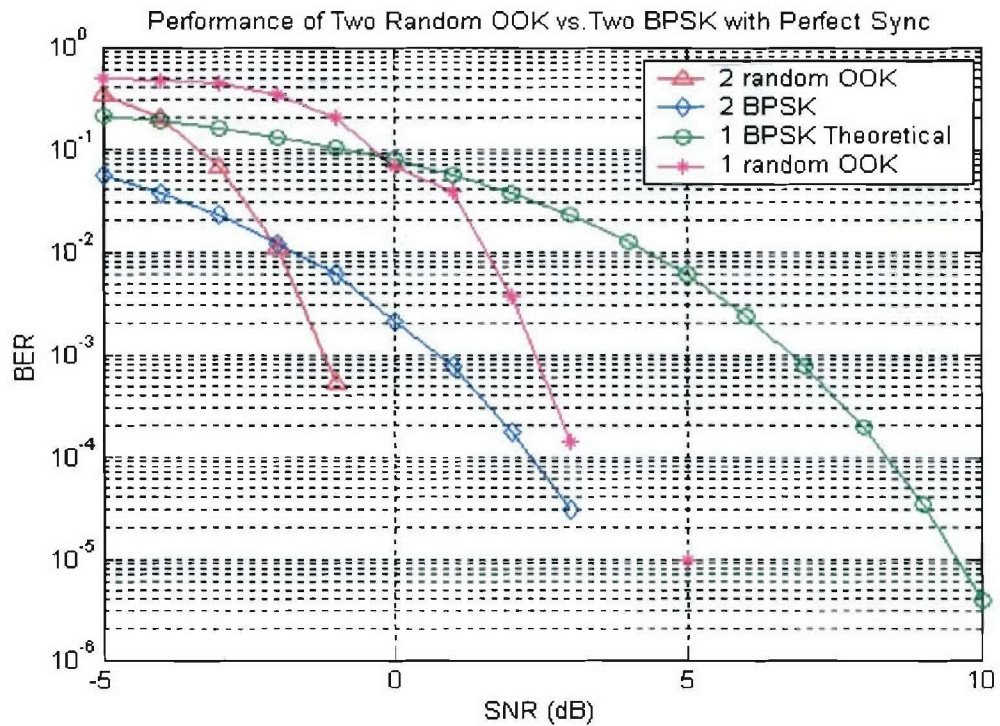


Figure 1.3-3 The performance of two combined signals with equal power with perfect synchronization (Case 2).

Case 3: The performance of OOK with two band-limited random signals and that of BPSK with two sinusoidal signals is compared. In contrast with case 2, non-perfect synchronization between two signals is assumed. It can be observed in Figure 1.3-4, that the combined BPSK has a large BER throughout the SNR range because of the random phase offset; the combined random OOK can maintain the performance from case two and has 3 dB from the single random OOK performance. It can be concluded that non-perfect synchronization does not degrade the performance of combined random OOK and synchronization will not be a necessary assumption in the later cases.

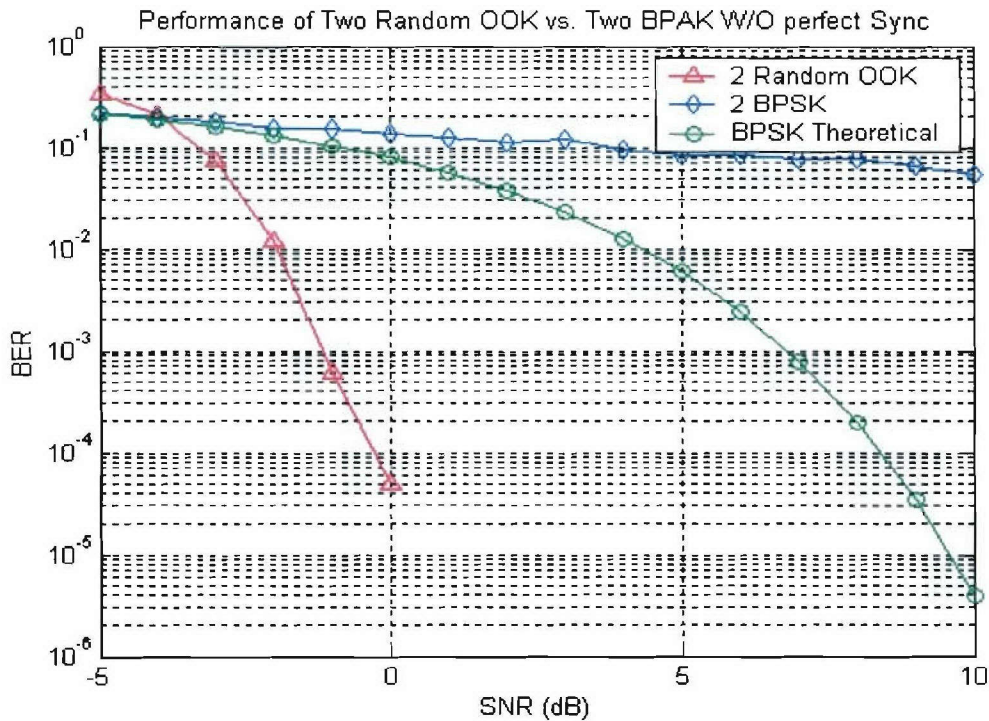


Figure 1.3-4 The performance of two combined signals with equal power W/O perfect synchronization (Case 3).

Case 4: The performances of OOK with two, three and four combined OOK band-limited random signals is compared. Equal power is assumed for each of the random signals. In Figure 1.3-5 below, the -3 dB point on red curve (2 random signals with OOK) and 0 dB point on the blue curve (4 random signals with OOK) have similar BER of 3×10^{-4} . This means that a 3 dB gain is achieved by adding twice the power, i.e. $10 \cdot \log_{10}(4/2)$. The estimated gain of two random signals can be expressed as $10 \cdot \log_{10}(3/2) = 1.76 \text{ dB}$. This matches the observation in Figure 1.3-5.

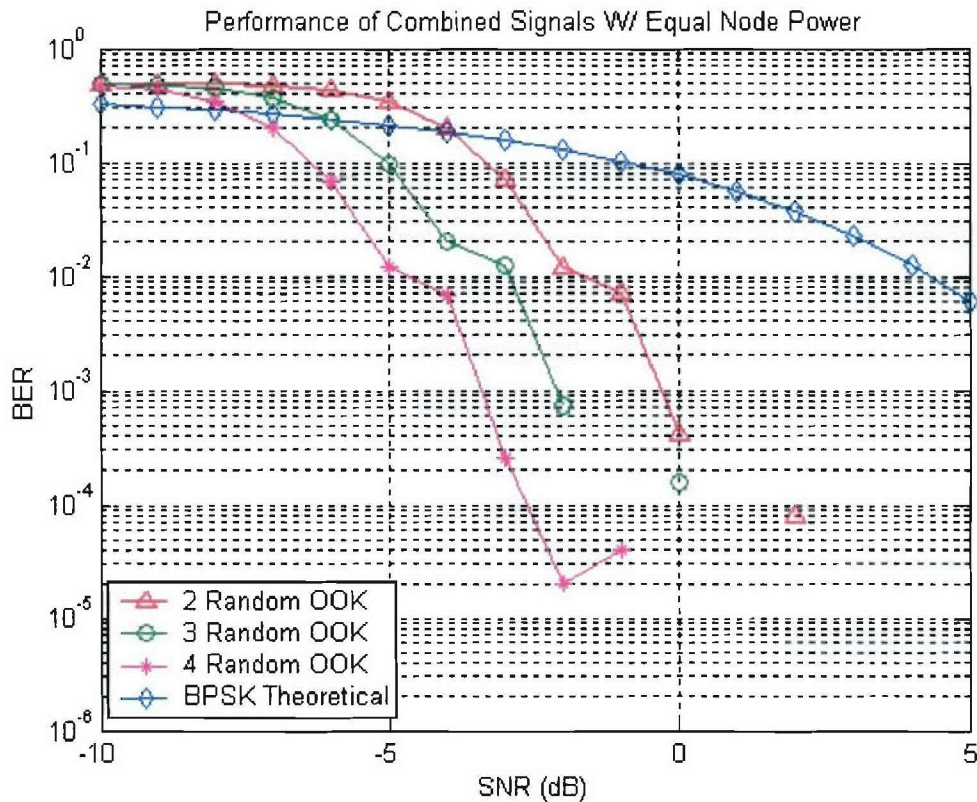


Figure 1.3-5 The performance of Two, Three and Four random signals with equal power (Case 4).

Case 5: The performance of OOK with one, two and four band-limited random signals is compared in Figure 1.3-6. In the two signal cases, each signal has one-half of the power of the single signal; in the four signal cases, each signal has one-quarter of the power of a single signal. It can be observed in this figure that the curves of these three cases are almost overlapped. It can be concluded that the same performance is achieved when the sum power of each node is the same.

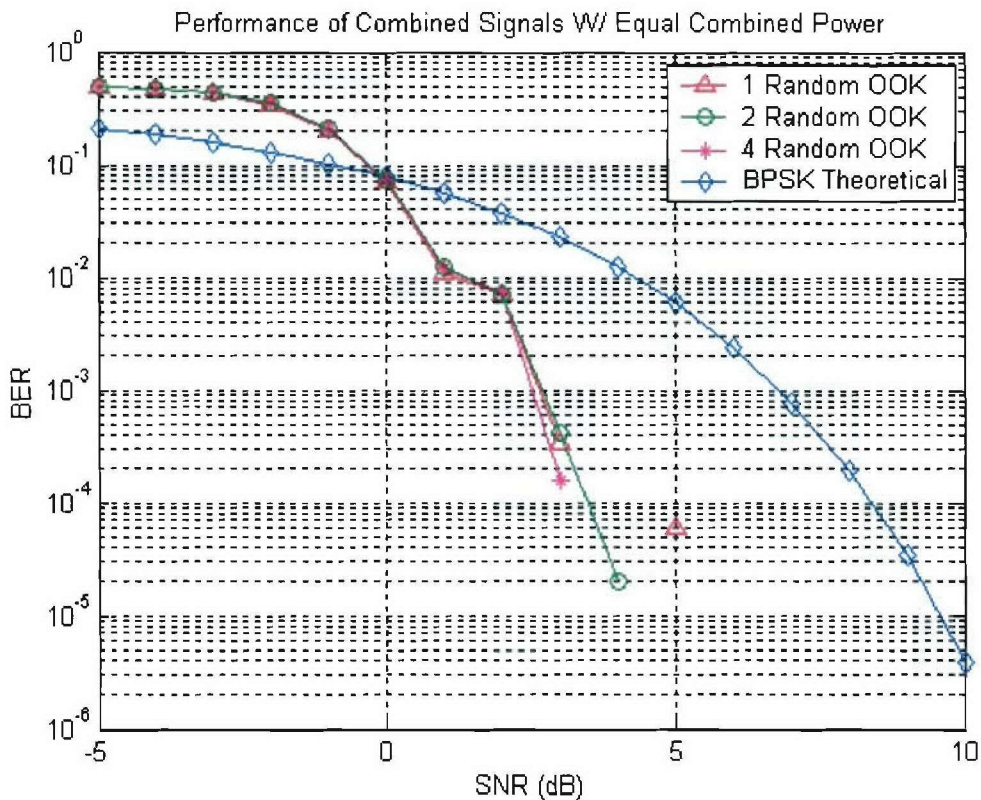


Figure 1.3-6 The performance of one, two, and four signals with equal power (Case 5).

Finally, we constructed a physical testbed to demonstrate the performance of the band-limited random signal algorithm. The team built two linked transmitters (Figures 1.3-7 & 1.3-8) and one receiver (Figure 1.3-9) to test simultaneous transmission of identical data. The transmitters use on-off keying with a band-limited pseudo-random signal as the carrier. The transmitters send the random signal when they need to send a 1 and don't send anything when they need to send a 0. Each packet contains a 31-bit m-sequence prefix, an 8-bit payload size, an 8-bit checksum, and the payload (0-255 bytes). The linked transmitters send data in phase, but the pseudo-random signal generators and the local oscillators run freely.

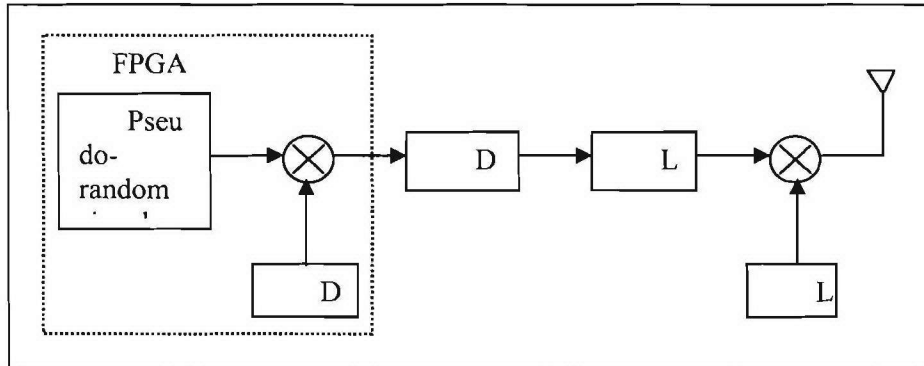


Figure 1.3-7 Basic transmitter.

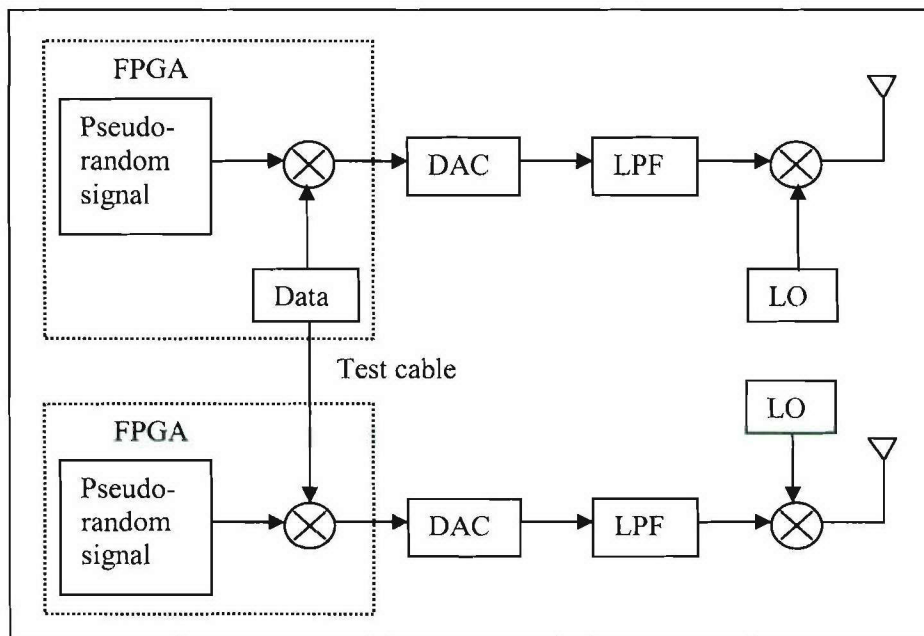


Figure 1.3-8 Linked transmitters.

The transmitters send data at 2500 bits per second using a 100 MHz DAC. The modulated signal is less than 100 MHz wide (double sideband) and is centered at 2.05 GHz. The Red River board in the receiver sends approximately 160k samples per second to the software. The Red River board limits the data rate; future receiver designs will allow the transmitters to send data at a higher rate without increasing the bandwidth.

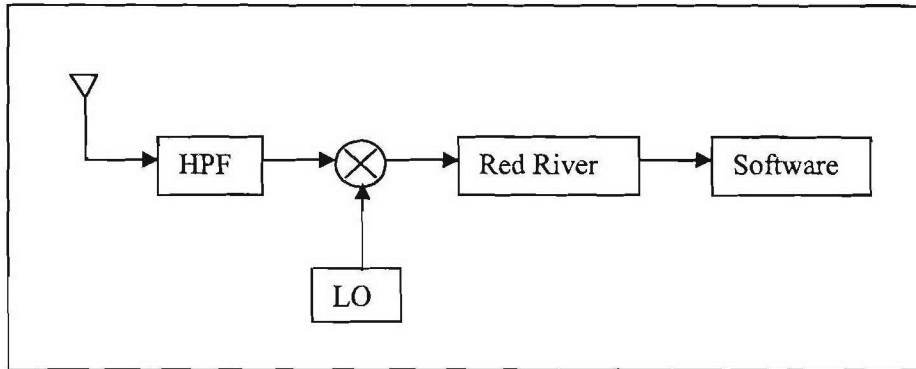


Figure 1.3-9 Receiver.

Software does most of the receiver's work. It divides incoming samples into partial bits (1/2 of a bit period, Figure 1.3-10) and assigns each partial bit a score, which is the sum of the sample magnitudes. Only one-half of the partial bits are correctly aligned with the incoming data. The partial-bit scores feed into a circular buffer that is used by the match filter to detect the beginning of a packet. The match filter looks at every other partial-bit score in the buffer. The match filter thus finds the subset of partial bits that aligns correctly with the incoming data. The match filter also determines the threshold value that separates ones from zeros. After the filter finds a match, the software feeds every other partial-bit score to a deserializer. It then computes the packet's checksum and rejects packets that have a checksum error.

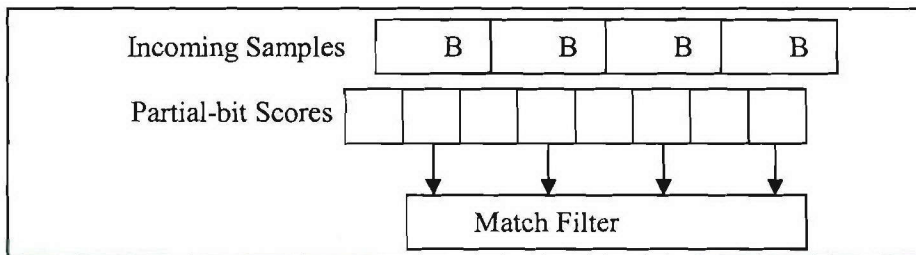


Figure 1.3-10 Receiver software operation.

Both the single-transmitter and linked-transmitter schemes were tested. The receiver properly received data under both scenarios. The received power was approximately 3 dB higher with two transmitters running than with one transmitter running; the transmitter antennas were the same distance from the receiver antenna. The signals from the two transmitters did not interfere with each other. Bit error rates were not measured.

1.3.2.2 Determining Position (for prototyping)

The purpose of this subtask is to develop a behavioral program using current robotics software to accurately estimate a robot's position to within 1.5 cm. Position is relative to an arbitrary location in a test room to which all participating robots orient themselves and operate on the same x, y plane. This task can be extended to determine the relative position from a base station by creating an offset to the relative map's origin. The same technique can also be applied to determine absolute position on the earth's surface. Position accuracy is required in the AWINN project to correctly transmit data from individual point sources (robots) to a base station. The basis behind

the project assumes that each robot does not have enough power on its own to reach the base station. However, when multiple robots send timed signals of the same wavelength and phase, the signals will combine providing a signal strong enough to reach the base station. To achieve the proper phase, the wavelength of each robot cannot be off by more than 10 percent. To ensure that the phase and timing of each robot's transmitted signal combines to form an amplified beam, the position of each robot must be determined within 1.5 cm. In the case of the band-limited random signal method, we can relax this somewhat, but it will still have a bearing on determining synchronization of timing of message sending.

The platforms for demonstrating the practicality of the AWINN project are robots running the ERSP 3.0 robotic development software. The basic software structure for their operation is a wander-and/or-explore pattern that directs each robot around its environment while avoiding obstacles and creating an internal map so it can analyze its position and make corrections to its location as the map becomes increasingly more accurate.

Most of the focus for the last quarter was on validating the accuracy of the navigation system through a variety of parameters and changing environmental conditions. The current camera in use is a simple web cam which can produce images with a resolution of 640 X 480. In fact all cameras supported by the ERSP program have this same maximum resolution. Therefore a more advanced camera would likely not offer much improvement in object recognition. An important part of the software's navigation is the ability to detect multiple landmarks. While the robot explores its environment, multiple pictures are taken with the camera. When a picture is taken which has a sufficient number of features, it is stored in a database along with the present position of the robot at that time. Features are best defined as sharp contrasts between items in the camera's field of view. Images that have distinct corners or well-defined differences in color provide multiple features with which the software can identify a landmark.

To assist the robot in creating multiple landmarks, it was necessary to provide it a landmark-rich environment. Blank white walls proved virtually useless in creating landmarks and therefore a more realistic setting was created using chairs, desks, boxes, posters, and other random "clutter" items which were distinct. The next step was refining the recognition algorithm so that it would be able to create multiple new landmarks from differing angles and positions while at the same time retaining enough distinct features to identify landmarks it had already seen. This was accomplished through a parameter known as feature-quality. Higher values resulted in a larger number of landmarks identified, but also reduced the program's ability to identify previously established landmarks. After several tests ranging from values of 0.5 to 100, a standard feature quality of 20 was established that provided enough new landmarks that were easily recognized by the program.

One additional problem in establishing suitable landmarks was the angular velocity of the robot. The speed at which the camera resource task is able to update a picture file is relatively slow (about 0.5 second), therefore any angular motion causes distortion and blurring. Reducing the maximum angular velocity provided better picture results but reduced the robot's turning ability to such an extent that it was impractical. Instead, the solution to this problem lies in the exploration pattern. When exploring its environment the robot proceeds in a straight line long enough to establish a well defined landmark. Although linear speed can produce some blurring of landmarks as well, it was generally minimized and had no noticeable effect at our desired operating speed of 10 m/s.

A working map was created by allowing the robot to explore its environment and saving the results to file. This map file was then loaded into each additional robot and provided enough

adequate landmarks to correct position to within 15cm during most operation. Two challenges which have limited the accuracy are a changing environment and the attempted correction using bad measurements. Eventually if the robot continues to explore the environment it will find enough landmarks to correct its position to within the 15 cm objective; before that time, however, measurements can be off by as much as 40-50 cm.

1.3.2.3 Embedded Multi-core RTOS for Node Management

In this task, nodes in the sensor network will need to sequence their operations carefully. Due to the nature of the multitude of computational tasks required on each node, a popular embedded real-time operating system (RTOS) is being adapted for use in our soft-core FPGA platform for the purposes of modem management.

The Xilinx MicroBlaze is a soft processor intended to be used in FPGA applications and embedded products. Its acceptance has recently grown in the embedded and research communities and several groups have contributed or created products that have increasingly aided its popularity. For instance, an Australian university ported the ucLinux real-time operating system to the MicroBlaze and this combination has become a respectable option for developers.

In the Virginia Tech Configurable Computing Laboratory, researchers have been conducting research in the field of configurable computing in our lab. One of the products of his research has been a MicroBlaze instruction-level compatible soft-processor called the *OpenFire*, which has recently been released as open source. To further this research in configurable arrays, an operating system is required. eCos is a popular open-source operating system frequently used in single application, single-process embedded products. Originally maintained by the RedHat Corporation (it is not a Linux product), it is now maintained by an independent group. eCos is an excellent choice as an operating system for the MicroBlaze platform for the following reasons: eCos is popular and well-received in the community as is the Xilinx MicroBlaze.

Many developers, institutions and companies have requested an eCos port for the MicroBlaze over the past years all over the world and one is yet to be created. The eCos system is simple - it is intended for processors that contain no memory management unit (MMU). eCos is extendible and configurable. Its popularity and power comes from its simplicity and the ability to choose exactly which components you would like included and the ability to add others. This enables it to be a workable solution for all types and sizes of applications and systems.

eCos is open-source enabling us to extend and modify it to future applications and research. The Configurable Computing Laboratory has undertaken the task of producing a port of the eCos RTOS for the Xilinx MicroBlaze/ML310 and ultimately the OpenFire processor. As of now, the team has completed an implementation of the configuration tool portion of the system and almost completely mapped the requirements needed by the operating system against the capabilities of the processor. A base for the port has been selected, that of the MBX/PowerPC platform. This was a suitable starting point because of the simplicity of its eCos implementation. This new base is almost fully registered with the supplied configuration tool.

The eCos configuration tool requires that the individual sections be written manually in a pseudo-language called CDL, the Component Description Language, which is an extension the Tcl/Tk language. The configuration tool recognizes which portions of the code can be conditionally compiled into the RTOS executable and how to present these options to the user. It also determines compilation options, such as which libraries are available in the build chain (such as math and string processing) as well as the level of the library support. The CDL portion consists

of a hierarchical structure of configuration files resident with the necessary drivers and source code.

The team is now able to successfully layout a source tree suitable for a RTOS build. This alone is a milestone that will assist us in the development process. The configuration tool is capable of creating a suite of testing applications and libraries to test the implementation as well as building a RedBoot instance for the platform. RedBoot is a specialized bootstrap environment that can assist in booting and loading applications as well as communicating with the outside world via serial port or Ethernet.

The creation of a new port requires detailed specification of the processor. These definitions, such as base and compatible data types for the 32bitMicroBlaze have been completed. In addition, a "mk_defs" (pronounced "make defs") has been defined. This technique, first used in the creation of the Mach OSF and now commonly accepted allows C-level specifications to be introduced at the assembly language level, thereby reducing the number of places such definitions have been made. The processor characterization also includes complete definition of such things as the meaning and masks of machine status registers. We have also completed the code required to do context switching (save and load context), definition of interrupts, exceptions, coding of stub eCos Vector Service Routines (VSR) and their definition to the kernel interfaces and various utility routines such as bit indexing, reorder barriers, machine status register routines such as enabling, disabling and restoring of interrupts.

The following work remains before a build of the eCos system can be completed: creation of linker scripts, definition of memory layout files that describe I/O locations, mapping of exceptions to POSIX signals, definition of ML300 platform specifications, inclusion of interrupt and clock support for thread scheduling, and mapping of eCos register definitions to the linear array used by GNU Debugger or GDB (we are unable to locate documentation for the MicroBlaze GDB, but will solicit assistance from the ucLinux listserv) and the utility functions that support these operations (known as the "stub").

Once this work is completed, we will be able to build and debug the base system. Our goal is to release the code to the general public and solicit volunteers to contribute drivers and bug elimination.

1.3.3 Importance/Relevance

Software defined radios have the potential of changing the fundamental usage model of wireless communications devices, but the capabilities of these transceivers are often limited by the speed of the underlying processors. Here we make an attempt to solve this problem by using reconfigurable architectures to develop custom data paths which can handle these high data rates using commercially available FPGAs as an alternative to custom ASICs which lead to the obvious cost and development time benefits. An added advantage of such architecture is the capability to use run-time reconfigurability to adapt to the effects of pulse shaping, channel coding, error control, and network algorithms on UWB communication. It can also be used to implement advanced cryptosystems or obfuscate communication.

1.3.4 Productivity

Conference publications

1. D. Agarwal, "An 8 GHz UWB Transceiver Prototyping Testbed," Master's Thesis, Virginia Tech, Blacksburg, VA, Oct 2005.

2. Stephen Craven, Cameron Patterson, and Peter Athanas, "A Methodology for Generating Application-Specific Heterogeneous Processor Arrays", Proceedings of the 39th Hawaii International Conference on System Sciences, HICSS 2006 / MOCHA 2006, Kauai, HI, Jan 2006.

Invited Talks

1. P. Athanas, "Secure Communications and High Performance Configurable Computing," Wright State University, Department of ECE Seminar Series, September 2005.

Students supported

Todd Flemming, PhD student
Tingting Meng, PhD student
Yousef Islander, PhD student
James Webb, MSEE student
Matthew Blanton, MSEE student
Marc Somers, MSEE student
Lael Matthews, MSEE student

2. TASK 2 Secure and Robust Networks

2.1 Task 2.1 Ad Hoc Networks

2.1.1 Overview

Task Goal: This task investigates core network capabilities for quality of service (QoS), security, and routing in ad hoc networks, especially mobile ad hoc networks (MANETs).

Organization: This task is managed by Scott Midkiff and involves or has involved the following personnel:

Scott F. Midkiff, faculty (task director)

Luiz A. DaSilva, faculty

Nathaniel J. Davis, IV, faculty (1/15/05-8/14/05)

Y. Thomas Hou, faculty

Shiwen Mao, post-doctoral research associate

George C. Hadjichristofi, GRA (1/15/05-5/14/05), post-doctoral associate (7/25/05-present)

Walter M. de Sousa, GRA (5/15/05-present)

Unghee Lee, GRA (33% for 4/1/05-5/14/05, 100% for 5/15/05-present)

Xiaojun Wang, GRA

Summary: This quarter we continued work on integration of routing and medium access control (MAC) protocols for ad hoc networks to support multiple channel operation, implementation of test bed conversion to support both Internet Protocol (IP) version 6 (IPv6) and IP version 4 (IPv4) including IP Security (IPsec) and key management. We enhanced the capabilities of TopoView, our network monitoring tool, to support both IPv6 and IPv4 operation and started the development of a topology control algorithm to increase effective network capacity. We also continued to investigate how to exploit path diversity in ad hoc networks and demonstrated it through implementation improved support for video communication. The accomplishments and other details are provided in Section 2.1.2 below.

2.1.2 Task Activities for the Period

Subtask 2.1(a): Policy-based Quality of Service

Task Objective: The objectives of this subtask are to investigate and develop quality of service mechanisms that provide differential bandwidth allocation and scheduling based on traffic type, node type, and the current network environment. We seek to increase the adaptability of the QoS mechanisms to operate more robustly in a variety of environments. We will also explore automatic adaptation at the physical and data link layers in response to application and network-layer demands, as an initial exploration of cognitive networks as an approach to cross-layer optimization.

Accomplishments during reporting period: Investigation and planning for this task continued during this quarter. We focused on the development of a topology control (TC) algorithm that increases network capacity by means of controlling the physical topology of heterogeneous ad hoc networks, composed of nodes with different capabilities (e.g., different antenna subsystems) and resources (e.g., varying energy supplies). The TC algorithm coordinates nodes' decisions regarding their transmitting ranges with the objective of reducing interference and generating a network topology with desired properties (e.g., higher effective network capacity). In addition to

the development of this algorithm, we investigated various practical implementation strategies of TC algorithms in the Linux operating system and performed an initial assessment of updating our test bed to allow for the evaluation and demonstration of TC. We also continued to investigate relevant literature in the field.

Links to other tasks: This subtask has natural synergies with Task 2.4 (Cross-Layer Optimization), as the mechanisms that support QoS in mobile ad hoc networks span the physical, data link, network, and application layers. It also integrates with Task 2.2 (Real-Time Resource Management, Communication, and Middleware) as some of the QoS mechanisms developed here will support real-time applications and must integrate with the real-time middleware developed in Task 2.2.

Schedule: The updated schedule for this subtask is as follows.

- Develop extended policy-based QoS mechanism (April-November 2005)
- Explore adaptability methods (July-December 2005)
- Demonstrate potential benefits of topology control in test bed (July-December 2005)
- Realize and integrate protocols using test bed (January-March 2006)
- Refine protocols based on performance evaluation and demonstrations (April-June 2006)

Personnel: The following personnel were assigned to this subtask during the quarter.

Luiz A. DaSilva, faculty (subtask leader)
Scott F. Midkiff, faculty
Waltemar de Sousa, GRA

Subtask 2.1(b): Security Mechanisms for Ad Hoc Environments

Task Objective: The objectives of this subtask are to investigate and, where feasible and deemed appropriate, develop security mechanisms that are efficient for ad hoc network environments. Our initial emphasis considers a distributed key management system (KMS) and associated shared trust schemes.

Accomplishments during reporting period: During the quarter, we deployed the integrated Key Management System (KMS), Openswan (which implements user space IPsec), and Linux kernel IPsec mechanisms on our test bed and tested interoperability with other network functions, including OLSR-MC as investigated in Subtask 2.1(c). The interoperation was successful for the most part, except from a particular functionality limitation introduced by an Openswan implementation “bug” that will be addressed in the next quarter. Any node in the network can establish security associations (SAs) by utilizing IPv4 addresses and/or IPv6 addresses. The KMS dynamically distributes the certificates of the nodes throughout the network by utilizing Delegated Certificates Authorities (DCAs) and trusted peers. Communication among nodes is facilitated through the OLSR-MC routing protocol. This routing and security systems’ integration was demonstrated on December 8.

Links to other tasks: This subtask has synergies with Subtask 2.1(c) and Task 2.4 (Cross-Layer Optimization) as link layer and, especially, network layer information can be employed to improve key management and other security functions. We are working to deploy a prototype for evaluation in the test bed developed in Subtask 2.1(e) and use tools of Subtask 2.1(f).

Schedule: The schedule for this subtask is as follows. There is no change from the previous quarter.

- Develop DCA and trust management system (January-June 2005)

- Integrate cross-layer design features (July-September 2005)
- Realize prototype implementation (July-December 2005)
- Integrate protocols using test bed (January-March 2006)
- Refine protocols based on performance evaluation and demonstrations (April-June 2006)

Personnel: The following personnel were assigned to this subtask during the quarter.

Scott F. Midkiff, faculty (task leader)

George C. Hadjichristofi, post-doctoral associate

Subtask 2.1(c): Ad Hoc Routing Optimization

Task Objective: The objectives of this subtask are to investigate schemes to improve routing and to use network layer functionality to improve other network services.

Accomplishments during reporting period: We continued to investigate the cross-layer design of a multi-channel system that integrates medium access control (MAC) functions and routing layer functions. We investigated the Channel Distribution Index (CDI) as a way to improve performance for channel assignment, implement a mechanism using virtual interfaces that allows control of the channel used for packet forwarding, and continued work on multi-channel version of the Open Shortest Path First with Minimum Connected Dominating Sets for Multiple Channels (OSPF-MCDS-MC or, simply, OMM) and Optimized Link State Routing for Multiple Channels (OLSR-MC) MANET routing protocols.

We implemented, integrated, and tested the Virtual Interface Module (VIM) in the routing protocols. The VIM driver is a logical network interface that implements special-purpose processing on data packets without actual physical packet transmission, while avoiding the complexity of changes to the kernel's network subsystem. This module plays a pivotal role in our prototype implementation, including channel decision, channel switching, and packet lookup functions.

We investigated the effectiveness of our multi-channel scheme. We implemented the OLSR-MC module to augment the existing Naval Research Laboratory (NRL) implementation of OLSR by adding multi-channel capabilities. To realize OLSR-MC we introduced new message formats, including the Channel Update (CU) message and delayed initial HELLO message. The OLSR-MC protocol has also been extended to work over IPv4- and IPv6-based networks and is at the final stages of testing. As mentioned in Subtask 2.1(b), this version of OLSR-MC was successfully demonstrated on December 8. In addition to the OLSR-MC routing protocol, we are currently testing the OMM routing protocol.

Links to other tasks: This subtask has direct ties to Task 2.4 (Cross-Layer Optimization) as our focus makes the network layer a key part of our cross-layer optimization schemes. In addition, we will explore synergy with Task 2.2 (Real-Time Resource Management, Communication, and Middleware). We are deploying a prototype for evaluation in the test bed developed in Subtask 2.1(e) and use tools of Subtask 2.1(f).

Schedule: The updated schedule is as follows.

- Extend DSDV to support multi-channel MAC (January-March 2005)
- Extend OSPF-MCDS to support multi-channel MAC (April-June 2005)
- Extend Optimized Link State Routing (OLSR) to support multi-channel MAC (May-June 2005)
- Realize prototype implementation in Linux, including IPv6 support (July-November 2005)

- Provide enhanced support for policy-based network management (PBNM) (November-January 2005)
- Provide enhanced support for security services (October-December 2005)
- Integrate additional cross-layer enhancements (October-December 2005)
- Integrate protocols using test bed (January-March 2006)
- Refine protocols based on performance evaluation and demonstrations (April-June 2006)

Personnel: The following personnel were assigned to this subtask during the quarter.

Scott F. Midkiff, faculty (subtask leader)

Unghee Lee, GRA

Subtask 2.1(d): Cross-Layer Approach for Routing of Multiple Description Video over Ad Hoc Networks

Task Objective: The objectives of this subtask are to investigate a theoretical foundation for cross-layer approaches for carrying video using Multiple Description (MD) coding over ad hoc networks and to build on this foundation to demonstrate key concepts via a prototype implementation.

Accomplishments during reporting period: We continued to investigate how to exploit path diversity in ad hoc networks to better support video communications. The video coding that we employ is called Multiple Description coding, a new video coding technique that is uniquely suitable for video transport over wireless ad hoc networks. We consider the problem of how to support video multicast with MD-coded video in ad hoc networks. Instead of just finding multiple paths in the network, we follow an application-centric, cross-layer routing approach with the objective of minimizing the overall video distortion. We propose an MD-coded video multicast scheme where multiple source trees are used. Furthermore, each video description is coded into multiple layers to cope with diversity in wireless link bandwidths. Based on this multicast model, we formulate cross-layer multicast routing as a combinatorial optimization problem and propose an efficient solution procedure. Our preliminary results show significant gains for a wide range of network operating conditions.

During the quarter, we continued our efforts on prototype development and test bed demonstration of video communication in ad hoc networks. We have implemented the MD algorithm for video over multipath routing, including video codec, transport control, mobile ad hoc network emulation, and live display of video and video quality based on the peak signal to noise ratios (PSNR) curves. We have chosen several interesting network settings for demonstration, purchased necessary equipment, and set up two test bed networks. In our test beds, we implemented the Ad-hoc On-demand Distance Vector (AODV) routing protocol and demonstrated that a commercial off-the-shelf video application, such as Microsoft NetMeeting, cannot provide acceptable video quality when the underlying ad hoc network is operating under dynamic situations (e.g., high packet loss). We proved that our MD algorithm provides acceptable video quality at the receiver. Furthermore, we demonstrated that cross-layer based multipath routing improves video quality more than two-disjoint path routing for MD-coded video, affirming the need for cross-layer optimization for video communications over ad hoc networks. Figure 2.1-1 shows the PSNR of the reconstructed frames delivered by the proposed algorithm and the traditional two-disjoint path routing algorithm. We used the video trace “True Lies” and an H.263+ based FEC-DD codec. We observe that the video frames delivered by the proposed algorithm have much higher PSNR values than those delivered by the traditional algorithm. A similar trend was observed on perceived video quality when the videos were played side-by-side. The successful operations of these components were demonstrated on December 8.

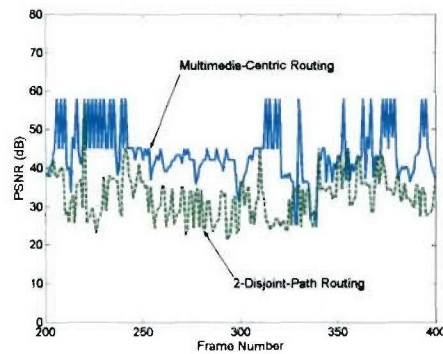


Figure 2.1-1 PSNR values of reconstructed videos.

Links to other tasks: This subtask has direct ties to Task 2.4 (Cross-Layer Optimization) as it considers cross-layer optimization schemes that involve applications, in this case, video. We are deploying a prototype for evaluation and this will be integrated into the test bed developed in Subtask 2.1(e).

Schedule: The updated schedule is as follows.

- Develop foundation for cross-layer optimization (January-July 2005)
- Develop prototype system (June-November 2005)
- Integrate prototype system into interoperability test bed (December 2005-January 2006)
- Conduct experiments with interoperability test bed (February-March 2006)
- Refine protocols based on performance evaluation and demonstrations (April-June 2006)

Personnel: The following personnel were assigned to this subtask during the quarter.

Y. Thomas Hou, faculty (subtask leader)
 Shiwen Mao, post-doctoral associate
 Xiaojun Wang, GRA

Subtask 2.1(e): Test Bed Evaluation and Demonstration

Task Objective: The objectives of this subtask are to integrate and demonstrate through research prototype implementations key ideas from Subtasks 2.1(a), 2.1(b), 2.1(c), and 2.1(d) and, as feasible and appropriate, from Task 2.2 (Real-Time Resource Management, Communication, and Middleware), Task 2.3 (Network Interoperability and Quality of Service), and Task 2.4 (Cross-Layer Optimization). The objective includes exploring interactions between different components and functions and to evaluate and demonstrate both functionality and performance.

Accomplishments during reporting period: As noted in descriptions of Subtasks 2.1(b) and 2.1(c), we continued to deploy and test components to support the evolution of the test bed from supporting only IPv4 to supporting both IPv4 and IPv6. We demonstrated the integration of IPsec, KMS, and OLSR-MC on December 8. We have, also, modified and tested the OLSR-MC configuration to support routing across logical subnets to support our test bed configuration.

Links to other tasks: The test bed evaluation and demonstrations rely on results from Subtasks 2.1(a), 2.1(b), 2.1(c), and 2.1(d), as well as Tasks 2.2, 2.3, and 2.4.

Schedule: The updated schedule for this subtask is as follows.

- Identify and clarify needs (July-September 2005)
- Acquire and deploy test bed hardware (October 2005-January 2006)
- Deploy technologies in test bed (October 2005-March 2006)
- Final performance evaluation and demonstrations (April-June 2006)

Personnel: The following personnel were assigned to this subtask during the quarter.

Scott F. Midkiff, faculty (subtask leader)

George C. Hadjichristofi, post-doctoral associate

Unghie Lee, GRA

Subtask 2.1(f): Configuration and Monitoring Tools

Task Objective: The objectives of this subtask are to investigate and develop software configuration and monitoring tools to facilitate network testing and demonstration.

Accomplishments during reporting period: We identified issues with our topology and node state monitor, TopoView, running in a combined IPv4 and IPv6 environment. Issues related to use of the Simple Network Management Protocol (SNMP) with IPv6. The SNMP functionality that handles the routing table information of the IPv6 Management Information Base (MIB) has not yet been implemented in Linux, indicating the lack of maturity of this technology. The code to provide this functionality would have to be, instead, written by us from “scratch” and would not provide any research benefits. Therefore, we elected to enhance TopoView to translate the IPv4 information acquired by SNMP using the reverse algorithm of OLSR-MC of Subtask 2.1(c). We intend to continue the investigation of network monitoring, but with non-SNMP based tools.

We have also augmented the functionality of TopoView to display the channel index information of the nodes that utilize OLSR-MC and to display the type of SAs established (IPv6 versus IPv4). Figure 2.1-2 depicts a screen capture of latest version of TopoView.

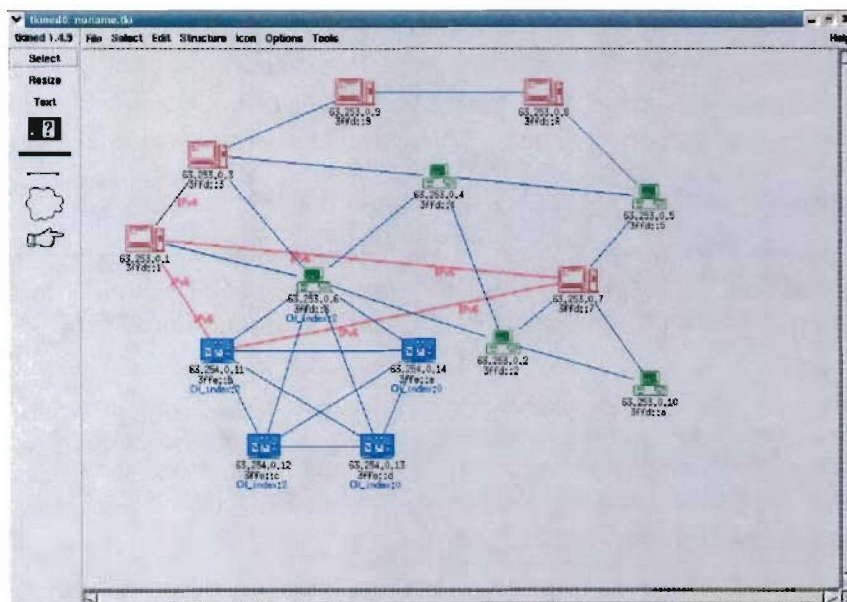


Figure 2.2-2 TopoView with IPv6 addressing, channel index, and IPv4/IPv6 SAs.

Links to other tasks: The tools support the test bed described above for Subtask 2.1(e).

Schedule: The updated schedule for this subtask is as follows.

- Identify and clarify needs (April-September 2005)
- Implement and test tools (October 2005-January 2006)
- Utilization and refinement of tools (February-June 2006)

Personnel: The following personnel were assigned to this subtask during the quarter.

Scott F. Midkiff, faculty (subtask leader)

George C. Hadjichristofi, post-doctoral associate

2.1.3 Importance/Relevance

Ad hoc networks are of particular importance to the Navy and other Department of Defense (DoD) units because of their ability to be quickly configured and operate without infrastructure. Research in ad hoc networks to date has been dominated by solutions to particular, specific problems and not to general system and network infrastructure issues. This task focuses on making ad hoc network operate successfully as a system with efficient routing, the ability to offer quality of service, and the robustness and security required of military networks. We also examine the challenging problem of delivering video, specifically Multiple Description video, in an ad hoc network.

2.1.4 Productivity

Journal publications (accepted during the quarter)

1. Y. T. Hou, Y. Shi, J. Pan, A. Efrat, and S. F. Midkiff, "Maximizing lifetime of wireless sensor networks through optimal single-session flow routing," *IEEE Transactions on Mobile Computing*.
2. S. Mao, Y.T. Hou, X. Cheng, H.D. Sherali, S.F. Midkiff, and Y.-Q. Zhang, "Multi-path routing for multiple description video over wireless ad hoc networks," *IEEE Transactions on Multimedia*.
3. Y. Shi, Y. T. Hou, H. D. Sherali, S. F. Midkiff, "Cross-layer optimization for routing data traffic in UWB-based sensor networks," *IEEE Journal on Selected Areas in Communications*.

Conference publications (appeared during the quarter)

1. M. X. Gong, S. F. Midkiff, and S. Mao, "A Combined Proactive Routing and Multi-Channel MAC Protocol for Wireless Ad Hoc Networks" (invited paper), *Proc. International Conference on Broadband Networks (BROADNETS)*, Boston, MA, October 3-7, 2005, pp. 479-488.
2. R. W. Thomas, L. A. DaSilva, and A. B. MacKenzie, "Cognitive Networks," *Proc. First IEEE International Symposium on New Frontiers in Dynamic Spectrum Access Networks (DySPAN)*, Nov. 2005, Baltimore, MD.

Conference publications (accepted during the quarter)

1. S. Kompella, S. Mao, and Y.T. Hou, "Optimal rate control for video transport over multi-hop wireless networks," *Proc. IEEE Wireless Communication and Networking Conference (WCNC 2006)*, April 2006.

2. U. Lee and S. F. Midkiff, "Channel Distribution Fairness in Multi-Channel Wireless Ad-hoc Networks Using a Channel Distribution Index," *Proc. IEEE International Performance Computing and Communications Conference (IPCCC 2006)*, April 2006, Phoenix, AZ.
3. U. Lee and S. F. Midkiff, "OLSR-MC: A Routing Protocol for Multi-Channel Wireless Ad-Hoc Networks," *Proc. IEEE Wireless Communication and Networking Conference (WCNC 2006)*, April 2006.
4. U. Lee, S. F. Midkiff, and T. Lin, "OSPF-MCDS-MC: A routing protocol for multi-channel wireless ad-hoc networks," *Proc. IEEE Communications and Networking Conference (CCNC)*, Jan. 2006, Las Vegas, NV.

Presentations

1. AWINN poster presentation at the Virginia Tech Advanced Research Institute's Open House (a research showcase event), Arlington, VA, December 7, 2005.

Meetings Attended

1. Dr. Hou and Dr. Midkiff attended IEEE BROADNETS 2005 held on Oct. 3-7 at Boston, MA. Dr. Hou served as the General Vice Chair.
2. Dr. Mao attended the NSF NOSS Informational Meeting held on Oct. 18 at Harvard University, Boston, MA.

Students supported

Waltemar de Sousa 10/1/05-12/31/05
 Unghee Lee, 10/1/05-12/31/05
 Xiaojun Wang, 10/1/05-12/31/05

Faculty supported

Scott F. Midkiff, 10/1/05-12/31/05
 Luiz A. DaSilva, 10/1/05-12/31/05
 Y. Thomas Hou, 10/1/05-12/31/05
 George C. Hadjichristofi, 10/1/05-12/31/05 (post-doctoral associate)
 Shiwen Mao, 10/1/05-12/31/05 (post-doctoral associate)

2.2 Task 2.2 Real-Time Resource Management, Communications, and Middleware

This report discusses the progress of Task 2.2 during the fourth quarter – October through December, 2005. The report has four sections: (1) task overview, (2) task activities for the period, (3) importance to the Navy, and (4) productivity. These are discussed in the subsections that follow:

2.2.1 Task Overview

The objectives of Task 2.2 include:

- (1) Develop time/utility function (TUF)/utility accrual (UA) scheduling algorithms for scheduling Real-Time CORBA 1.2's distributable threads with *assured timeliness properties* under failures. Develop distributable thread maintenance and recovery (TMAR) protocols that are integrated with such scheduling algorithms;
- (2) Develop TUF/UA *non-blocking synchronization mechanisms* for synchronizing distributable threads and single-processor threads for concurrently and mutually exclusively accessing shared objects;
- (3) Investigate how TUF/UA scheduling algorithms, synchronization mechanisms, and TMAR protocols can co-reside with policy-based network QoS management schemes, and jointly optimize (with network QoS schemes) UA timeliness optimality criteria, as envisaged in Task 2.3; and
- (4) Develop the *Distributed Real-Time Specification for Java* (DRTSJ) standard under the auspices of Sun's Java Community Process (JCP)¹, incorporating scheduling algorithms, synchronization mechanisms, and TMAR protocols developed in (1) and (2).

Embedded real-time systems that are emerging such as control systems in the defense domain (e.g., Navy's DD(X), Air Force's AWACS) are fundamentally distinguished by the fact that they operate in environments with dynamically uncertain properties. These uncertainties include transient and sustained resource overloads due to context-dependent activity execution times and arbitrary activity arrival patterns. For example, many DoD combat systems include radar-based tracking subsystems that associate sensor reports to airborne object tracks. When a significantly large number of sensor reports arrives, it exceeds the system processing capacity, causing overloads, resulting in important tracks to go undetected.

When resource overloads occur, meeting deadlines of all application activities is impossible because the demand exceeds the supply. The urgency of an activity is typically orthogonal to the relative importance of the activity—e.g., the most urgent activity can be the least important, and vice versa; the most urgent can be the most important, and vice versa. Hence, when overloads occur, completing the most important activities irrespective of activity urgency is often desirable. Thus, a clear distinction has to be made between the urgency and the importance of activities during overloads. (During under-loads, such a distinction need not be made, because deadline-based scheduling algorithms such as EDF are optimal for those situations [hor74]—i.e., they can satisfy all deadlines.)

Deadlines by themselves cannot express both urgency and importance. Thus, we consider the abstraction of time/utility functions (or TUFs) [Jlt85] that express the utility of completing an application activity as a function of that activity's completion time. Utility is typically mapped to

¹ The DRTSJ effort is currently ongoing under a JCP called JSR-50. The core members of the DRTSJ team include those from The MITRE Corporation and Virginia Tech.

application-level quality of service (QoS) metrics such as track quality and track importance in a command and control application. We specify deadline as a binary-valued, downward “step” shaped TUF; Figure 2.2-1(a) shows examples. Note that a TUF decouples importance and urgency—i.e., urgency is measured as a deadline on the X-axis, and importance is denoted by utility on the Y-axis.

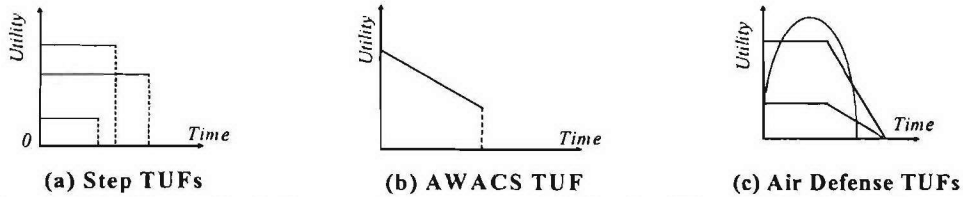


Figure 2.2-1 Example timing requirements specified using Time/Utility Functions.

Many embedded real-time systems also have activities that are subject to *non-deadline* time constraints, such as those where the utility attained for activity completion *varies* (e.g., decreases, increases) with completion time. This is in contrast to deadlines, where a positive utility is accrued for completing the activity anytime before the deadline, after which zero, or infinitively negative utility is accrued. Figures 2.2-1(b) and 2.2-1(c) show example such time constraints from two real applications (see [cjk+99] and the references therein).

When activity time constraints are specified using TUFs, which subsume deadlines, the scheduling criteria is based on accrued utility, such as maximizing sum of the activities' attained utilities. We call such criteria, *utility accrual* (or UA) criteria, and scheduling algorithms that optimize them, as UA scheduling algorithms.

UA algorithms that maximize summed utility under downward step TUFs (or deadlines) [loc86, cla90, wrjb04] default to EDF during under-loads, since EDF can satisfy all deadlines during those situations. Consequently, they obtain the maximum total utility during under-loads. When overloads occur, they favor activities that are more important (since more utility can be attained from them), irrespective of their urgency. Thus, UA algorithms' timeliness behavior subsumes the optimal timeliness behavior of deadline scheduling.

The major Task 2.2 accomplishments of this quarter include:

- Development of an Naval Air Defense demonstration application
- Implementation of the Thread-Polling algorithm for distributed thread integrity
- Implementation of Wait-Free buffering in the Naval AD application
- Integration of thread integrity mechanisms with the Tempus middleware and AD application
- Work-in-progress paper describing and analyzing an improved thread-polling algorithm

Our focus on timely thread integrity algorithms has revealed new problems in the area of scheduling cleanup operations for failed threads. We have now characterized the timeliness of the thread integrity operations in terms of two major classes of operation, 1) Administrative Thread Maintenance and Repair (TMAR) activities, including fault detection, network communication, etc. and 2) Application-Defined clean-up activities. With item (1) well in hand, our focus in the next quarter will be on the unique scheduling problem presented in (2), which will allow us to offer end-to-end timing analyses. We summarize this result in Section 2.2.2.

2.2.2 Task Activities for the Period:

Implementation of a distributed Naval Air Defense application.

In order to motivate the need for, and effect of, distributed thread integrity algorithms, an enhanced version of our Air Defense application was implemented. This application consists first of a separate scenario generation and visualization capability. The positions and behaviors of friendly and enemy vehicles are simulated and distributed by a multicast protocol to be used by application code. A graphical user interface was developed allowing a user to see the scenario progress, instrument various application and system-level metrics, and change the operational modes of the application code.

Second, a distributed application was developed, with components to model sensor and air defense cannon control systems, a tracking service, and a command-and-control (C2) capability. The application activities were then modeled using distributed threads.

Implementation of Wait-Free buffering.

The “tracking service” described above represents a high throughput service with heavy contention between “read” and “update” tasks. The wait-free buffering algorithms designed by Cho were implemented in an application context here for the first time, enabling predictable access times and predictable memory consumption.

Implementation of the thread-polling algorithm.

The thread-polling algorithm for distributed thread integrity consists of an administrative-layer lease-based mechanism for tracking the health of thread segments (termed Thread Maintenance and Repair, or TMAR), and an application-layer API enabling programmers to associate stacks of cleanup activities with each local thread segment. These capabilities were implemented in the Tempus middleware.

Integration of TMAR with the AD application.

In the case of the Naval Air Defense demonstration, the thread integrity protocol allows the application to quickly discover and respond to failed control services. From time to time, a cannon control service will fail, modeling an enemy strike, hardware/software fault, or communications failure. When such a condition is detected, the Thread-Polling protocol acts to schedule activities on the remaining nodes to return services to a safe and consistent state. Once this is complete, control is returned to the distributed thread so that it may resume operations.

End-to-end Analysis of Thread-Polling.

Work continues on gradual improvements and modifications to the thread-polling protocol so that end-to-end analytical properties may be guaranteed. Bounds have been derived for most of the activities of the protocol with the exception of scheduling cleanup activities.

Initial Integrated Demo Application.

The AD application presented above represents the first build of a distributed demo appropriate for integration with Task 2.1. With the current Thread-Polling implementation, the application is tolerant to certain classes of communication failures, which will allow it to execute successfully in a MANET environment. The complexities of MANET routing, however, present new challenges and new sources of information that the middleware and application may exploit.

References

- [cla90] R. K. Clark, "Scheduling Dependent Real-Time Activities," PhD thesis, CMU CS Dept., 1990
- [cjk+99] R. K. Clark, E. D. Jensen, et al., "An adaptive, distributed airborne tracking system," In *IEEE WPDRTS*, pages 353--362, April 1999
- [hor74] W. Horn, "Some Simple Scheduling Algorithms," *Naval Research Logistics Quarterly*, 21:177--185, 1974.
- [jlt85] E. D. Jensen, C. D. Locke, and H. Tokuda, "A time-driven scheduling model for real-time systems," In *IEEE RTSS*, pages 112--122, December 1985
- [loc86] C. D. Locke, "Best-Effort Decision Making for Real-Time Scheduling," PhD thesis, Carnegie Mellon University, 1986
- [wrjb04] H. Wu, B. Ravindran, E. D. Jensen, and U. Balli, "Utility Accrual Scheduling Under Arbitrary Time/Utility Functions and Multiunit Resource Constraints," *IEEE Real-Time Computing Systems and Applications*, April 2004
- [srl90] L. Sha, R. Rajkumar, and J. P. Lehoczky, "Priority inheritance protocols: An approach to real-time synchronization," *IEEE Trans. Computers*, 39(9):1175--1185, 1990
- [kr93] H. Kopetz and J. Reisinger, "The non-blocking write protocol NBW", *IEEE RTSS*, 131--137, 1993
- [cb97] J. Chen and A. Burns, "A fully asynchronous reader/writer mechanism for multiprocessor real-time systems," *Technical Report YCS-288*, CS Dept., University of York, May 1997.
- [hps02] H. Huang, P. Pillai, and K. G. Shin, "Improving wait-free algorithms for interprocess communication in embedded real-time systems," *USENIX Annual Technical Conference*, pages 303--316, 2002
- [arj97] J. H. Anderson, S. Ramamurthy, and K. Jeffay, "Real-time computing with lock-free shared objects," *ACM TOCS*, 15(2):134--165, 1997
- [crj05] H. Cho, B. Ravindran, and E. D. Jensen, "A space-optimal, wait-free real-time synchronization protocol," *IEEE ECRTS*, 2005.

2.2.3 Importance to the Navy

We believe that the TUF/UA real-time technology developed in this task is directly relevant to DoD's network-centric warfare concept, Navy combatant systems including DD(x), and other DoD systems such as Air Force's next generation command and control aircrafts. In fact, the fundamental aspects of this class of real-time problems include:

- (1) Need for transparent programming and scheduling abstractions for distributed computation workflows that are subject to time constraints
- (2) Systems that are subject to significant run-time uncertainties that are often manifested in execution and communication times, and event and failure occurrences that are non-deterministically distributed
- (3) Systems that are subject to transient and permanent overloads
- (4) Need for time-critical and mission-oriented resource management (i.e., timely management of resources in the best interest of the current application mission)
- (5) Need for industry/commercial standards- and COTS-based solutions for portability, robustness, and maintainability.

All these aspects are directly addressed by Task 2.2 research. In particular, Real-Time CORBA 1.2's and DRTSJ's distributable threads abstraction provides a transparent programming and scheduling abstraction for distributed real-time computation workflows. Further, the class of TUF/UA scheduling algorithms, TMAR protocols, synchronization mechanisms, and policy-

based network QoS management schemes target application activities, whose execution/communication latencies and event/failure occurrences are non-deterministically distributed and are subject to overloads. TUF/UA algorithms provide time-critical and mission-oriented resource management by (system-wide) scheduling to maximize system-wide accrued utility, where utility is mapped to application-level QoS. Consequently, utility maximization leads to managing system resources to maximize utility achieved for the users by the system. Furthermore, Task 2.2's work on the DRTSJ industry standard directly promotes industry/commercial standards and COTS-based solutions.

Thus, we believe that Task 2.2 research is directly relevant to Navy systems and other DoD systems.

DD(X) is currently using RTSJ, and is building a distributed real-time infrastructure using RTSJ. The DD(X) team has expressed significant interest in using DRTSJ – in particular, the distributable threads abstraction and end-to-end timing analysis capability. We believe that DD(X) can directly leverage DRTSJ's advanced adaptive time-critical (TUF/UA) resource management techniques, and DRTSJ's synergy with RTSJ.

2.2.4 Productivity

Journal publications

- (1) H. Wu, U. Balli, B. Ravindran, J. Anderson, and E. D. Jensen, "Utility Accrual Real-Time Scheduling Under Variable Cost Functions," *IEEE Transactions on Computers*, Submitted November 2005
- (2) H. Wu, B. Ravindran, E. D. Jensen, "Utility Accrual, Real-Time Scheduling Under the Unimodal Arbitrary Arrival Model with Energy Bounds," *ACM Transactions on Embedded Computing Systems*, Submitted November 2005

Conference publications

- (1) P. Li, B. Ravindran, and E. D. Jensen, "Utility Accrual Real-Time Resource Access Protocols with Assured Individual Activity Timeliness Behavior," *International Conference on Real-Time and Network Systems (RTNS)*, Submitted November 2005
- (2) H. Cho, C. Na, B. Ravindran, and E. D. Jensen, "On Scheduling Garbage Collector in Dynamic Real-Time Systems With Statistical Timeliness Assurances," *IEEE International Symposium on Object and component-oriented Real-time distributed Computing (ISORC)*, Submitted November 2005
- (3) H. Wu, B. Ravindran, and E. D. Jensen, "Utility Accrual, Real-Time Scheduling with Energy Bounds," *2006 ACM Symposium On Applied Computing (SAC), Track on Embedded Systems*, Dijon, France, April 23-27, 2006, Accepted October 2005, to appear
- (4) H. Cho, B. Ravindran, and E. D. Jensen, "On Utility Accrual Processor Scheduling with Wait-Free Synchronization for Embedded Real-Time Software," *2006 ACM Symposium On Applied Computing (SAC), Track on Embedded Systems*, Dijon, France, April 23-27, 2006, Accepted October 2005, to appear

- (5) H. Cho, B. Ravindran, and E. D. Jensen, “Lock-Free Synchronization for Dynamic Embedded Real-Time Systems,” *2006 ACM Design, Automation, and Test in Europe (DATE), Real-Time Systems Track*, Munich, Germany, March 6-10, 2006, Accepted November 2005, To appear

Students supported

Jonathan Anderson, January 2005 – present
Hyeonjoong Cho, January 2005 – present
Edward Curley, May 2005 – present
Chewoo Na, September 2005 – present

2.3 Task 2.3 Network Interoperability and Quality of Service

2.3.1 Overview

Task Goal: The goal of Task 2.3 is to integrate network services (as investigated in Task 2.1) with real-time middleware (as investigated in Task 2.2). Specifically, we will investigate and develop methods and mechanisms to integrate policy-based quality of service (QoS) capabilities at the network level, and perhaps at the link layer, with real-time services offered by middleware.

Organization: This task is managed by Scott Midkiff and involves the following personnel:

Scott F. Midkiff, faculty (task director)
Luiz A. DaSilva, faculty
Binoy Ravindran, faculty
George C. Hadjichristofi, post-doctoral research associate
Jonathan Anderson, graduate research assistant

Summary: Task 2.3 integrates results from Tasks 2.1 and 2.2. As these tasks are just beginning, no significant activity specifically in support of Task 2.3 took place during the reporting period beyond continuation of integration planning. The following sections summarize subtasks and schedule.

2.3.2 Task Activities for the Period

Task Objective: As stated in Section 2.3.1, the goal of Task 2.3 is to integrate network services (from Task 2.1) with real-time middleware (from Task 2.2).

Accomplishments during reporting period: Minimal activities pertaining to this subtask took place during the reporting period. For this integration, we will be reproducing the basic network environment of Task 2.1 and utilizing it for testing the components of Task 2.2. The results from this initial integration will indicate required integration adjustments for the various network functions, as well as the readiness for a complete integration between the two tasks.

Links to other tasks: This task integrates results from Task 2.1 and Task 2.2. It is also potentially synergistic with Task 2.4 (Cross-Layer Optimization) as it may be possible to integrate optimizations at the link and network layer with requirements presented by the real-time middleware.

Schedule: The revised schedule for this task is as follows.

- Plan integration approach (April-November 2005)
- Begin integration based on preliminary results (December 2005-January 2006)
- Integrate cross-layer design features (January-February 2006)
- Integrate protocols using test bed (March-April 2006)
- Refine protocols based on performance evaluation and demonstrations (May-June 2006)

Personnel: The following personnel participated in this subtask during the reporting period.

Scott F. Midkiff, faculty (task leader)
Binoy Ravindran, faculty
George C. Hadjichristofi, post-doctoral research associate
Jonathan Anderson, graduate research assistant

2.3.3 Importance/Relevance

Many military systems rely on real-time operation, but can often be characterized using “soft” real-time constraints. This work paves the way to providing real-time capabilities, based on time-utility functions (TUFs), in an ad hoc network environment.

2.3.4 Productivity

Students supported

Jonathan Anderson

Faculty supported

Scott F. Midkiff

Binoy Ravindran

George C. Hadjichristofi (post-doctoral associate)

2.4 Task 2.4 Cross-Layer Optimization

2.4.1 Overview

Task Goal: The goal of this task is to investigate and develop methods and metrics to characterize and evaluate the interaction between physical, data link, network and application layer protocols. This will be accomplished through two specific applications (a) position location networks and (b) collaborative radio networks.

Organization: This task is managed by Dr. R. Michael Buehrer and Dr. Scott Midkiff.

Dr. R. Michael Buehrer, faculty

Dr. Scott Midkiff, faculty

Dr. Tom Hou, faculty

Qiao Chen, GRA

Swaroop Venkatesh, GRA

Summary: In this quarter we focused on two subtasks: (a) Cross-layer design for UWB position-location networks and (b) collaborative radio networks. The latter sub-task was broken down into two studies, the study of collaborative UWB networks and collaborative beam-forming techniques.

2.4.2 Task Activities for the Period

2.4.2.1 Subtask 2.4.1a Cross-Layer Design for Ultra-Wideband Position-Location Networks

Overview

In this section, we build on known bounds on localization to provide new insights that can be used in position-location network design from a localization perspective. Specifically, we look at the Cramer-Rao lower bound (CRLB) for the estimation of a node's location given unbiased Gaussian range estimates from a set of location-aware "anchor" nodes. A novel characterization of the accuracy of node location-estimates is derived, which provides new insights into the design of medium-access control (MAC) protocols from the perspective of node localization accuracy. These insights are validated through the investigation of the performance of a spread-spectrum multiple access scheme in a synchronous ultra-wideband position-location network.

MAC Design for Synchronous UWB Networks

It was demonstrated previously that, for the Minimum Variance Unbiased Estimator (MVUE) of a node's location given unbiased Gaussian range information, the number of available range estimates strongly affects the accuracy of the node's location estimate. It was shown that, except when all anchors were collinear, increasing the number of range estimates results in reduction of the localization error. Even when connectivity with anchors is limited, repeated range measurements allow averaging of range estimates, which reduces their variance and, hence, the localization error.

From the perspective of MAC design, it stands to reason that a protocol that allows each unlocalized node to accumulate a large number of range estimates in a given duration increases the likelihood that an accurate estimate of the node's location is computed at the end of that duration. Based on this reasoning, as time progresses, a MAC protocol which provides a higher *effective throughput* of range estimates to unlocalized nodes should allow faster convergence of network location estimates to the true locations.

In order to verify this conjecture, we investigate the performance of a spread-spectrum multiple access scheme for UWB position-location networks. The scheme is based on the assignment of Time-Hopping (TH) codes that are commonly proposed for UWB communication [Win1998]. The motivation for investigating a scheme based on TH spread-spectrum for UWB networks is as following: (1) A spread-spectrum multiple access scheme is a “multi-channel” approach that allows simultaneous transmissions at the cost of incurring multi-access interference. This leads to graceful degradation in performance as the number of nodes is increased. (2) Due to the significant amount of spreading (transmission-bandwidth to data-rate ratio) inherent in the use of UWB signals for low data-rate applications, “single-channel” collision-avoidance approaches appear wasteful. (3) The low power spectral density of UWB signals makes sensing the channel for collision-avoidance schemes inherently unreliable. Through the following analysis, we demonstrate that for the modeled UWB position-location network, minimizing the localization error of nodes at any instant of time is equivalent to maximizing the average throughput of the network. We also utilize results from our previous work to derive bounds on the average rate of convergence of node location estimates to the true locations. This temporal characterization of localization accuracy is particularly useful in mobile scenarios.

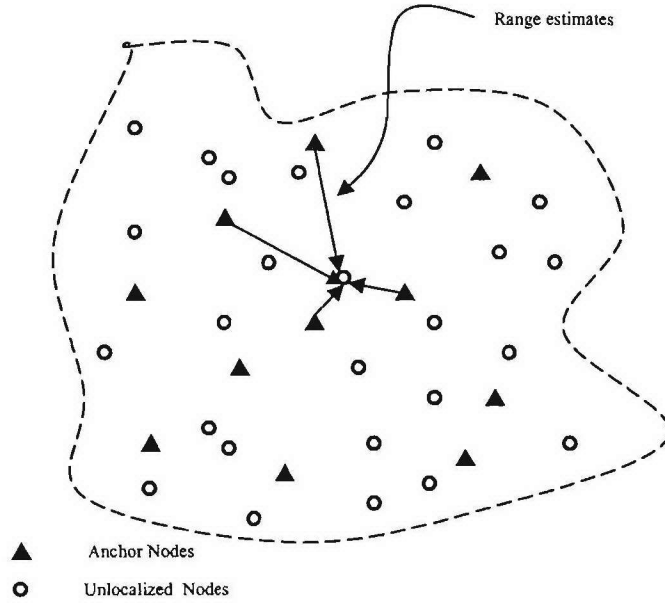


Figure 2.4-1 Network schematic: A network comprising anchor and unlocalized nodes; the anchors transmit packets to the unlocalized nodes. The unlocalized nodes can obtain range estimates using the TOAs of the packets.

Network Model

A position-location network comprising unlocalized nodes and localized anchors (note that the localized anchors may have been originally unlocalized, but now have known positions) is illustrated in Figure 2.4-1. The following assumptions are made in the modeling of the network:

1. *Spatial Distribution of Anchors:* We assume that the anchor nodes are Poisson distributed over the two-dimensional plane, with an average spatial density Λ . The probability of finding k nodes in a region with an area A is given by

$$P \{k \text{ nodes in an area } A\} = e^{-\Lambda A} \frac{(\Lambda A)^k}{k!}, \quad (2.4-1)$$

where Λ is the average number of anchor nodes per unit area. The anchors are assumed to be stationary.

2. *Packet Transmissions by Anchors:* For ease of analysis, we assume that the time-axis is slotted and that all nodes are synchronized to the slot transitions. Each anchor transmits a single packet at the beginning of a slot with probability p . The slot width T_s is assumed to be greater than the packet duration T_p . The anchor nodes are the “packet-sources” and the unlocalized nodes are the “packet-sinks” of the network. For simplicity, we assume that each packet transmitted by an anchor is intended for a unique unlocalized node. This packet is transmitted on a unique TH spreading-code, achieving an effective spreading gain N_s . This essentially forms multiple TH “code-channels” between pairs of anchors and unlocalized nodes. In general, packets from an anchor node can be broadcast to several unlocalized nodes resulting in multiple packet receptions per packet transmission, but this complicates the analysis considerably. The transmit power of anchors is assumed to be constant and equal to P_T .
3. *TOA-based Range Estimation at unlocalized nodes:* An unlocalized node that receives a packet from an anchor can estimate the distance R between them based on the TOA of the packet within the slot, as shown in Figure 2.4-2. Since anchor nodes transmit packets at slot-transitions, the TOA of the packet within the slot is proportional to R . In order to eliminate range ambiguity, we assume $R \gg cT_s$, where c is the speed of light. Because our goal is to model localization accuracy, the contents of the packets are assumed to be the coordinates of the corresponding anchors. From a communications perspective, these packets could contain additional data, since only the TOAs of the packets are used to obtain range estimates.
4. *Multiple-Access Interference:* As several anchor nodes can transmit packets simultaneously at a slot transition, this can result in multiple-access interference (MAI) between simultaneously transmitted packets at unlocalized nodes. We assume that the multiple-access interference seen at an unlocalized node is independent from slot to slot. Further, the level of interference is assumed to be constant over the length of a slot.

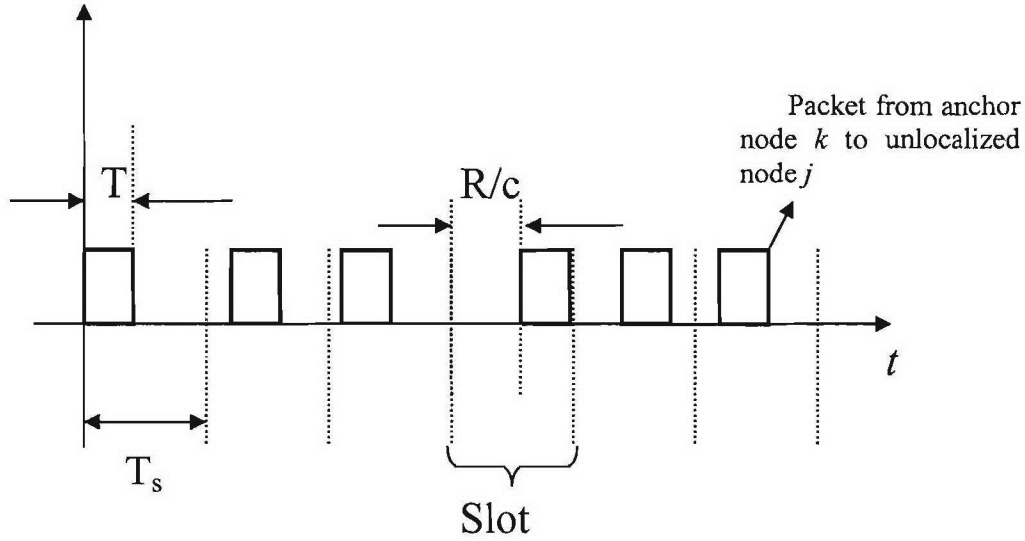


Figure 2.4-2 Slotted Packet Transmissions: based on the delay between a packet's arrival-time and the previous slot transition, an unlocalized node can estimate the distance between itself and the anchor that transmitted the packet. This assumes that the propagation delays are much smaller than the length of a slot.

5. *Successful reception of packets:* A packet is decoded successfully at an unlocalized node if the signal-to-interference-and-noise ratio (SINR) ξ at the receiver exceeds a threshold ξ_T , determined by the sensitivity of the receiver and the strength of coding scheme used. We assume that if the packet is decoded successfully, then a range estimate can be obtained based on its TOA within the slot.
6. *Traffic and Average Performance:* The traffic from anchors to unlocalized nodes is assumed to be balanced, and therefore the analysis of a single unlocalized node represents the generic average over all unlocalized nodes. Coupled with the assumption that the MAI is independent from slot to slot, this allows us to model the average performance by simply looking the behavior of a single "generic" unlocalized node over an arbitrary time-slot.

Due to the memoryless property of the Poisson distribution [Papoulis1991], without loss of generality, we assume that the generic unlocalized node lies at the origin. Based on the above assumptions, we first obtain the statistics of the SINR seen at the generic unlocalized node. Using these statistics, we can compute the average effective throughput of packets within the network. This then allows us to characterize the convergence of node location estimates to the true node locations.

Statistics of the Signal-to-Interference-and-Noise Ratio

The computation of the statistics of the SINR presented here closely follows the analysis presented in [Sousa1990]. Consider an anchor node A and an unlocalized node B . Let the distance between A and B be R . In a given slot, if node A transmits a packet to node B , the received signal power can be modeled as [Buehrer2004]

$$P_{r0} = \frac{K_P P_T}{R^\beta} \quad (2.4-2)$$

where P_T is the transmit power, β is the path-loss exponent in the propagation environment and K_p is a constant determined by the physical layer. At B , the received signal power from other interfering anchors that transmit packets in the same slot is given by

$$P_{rk} = \frac{K_p P_T}{r_k^\beta}, \quad k = 1, 2, \dots \quad (2.4-3)$$

where r_k is the distance between B and the k th interferer. The Gaussian model for the MAI in TH-PPM UWB systems was analyzed in [Win2000]. Applying this model to the interference seen at B from other interfering anchors, the Signal-to-Interference-and-Noise Ratio (SINR) ξ at B can be expressed as

$$\xi = \left(\frac{1}{\xi_0} + \frac{K_1}{N_s P_{r0}} \sum_k P_{rk} \right)^{-1} \quad (2.4-4)$$

where K_1 is a constant dependent on the receiver structure, ξ_0 is the Signal-to-Noise ratio (SNR) and P_{rk} represents the received power from the k th interfering anchor and k is the number of users. Using (2.4-3) and (2.4-4), this can be rewritten as

$$\xi = \left(\frac{1}{\xi_0} + \frac{K_1 R^\beta}{N_s} \sum_k \frac{1}{r_k^\beta} \right)^{-1} \quad (2.4-5)$$

The SINR ξ is a random variable, because it depends on the spatial locations of the interfering anchor nodes. Because in any slot the probability that an anchor node is transmitting is p , the set of interfering anchors form a spatial Poisson process [Sousa1990] with average density $\Lambda' = p\Lambda$. Suppose we define the “effective interference” as the random variable Y :

$$Y = \sum_k r_k^{-\beta} \quad (2.4-6)$$

Then Y represents the spatial dependence of the total interference seen from all interfering anchor nodes. It can be shown that [Sousa1990] for $\beta > 2$, the characteristic function of Y is:

$$\Phi_Y(\omega) = \exp \left(-p\pi\Lambda e^{-\pi/\beta} \Gamma \left(1 - \frac{2}{\beta} \right) \omega^{2/\beta} \right). \quad (2.4-7)$$

A closed-form expression for the probability density function (CDF) associated with the above characteristic function when $\beta = 4$, is known [Feller1966]:

$$F_Y(y) = \text{erfc} \left(\frac{p\pi^{3/2}\Lambda}{2\sqrt{y}} \right). \quad (2.4-8)$$

Packet Success Probability

For $\beta = 4$, from (2.4-6) and (2.4-8), the probability of the SINR ξ crossing the threshold ξ_T is given by

$$P_s = F_Y \left(\frac{N_s}{K_1 R^4} \left(\frac{1}{\xi_T} - \frac{1}{\xi_0} \right) \right) = \operatorname{erfc} \left(\frac{p \pi \Lambda R^2}{\sqrt{\frac{4 N_s}{K_1 \pi} \left(\frac{1}{\xi_T} - \frac{1}{\xi_0} \right)}} \right). \quad (2.4-9)$$

Since $\operatorname{erfc}(\cdot)$ is a monotonically decreasing function, we see that the probability, P_s , of successfully decoding a packet, (i) increases as the spreading gain N_s increases, and (ii) decreases as the transmission probability p , the distance R and the density of anchor nodes Λ increase. It must be noted that although the results here are derived for $\beta = 4$, similar trends are observed for other values of β .

Based on this expression, we can now compute the average effective throughput of packets from anchor nodes to unlocalized nodes. In terms of the packets per slot, the effective throughput is simply the probability of successful packet delivery at an unlocalized node. In terms of the anchor A and unlocalized node B , the probability of the successful reception of a packet at B is given by

$$\eta = \Pr \{A \text{ transmits a packet}\} \cdot \Pr \{B \text{ does not transmit a packet}\} \cdot \Pr \{\text{packet from } A \text{ received} \mid B \text{ does not transmit a packet}\} \quad (2.4-10)$$

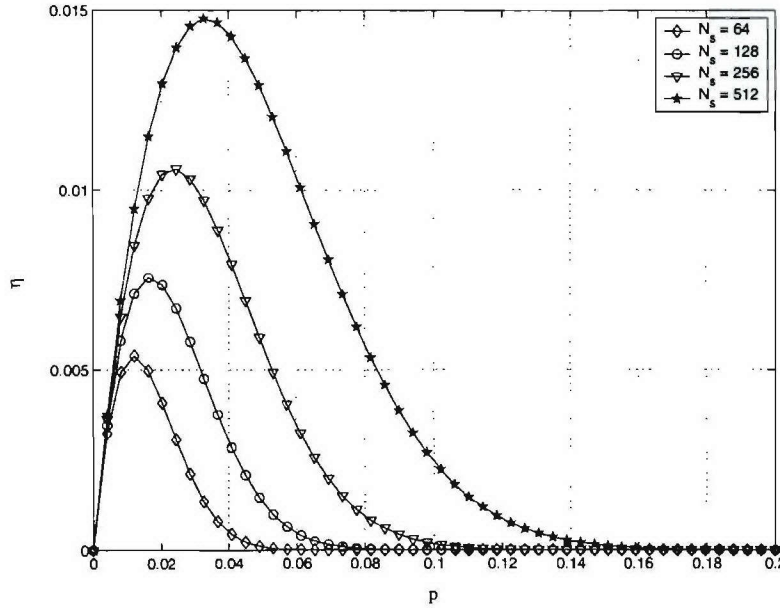


Figure 2.4-3 The average throughput per slot η versus the packet transmission probability p for different values of the spreading gain N_s . The values of the other parameters are: $R = 5$ meters, $K_1 = 10$, $\xi_T = 10$ dB, $\xi_0 = 20$ dB, $\Lambda = 0.5$ meter⁻².

From the analysis provided in [Sousa1990], the expression for η has been shown to be well approximated by

$$\eta = (1-p)(1-e^{-p})P_s.$$

From the above equations, we obtain

$$\eta = (1-p)(1-e^{-p})\operatorname{erfc}\left(\frac{p\pi\Lambda R^2}{\sqrt{\frac{4N_s}{K_1\pi}\left(\frac{1}{\xi_T}-\frac{1}{\xi_0}\right)}}\right). \quad (2.4-10)$$

Figure 2.4-3 shows the average throughput η versus the packet transmission probability p for different values of the spreading gain N_s . We see that as the spreading gain increases, the average throughput for a given value of p increases, due to increase in the resistance to MAI. We also see that there is an optimal value of p for which the average throughput is maximized. This value of p can be obtained by setting the partial derivative of η with respect to p in (2.4-10) to zero, and solving for p .

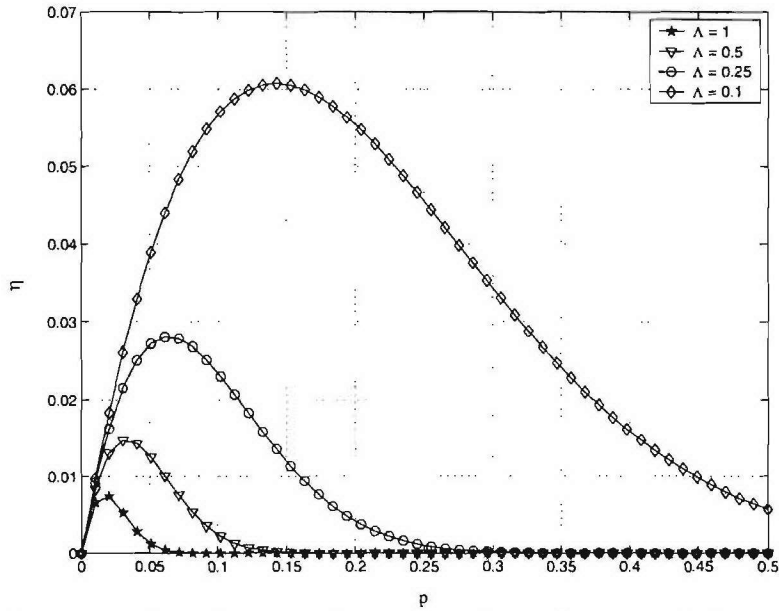


Figure 2.4-4 The average throughput per slot η versus the packet transmission probability p for different values of the node density Λ . The values of the other parameters are: $R = 5$ meters, $K_1 = 10$, $\xi_T = 10$ dB, $\xi_0 = 20$ dB, $N_s = 512$.

Figure 2.4-4 shows the average throughput η versus the packet transmission probability p for different values of the anchor density Λ . We see that as the anchor density increases, the average throughput for a given value of p decreases. This is because, for a fixed value of p , as the anchor node density increases, the average MAI seen at an unlocalized node increases.

Convergence of the Localization Error

Since η is the probability that an unlocalized node decodes a packet successfully in a given time-slot, it is also the probability that the unlocalized node obtains a range estimate during the slot. Starting at $t = 0$, the probability that m range estimates are accumulated by an unlocalized node by time $t = nTs$, is given by

$$p_m = \binom{n}{m} \eta^m (1-\eta)^{n-m}.$$

Therefore, the average localization error $\Omega(t)$ of the unlocalized node at time $t = nTs$ is given by

$$E\{\Omega(t)\} = \sum_{m=0}^n p_m \Omega_{x,m} = \sum_{m=0}^n \binom{n}{m} \eta^m (1-\eta)^{n-m} \Omega_{x,m} \quad (2.4-11)$$

Applying the lower bound from our previous work for $\Omega_{x,m}$, we have

$$E\{\Omega(t)\} \geq \sum_{m=0}^n \binom{n}{m} \eta^m (1-\eta)^{n-m} \left(\frac{4}{\gamma_m} \right) \quad (2.4-12)$$

Assuming equal range variances $\sigma_i^2 = \sigma_0^2$, we obtain

$$E\{\Omega(t)\} \geq \sum_{m=0}^n \binom{n}{m} \eta^m (1-\eta)^{n-m} \left(\frac{4\sigma_0^2}{m} \right) \quad (2.4-13)$$

Figure 2.4-5 shows the variation of the average localization error computed using (2.4-13) versus η for different time-instants. As conjectured, we see that as the effective throughput increases, the average localization error at each time-instant decreases. Further, we see that as time progresses, the average localization error decreases due to the accumulation of a larger number of range estimates.

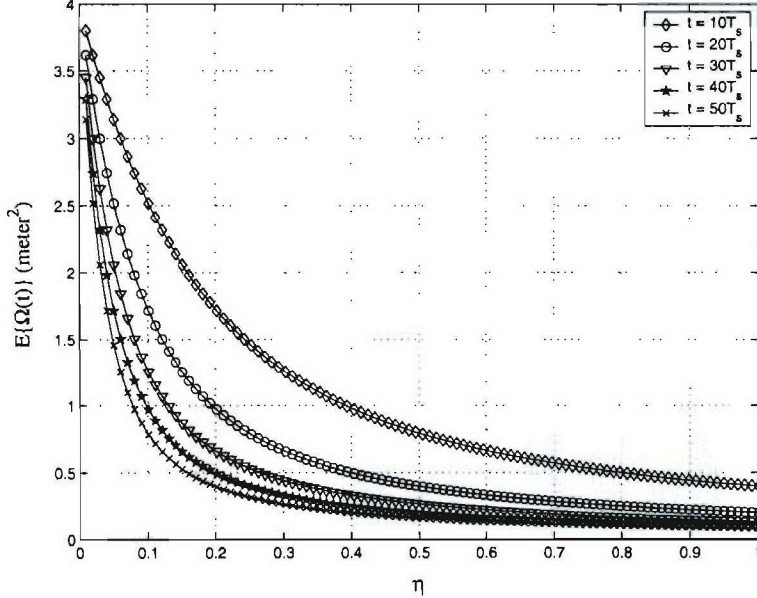


Figure 2.4-5 The average localization error $E\{\Omega(nT_s)\}$ versus η for different time-instants; The values of the other parameters are: $R = 5$ meters, $K_1 = 10$, $\xi_T = 10$ dB, $\xi_0 = 20$ dB, $N_s = 256$, $\sigma_0 = 1$ meter.

Figure 2.4-6 shows the average localization error at $t = 100T_s$ for different values of the transmission probability p . The most important observation to be made here is that the value of p that maximizes the average throughput η in Figures 3 and 4 also minimizes the average

localization error. This validates our conjecture that maximizing the average throughput η minimizes the average localization error $E\{\Omega(t)\}$, at any instant t .

Therefore, we have shown that the problem of minimizing the average localization error in the modeled UWB position-location networks is identical to the commonly studied problem of maximizing the throughput of packets within the network. This is intuitive since the accuracy of node location estimates was shown to be dependent on the *amount* of range information available. As range information is available through the TOAs of packets, increasing the rate of transport of this range information over the network should improve node localization accuracy.

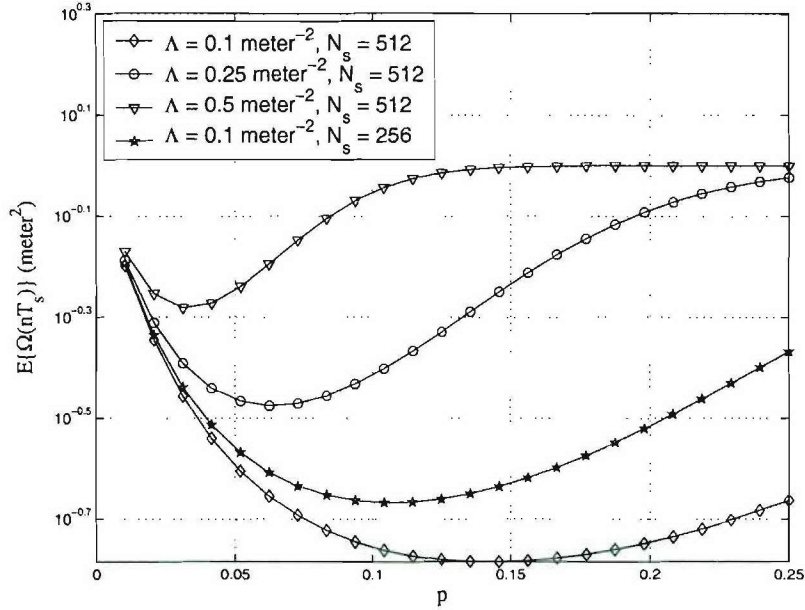


Figure 2.4-6 Lower bound on the average localization error $E\{\Omega(t)\}$ at $t=100T_s$ versus the transmission probability p . The value of $\sigma_0 = 0.5$ meter.

References

- [Win1998] M. Z. Win and R. A. Scholtz, "Impulse radio: How it works," *IEEE Communications Letters*, vol. 2, pp. 36–38, February 1998.
- [Papoulis1991] A. Papoulis, *Probability, Random Variables and Stochastic Processes*. 1991. 3rd Edition, McGraw-Hill Inc.
- [Buehrer2004] R. Buehrer, W. Davis, A. Safaai-Jazi, and D. Sweeney, "Ultrawideband propagation measurements and modeling – DARPA NETEX Final Report," Tech. Rep., January 2004. Available at http://www.mprg.org/people/buehrer/ultra/darpa_netex.shtml.
- [Win2000] M. Z. Win and R. A. Scholtz, "Ultra-Wide Bandwidth Time-Hopping Spread-Spectrum Impulse Radio for Wireless Multiple-Access Communications," *IEEE Transactions on Communications*, vol. 48, April 2000.

[Sousa1990] E. Sousa and J. A. Silvester, "Optimum transmission ranges in a direct-sequence spread-spectrum multihop packet radio network," *IEEE Journal on Selected Areas in Communications*, vol. 8, pp. 762–771, June 1990.

[Feller1966] W. Feller, *An Introduction to Probability Theory and its Applications*. vol. II, Wiley, 1966.

2.4.1.2 Subtask 2.4.1b Cross-Layer Design of Cooperative UWB Networks

Introduction

During this period, we investigated several questions raised in the previous report. First, we explored the reason why the results indicated that the exclusion region is not needed for centralized UWB systems. Second, the near-far problem is examined for both centralized and distributed UWB systems. Finally, at the physical layer, optimal transmit UWB sequences are also examined for interference mitigation as well as their impact on scheduling and routing.

Accomplishments during reporting period:

1. Routing Protocol and Traffic Flows

We assume that all nodes always have data to send, and all available link capacities are used to maximize the network performance. Two routing protocols are examined in the context of cross-layer design: (1) nodes do not relay data for others, which is called "Direct Routing Protocol (DIR)" and (2) nodes are willing to relay data for others and multi-hop paths are defined based on a minimum energy cost function and is called "Minimum Energy Routing (MER)". The cost function considers the average transmit power constraints as well as propagation loss. Since the optimal sequences, which applied later in the physical layer, adapted to the time-varying channel condition, the cost function didn't including any channel information. It should be noted that, given the statistical variation of wireless links, the channel conditions could be introduced into the cost function of a static wireless network (here static wireless network is defined as a network that without mobile nodes). However, we would rather handle time variation in the physical layer through the use of sequence adaptation.

2. Exclusion Regions and Rate Adaptation

Because the achievable rate could be approximated by signal-to-interference ratio (SIR) for a white Gaussian noise channel, the total interference for such a channel plays an important role. To reduce the interference, an exclusion region is introduced. The exclusion region is defined such that inside the exclusion region, no concurrent transmissions are permitted.

3. MAC Layer

We assume that for the MAC protocols examined here, the MAC always knows the state of the system, and there is no delay associated with scheduling time slots that correspond to the system state. Two specific scheduling algorithms are analyzed in this report. The first scheme uses a combination of TDMA to handle multiple flows through a single node and CDMA to allow multiple concurrent transmissions. The second scheme is a pure TDMA scheme.

4. Power Constraints

In our design we assume that all nodes assume have sufficient battery power and the optimization goal is to maximize the output utility of the wireless network, while the transmit power is confined to be less than the averaged maximum power.

5. Physical Layer

The physical layer is based on indoor non-line of sight (NLOS) channels which are randomly assigned to each link of networks. Each channel is based on channel impulse response measurements taken at the Mobile and Portable Radio Research Group (MPRG) at Virginia Tech. Furthermore, two optimal sequences are chosen during the test, one maximizes the output SNR at the receiver based on the multipath channel, while the second sequences is chosen to maximize the output SINR.

i.) Channel Matrix

The principle behind the optimal sequence algorithm is to design the transmit sequence based on the channel matrix. The channel matrix can be written as:

$$H_{m \times n} = \begin{bmatrix} h_0 & 0 & \cdots & 0 \\ h_1 & h_0 & \cdots & 0 \\ \vdots & \vdots & \ddots & \vdots \\ h_{N_x-1} & h_{N_x-2} & \cdots & h_0 \\ 0 & h_{N_x-1} & \cdots & h_1 \\ \vdots & \vdots & \ddots & \vdots \\ 0 & 0 & \cdots & h_{N_x-1} \end{bmatrix} \quad (2.4-14)$$

where h_i is the resulting channel coefficient after passing the received signal through a pulse matched filter, p_k is the signal power of the k^{th} user, X_k is the transmit sequence vector of the k^{th} user and b_k is the data bit transmitted by the k^{th} user. The received signal vector before despreading is:

$$r_i = \sum_{k=1}^M \sqrt{p_k} H_{ki} X_k b_k + n \quad (2.4-15)$$

Where n is a vector of zero-mean Gaussian random variables with variance $\sigma^2 = \frac{N_0}{2}$.

ii.) Optimal SNR & SINR Sequences

For one transmit and receive pair, with the transmit channel $H_{m \times n}$, if its transmit sequence vector X_k is chosen to be the eigen-vector corresponding to the maximum known eigen-value of channel matrix $H^T H$, the transmit sequence X_k is termed the optimal SNR sequence, denoted as s_k . Maximizing SNR at the receiver, the correlation template is matched to the received sequence and is the product of HX_k .

For a multi-access system, $I_k = \sum_{j \neq k}^{N-1} \sqrt{p_j} \hat{H}_{ji} X_j b_j$ and the interference-plus-noise correlation matrix is defined as:

$$Z_k = I_k * I_k^T + \sigma^2 I \quad (2.4-16)$$

where I is the identity matrix. Now if X_k is the eigen-vector corresponding to the maximum eigen-value of matrix $H_{kk}^T Z_k^{-1} H_{kk}$, X_k is rewritten as s_z , the optimal SINR sequence. To form an MMSE receiver, the unit-energy correlation template equals the product of $Z_k^{-1} H_{kk} X_k$.

iii.) UWB Sequence Adaptation Algorithms

By adopting an optimal SINR/SNR sequence and its corresponding template at the UWB receiver, three algorithms are proposed to mitigate interference and improve output utility of the whole network for both centralized and distributed scenarios.

Algorithm I: One of the concurrent flows transmits using the optimal SINR sequence and also uses an MMSE receiver. All of the other links maintain the use of the maximum SNR sequence and a matched filter receiver.

Algorithm II: All concurrent flows only adopt the optimal SNR sequence, and the matched filter receiver.

Algorithm III: All concurrent flows adopt the optimal SNR sequence, but use MMSE receivers to decorrelate the received signals.

Simulation Results

Simulation results are shown in Figure 2.4-7 in terms of the average network utility for the case of MER. We can see that when the number of nodes in a wireless network is five, an exclusion region is unnecessary, and output utility is increased by simply transmitting all flows concurrently. This is due to the fact that when the number of nodes in the network is small, the interference between nodes can be effectively mitigated by simply transmitting the optimal SNR/SINR sequence. Without the need for the exclusion region, more concurrent flows can be assigned to the same time slot, which helps to improve the output utility, under same routing protocol and transmit algorithms. To demonstrate, a simple example is, given as follows: Let node 1 indicate the base station. Now, based on the assumed node configuration, four tasks are needed to transmit data. Specifically, the flows are from node $2 \rightarrow 3 \rightarrow 1$, $3 \rightarrow 1$, $4 \rightarrow 1$ and $5 \rightarrow 1$ assuming MER routing. The final time slots are assigned as in 2.4-1.

Table 2.4-1 MAC layer under MER Routing Protocol for a Small Centralized Wireless Network

All sending together				Exclusion Region			
Time slot 1	Time slot 2	Time slot 3	Time slot 4	Time slot 1	Time slot 2	Time slot 3	Time slot 4
$2 \rightarrow 3$	$3 \rightarrow 1$	$3 \rightarrow 1$	$5 \rightarrow 1$	$2 \rightarrow 3$	$3 \rightarrow 1$	$3 \rightarrow 1$	$5 \rightarrow 1$
$4 \rightarrow 1$			$2 \rightarrow 3$	$4 \rightarrow 1$			

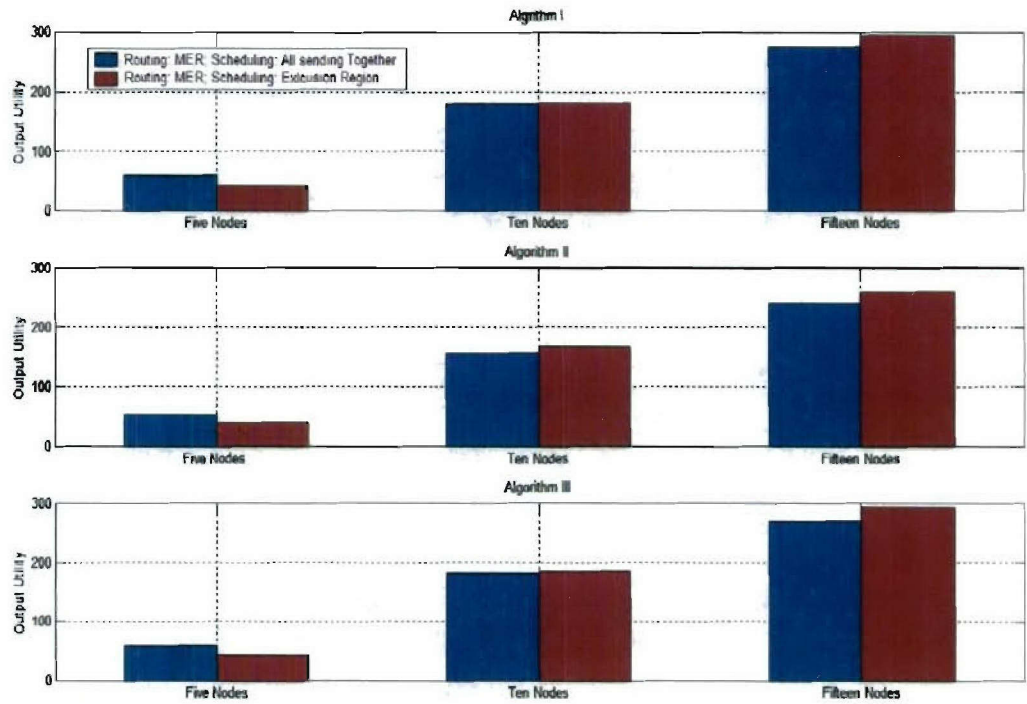


Figure 2.4-7 The Output Utility under MER routing protocol.

Now, it is obvious that as the size of the wireless network grows, more and more interference is introduced, and the output utility is maximized with the help of an exclusion region around the receiver. Furthermore, for a centralized network, the best result is given by the combination of MER routing protocol, exclusion region assignment, optimal SNR transmit sequence and an MMSE Receiver design. However, Algorithm I also provides performance under the same MAC and routing protocols which is very close, as shown in Figure 2.4-8. Further, it can be shown that this conclusion is also valid for distributed scenarios.

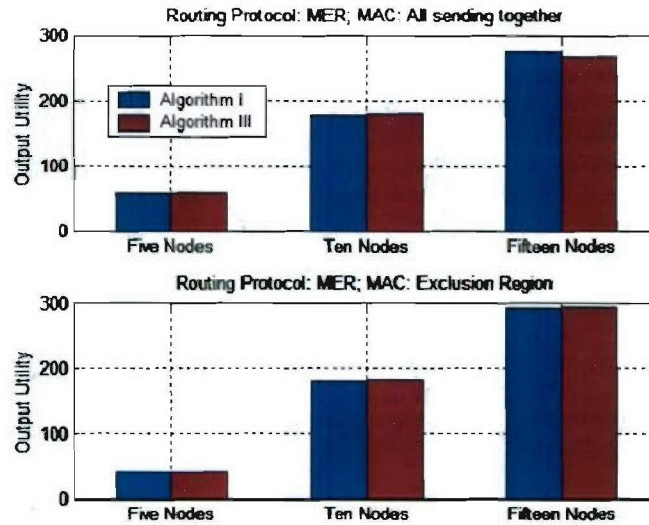
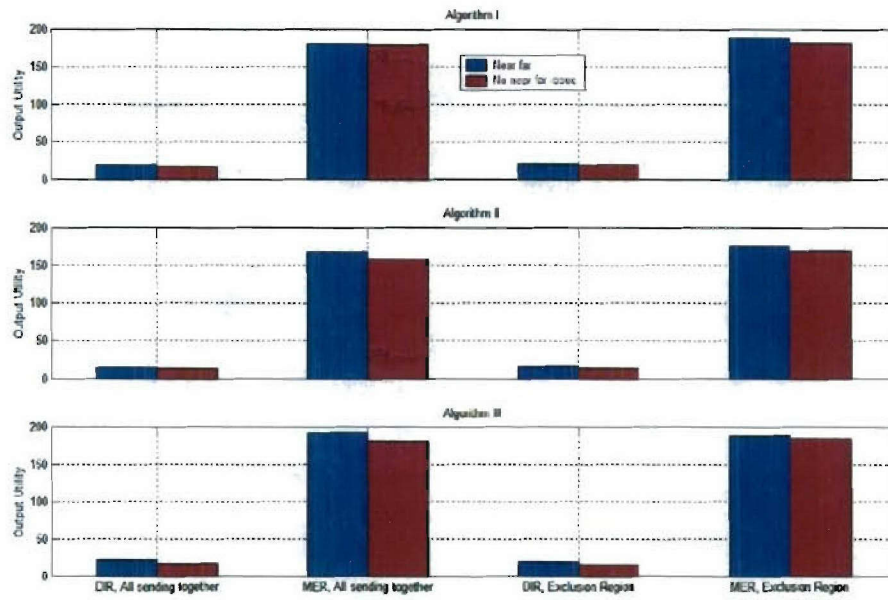


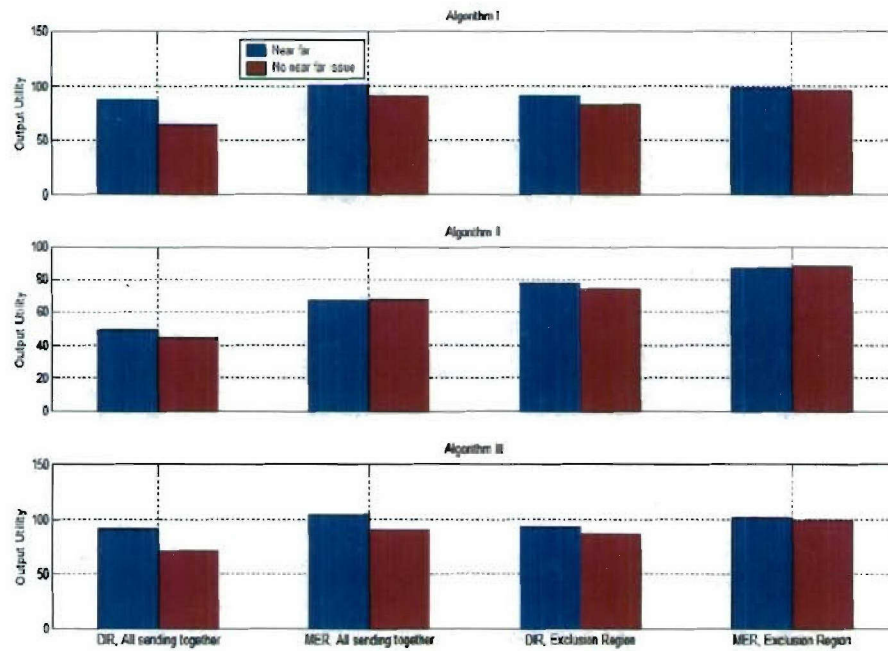
Figure 2.4-8 The Output Utility under different MAC and transmit algorithms.

Near-Far Issue

During this quarter, we also investigated system performance in the presence of the near-far problem for concurrent flows. Output Utility is simulated for both distributed and centralized wireless network to examine this. It is shown in Figure 2.4-9 that all three transmit algorithms successfully combat the near-far problem when the number of nodes in the network is 10, since under MER routing there is not a substantial amount of interference generated. Furthermore, it seems all three algorithms benefit the distributed wireless network more than the centralized network. However, a conclusion cannot be reached at this point, without further investigation for dense networks.



(a) Centralized system



(b) Distributed system

Figure 2.4-9 Output Utility for cross-layer network.

2.4.4 Productivity

Journal publications

1. J. Ibrahim and R.M. Buehrer, "Two-Stage Acquisition for UWB in Dense Multipath," paper accepted, *IEEE Journal on Selected Areas in Communications*, Issue on Ultra Wideband Wireless Communications -- Theory and Applications, second quarter 2006.
2. J. Ibrahim, R. Menon, and R.M. Buehrer, "UWB Signal Detection Based on Sequence Optimization for Dense Multipath Channels," paper accepted, *IEEE Communications Letters*.
3. J. Ibrahim and R.M. Buehrer, "NBI Mitigation for UWB Systems Using Multiple Antenna Selection Diversity," submitted to *IEEE Transactions on Vehicular Technology*.

Conference publications

1. J. Ibrahim and R.M. Buehrer, "A UWB Multiple Antenna System for NBI Mitigation under Rayleigh and Ricean Fading," paper accepted, *IEEE International Conference on Communication*, ICC 2006, June 2006.
2. J. Ibrahim and R.M. Buehrer, "A Novel NBI Suppression Scheme for UWB Communications Using Multiple Receive Antennas," *IEEE Radio and Wireless Symposium*, RWS 2006, January 2006.
3. S. Venkatesh, N. Kumar, and R.M. Buehrer, "A Spread-Spectrum MAC Protocol for Impulse-Radio Networks," *IEEE Vehicular Technology Conference*, September 2005.
4. S. Venkatesh and R. M. Buehrer, "Power-Control for UWB Position-Location Networks", accepted for publication, 2006 IEEE International Conference on Communications (ICC 2006), 11-15 June 2006, Istanbul, Turkey.
5. S. Venkatesh and R. M. Buehrer, "Multiple-Access Design for UWB Position-Location Networks", accepted for publication, 2006 IEEE Wireless Communications and Networking Conference (WCNC 2006), 3-6 April 2006, Las Vegas, USA.
6. S. Venkatesh and R. M. Buehrer, "A Linear Programming approach to NLOS error mitigation in Sensor Networks", accepted for publication, Fifth International Conference on Information Processing in Sensor Networks (IPSN '06), 19th-21st April 2006, Nashville, USA.

Students supported

Qiao Chen, January. 1, 2005 – present
Swaroop Venkatesh, January. 1, 2005 – present
Jihad Ibrahim, January. 1, 2005 – present

Faculty supported

R. Michael Buehrer, Jan. 1, 2005 – present
Scott Midkiff, Jan 1, 2005 - present

3. Task 3 Visualization of Wireless Technology and Ad Hoc Networks

3.1 Overview

Task Objective: The objective of this task is to identify and investigate AWINN enabling technologies for the Close-in Sea Basing.

Organization: The task is directed by Ali Nayfeh and Rick Habayeb. The personnel list follows.

Rick Habayeb, faculty

Ali Nayfeh, faculty

Summary: The main activity during this period was integrating the crane controller into a fielded crane. This provides the bridge to transition the UWB ranging technology into the Sea Basing environment.

3.2 Task Activities for the period

This quarter we had a golden opportunity to establish a potential transition path for the AWINN technologies into the Sea Basing environment. In the last two quarters, the team was given approval to piggy-back on a fielded crane at the seaport of Jeddah, Saudi Arabia. The crane controller developed at VT was integrated into a fielded crane at the seaport. Experiments to evaluate the crane controller are still ongoing.

For the VT anti-sway control system to work, the “sway angle” or the “pendulation angle” of the container must be accurately measured and fed-back to the control algorithm. In a live, full-scale test of a quay-side container crane, a “contact” sway sensor must be rugged and able to withstand very large forces from multiple sources. A “contact” sway sensor measures the cable angle through a mechanical linkage attached to the crane hoist cables.

The forces on the sensor arise from the hoist cables. The cables are 30-mm thick greased and galvanized steel. The cables are braided, so whenever the crane moves, a motion similar to that of a very high-speed screw is exerted on anything clamping the cables. Also, whenever the crane moves its base position perpendicular to the motion of the trolley (gantry) oscillations can be induced in that direction. Furthermore, due to day-to-day operations, other uncommon forces can be exerted on the system, such as if the operator lets the hoist cables slack and then begins to lift cargo, the cables “snap” much like a whip.

Figure 3-1 shows the complete design of our sway sensor assembly. All of the materials used were either high strength stainless steel (316) or aircraft grade aluminum (7075-T6). The bottom assembly can be seen in Figures 3-2 and 3-3, and the top assembly in Figure 3-4. The sensor has two degrees of freedom: in-plane with the trolley (and sway motion) of the cargo and out-of-plane with the trolley to compensate for the gantry motion. The hoist cable passes through two spring-loaded pulleys in the bottom assembly.

Figure 3-2 shows the configuration for the bottom assembly. In the original design, we used two spring-loaded pulleys sandwiched between two aluminum plates, held together by stainless steel rods. We were hoping that the spring loaded pulleys will keep the sensor firmly attached to the hoist cable, and at the same time absorb most of the forces from the braided cable. Unfortunately, due to the abrasive nature of the hoist cables, the cast-iron material in the

pulleys was being worn away. We had to reinforce the pulleys with stainless steel discs to provide support for the cast-iron and as an added safety precaution. If the cable were to escape the pulley, it could cause severe damage to the remainder of the sensor. Also, in the original design, we used rollers made out of thin stainless steel to prevent any snapping force from the cables to strike the rest of the assembly and to make sure that the sensor alignment is correct in the horizontal axes. Unfortunately, the snapping and abrasiveness of the hoist cables caused the original rollers to crack and break. We replaced these rollers with solid nylon rollers with a stainless steel shaft. The nylon absorbs impacts from the cables better than stainless steel and the thicker material lasts longer than the originally used thinner material.

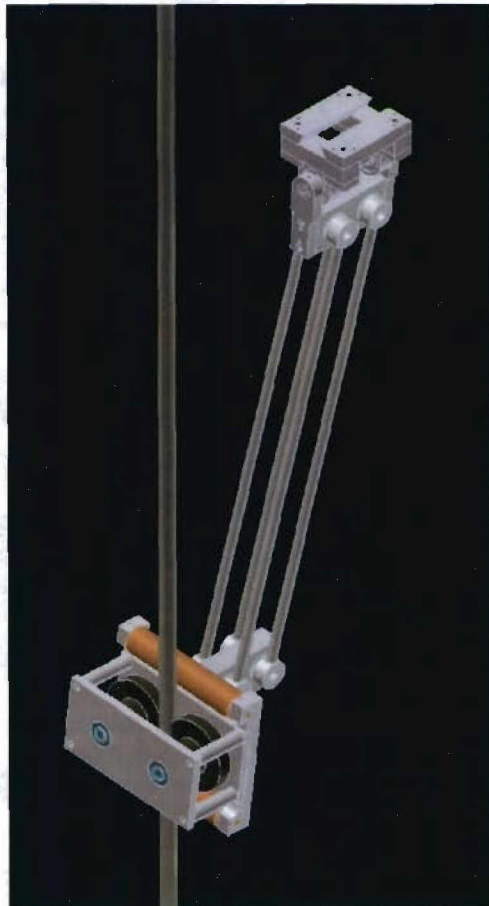


Figure 3-1 Complete sway sensor design.

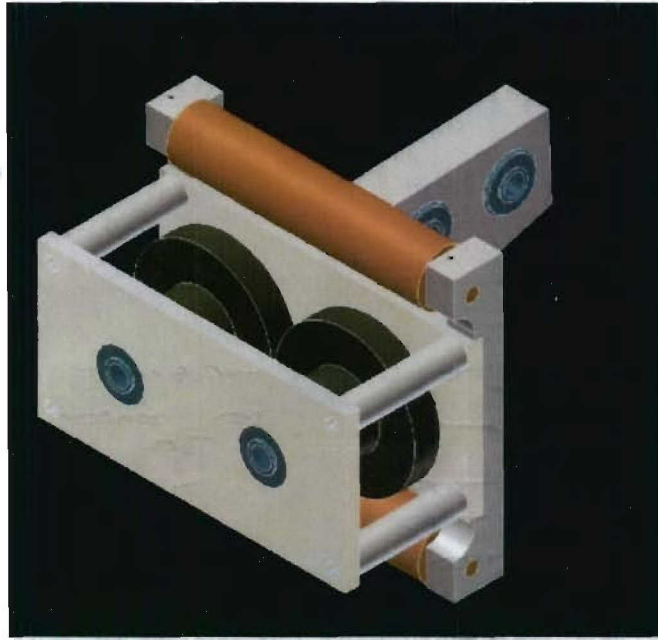


Figure 3-2 Isometric view of the bottom part of the sway sensor.

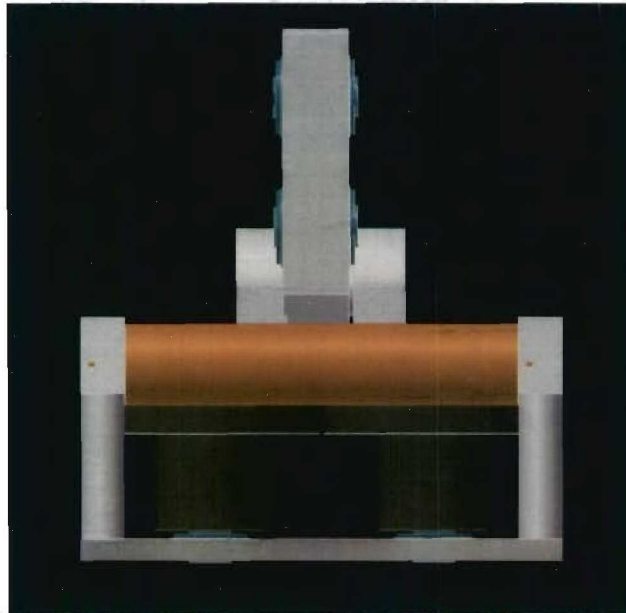


Figure 3-3 Top view of the bottom part of the sway sensor.

Figure 3-3 shows a top view of the bottom assembly. The plate behind the assembly attaches to a “four-bar” mechanism that connects to the top assembly. The four-bar mechanism is used to keep proper alignment of the sensor assembly and for strength.

Figure 3-4 shows the top assembly. An absolute encoder is mounted on the shaft go between the “Y” shaped plate and arms on the bottom part. This is the direction of motion that we want to measure. This assembly is mounted directly to the crane structure by use of a “dovetail”

mount. The materials in the dovetail are stainless steel. Aluminum is used on the lower “Y” shaped plate and arms to conserve weight.

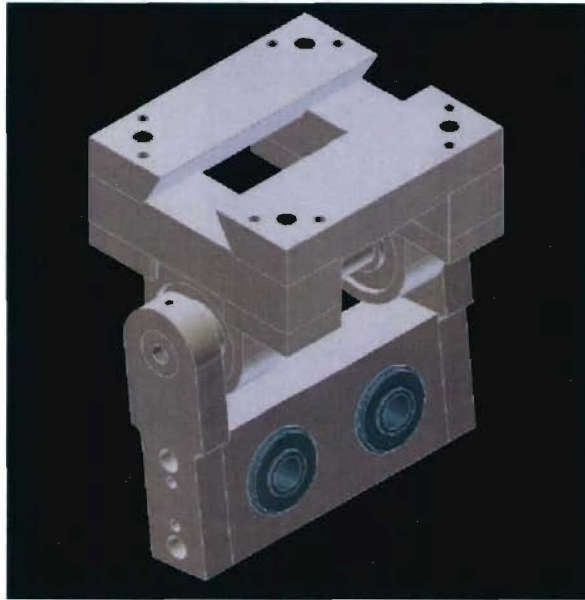


Figure 3-4 Isometric view of the top part of the sway sensor.

The entire assembly for one sensor weighs approximately 85 lbs. We need two of them for each crane. The team attempted to machine eight designs in Saudi Arabia, but all of them could not withstand the harsh environment. This is why we have switched to the very expensive materials of high strength stainless steel (316) and aircraft grade aluminum (7075-T6). Moreover, we could not get the precision machining in Saudi Arabia and hence machined all of the fixtures in the US.

Using these modified contact sensors, we were able to do 30 moves per hour (more than their skilled operators can do) WITHOUT the memory feature of the SSC controller. We used a container and picked it up from a truck and took it to the sea side to a specific location (55 m distance) and then brought it back on the truck. This operation repeated and we were able to home on the container very easily. So far, we have been getting positive response from the operators. We have started training some of the operators on the system. We hope to be able to use the system to unload the next ship which comes to the Jeddah Port.

The team’s experience demonstrates without ambiguity the need for non-contact sensors, such as with a UWB based sensor subsystem..

3.3 Importance/Relevance

ForceNet is the Navy implementation plan for Network Centric transformation. There are three fundamental concepts in ForceNet: Sea Shield, Sea Strike, and Sea Basing. Sea Basing is projecting joint operational independence. There several technological challenges associated with the Navy vision for Sea Basing. The first major challenge is the Close-in command, control, and communication (C3). Currently, ship-to-ship close-in C3 during UNREP is tedious, time consuming, archaic, and labor intensive. This project will explore, develop, visualize, and integrate the high payoff enabling AWINN technologies for the Close-in sea basing environment.

3.4 Productivity

Students Supported

N. Nayfeh- January 25, 2005 to present
M. Daqaq – January 25, 2005 to present
O. Marzouk- January 25, 2005 to present

4. TASK 4 Testing and Demonstrations

4.1 TIP#1 Distributed MIMO UWB sensor networks incorporating software radio

Numerous factors associated with regulations, business, technology, and social behavior naturally and logically speak in favor of wireless mesh networking. Since the network nodes will be battery-driven, energy efficiency (or network life-time) is a critical design consideration. Surprisingly, there has been only a few published works in the area of energy efficiency of ad-hoc networks until fairly recently. Most existing solutions for saving energy revolve around the reduction of radio transceiver power by selectively sending the receiver into a sleep mode and choosing routes that require many shorter hops instead of a few very long hops (to reduce the transmit power). More recently, it has been recognized that the density of the communication nodes in an ad-hoc network creates an intrinsic spatial diversity that could be exploited in order to substantially reduce the energy consumption of each device. Cooperating nodes in both transmit and receive clusters pool their antenna resources together to form “virtual antenna arrays” as shown in Fig 4.1-1 and achieve similar benefits offered by multiple-input-multiple-output (MIMO) systems without the use of antenna arrays. For example, [1]-[4] have studied performance improvements in terms of capacity, energy efficiency, and average bit error rate (ABER) for several cooperative relaying strategies.

However, all of the above-mentioned studies have ignored some practical aspects of distributed MIMO networks. For example, it is implicitly assumed that the transmitters and receivers are perfectly synchronized in time. But clock synchronization errors will typically be present due to the lack of a common reference driving the transmitter local oscillators. It is also not possible for the receiver to track and correct the signal offset in every cooperative link which results in sampling offset error for signals received from certain transmitting nodes. Timing offsets may also result from different propagation delays resulting from different transmitter-receiver distances if they are not compensated at the transmitter (e.g., imperfect location prediction due to GPS outages). The combined effects create intersymbol interference (ISI) which can significantly degrade the performance of distributed MIMO. The effects of unbalanced cooperative links and mixed-fading were also ignored in the above studies.

Recently, [5] examined the effect of time synchronization errors on the performance of two distributed multiple-input-single-output (MISO) schemes. Their analysis is based on Gaussian approximation of the ISI terms and averaging over the joint probability density function (PDF) of random variables representing channel gains over multiple adjacent symbol durations. There are two basic shortcomings of this approach. First, the joint PDF is difficult to compute and is only known for certain distributions. Secondly, this approach is computationally cumbersome because it involves an evaluation of nested multiple integrals equal to the number of transmitting nodes. Consequently, the analysis in [5] is restricted to only an AWGN channel. Simulation results were also provided for the Rayleigh fading case but limited to SNR less than 6 dB (due to excessive simulation run time) that correspond to the noise limited case (does not capture the noise floor due to ISI). In [6], numerical results for the pair wise error probability of a specific error pattern in Rayleigh fading is obtained by employing Gaussian assumption for the ISI terms and semi-analytic simulation. To evaluate the ABER, averaging over all possible error patterns will be required, which is again a very time consuming effort. Given the computationally complex nature of the ABER analysis even for the specific Rayleigh fading case apparent from the above discussions, this article derives an upper bound for the desired ABER in a generalized fading

channel with the aid of an alternative integral formula for the Gaussian probability integral $Q(\cdot)$ (based on Gil-Pelaez inversion theorem [7]) and frequency-domain analysis.

To enhance the understanding of our approach, we will consider a 2x1 distributed MISO system although the analysis can be extended to consider general cooperative MIMO networks. We also choose to analyze orthogonal space-time block coding (OSTBC) scheme because it is easier to implement and it is a bandwidth efficient scheme. Different from [5], the analysis presented here can consider the effect of both ISI from any specified number of adjacent symbols as well as cross-symbol interference from the symbols transmitted from cooperating nodes. Our analytical framework can also treat the case of non-identical fading statistics over different cooperative links which is more probable in a realistic distributed MIMO network.

First we provide details the distributed OSTBC 2x1 MISO system model. Next, we present a frequency-domain analysis technique for computing the ABER performance of distributed MISO with timing synchronization errors over generalized fast fading channels. Selected simulation and computational results are then presented.

- Effect of Pulse Shaping on Distributed OSTBC

Among various diversity/multiplexing MIMO solutions, distributed OSTBC is an attractive solution for energy-constrained sensor networks because it does not require additional bandwidth and possesses low encoding-decoding complexity. To simplify our analysis we consider a distributed MISO system where a cluster of nodes transmit to a single receive node. Further, it is assumed that the nodes in the transmitting cluster are able to exchange data and coordinate among themselves in an error free high SNR mode. The primary focus is to analyze the effect of time synchronization error on parallel transmission alone. This analysis can be extended in future to include the effect of imperfect intra-cluster communication on the end-to-end ABER performance of a distributed OSTBC system by using the method presented in [3].

We consider a 2x1 MISO system where two nodes cooperate to transmit OSTBC codewords as described in [8]. It is assumed that the channels between the distributed transmitters and the receiver are independent (transmit antennas are far apart) and undergo slow frequency non-selective fading. For coherent STBC under perfect synchronization the received signal model after some manipulation as shown in [9] can be written as

$$\begin{bmatrix} r_1 \\ r_2 \end{bmatrix} = \begin{bmatrix} h_1 & h_2 \\ -h_2^* & h_1^* \end{bmatrix} \begin{bmatrix} s_{l,1} \\ s_{l,2} \end{bmatrix} + \begin{bmatrix} n_l \\ -n_{l+1}^* \end{bmatrix} \quad (4.1-1)$$

where r_l and r_{l+1} are received signals during l^{th} symbol duration and $l+1^{th}$ symbol duration respectively. s_{l1} and s_{l2} are the symbols transmitted by cooperating transmit nodes one and two, respectively, corresponding to the space-time block code transmitted at l^{th} symbol duration. The h_l

channels are assumed to be quasi-static over the duration of the block code. Hence, h_1 and h_2 represent the random channel gains from transmit antenna one and two respectively. The channel gain can be expressed as

$$h_m = \alpha_m \exp(j\theta_m) \quad (4.1-2)$$

where α_m is a random amplitude process (fading), θ_m is the uniformly distributed random phase process. n_l and n_{l+1} are additive white Gaussian noise terms corresponding to the received symbol durations with zero mean and a two sided power spectral density equal to $N_0/2$.

The pulse shaped symbol at the output of the receiver in the absence of noise and fading, corresponding to one of the transmitting antennas can be expressed as

$$s(t) = \sum_{l=-\infty}^{\infty} b_l g(t-lT) \quad (4.1-3)$$

Where b_k is an independent random variable that represents transmitted binary data sequence taking values $\{1, -1\}$ with equal probabilities. $g(t)$ is the output at the receiver of the pulse shaped waveform used for symbol transmission and T is the symbol duration. In discrete form (4.1-3) can be written as

$$s = \sum_{l=-\infty}^{\infty} b_l g_l \quad (4.1-4)$$

The received signal block starting at k^{th} symbol time duration is now given by

$$\begin{bmatrix} r_k \\ r_{k+1} \end{bmatrix} = \begin{bmatrix} \sum_{m=1}^2 h_{k,m} b_{k,m} g_{k,m} + \sum_{m=1}^2 \sum_{\substack{l=-\infty \\ l \neq k+1}}^{\infty} h_{l,m} b_{l,m} g_{k-l,m} \\ \sum_{m=1}^2 h_{k,m} b_{k+1,m} g_{k+1,m} + \sum_{m=1}^2 \sum_{\substack{l=-\infty \\ l \neq k+1}}^{\infty} h_{l,m} b_{l,m} g_{k-l+1,m} \end{bmatrix} + \begin{bmatrix} n_k \\ n_{k+1}^* \end{bmatrix} \quad (4.1-5)$$

The subscripts k and l represent the symbol sampling time. m represents the transmit antenna from which the symbol was transmitted. The desired portion of the received signal is given by

$$r_{k,desired} = \sum_{m=1}^2 h_{k,m} b_{k,m} g_{k,m} \quad (4.1-6)$$

The ISI portion of the received signal is given by

$$r_{k,isi} = \sum_{m=1}^2 \sum_{\substack{l=-\infty \\ l \neq k}}^{\infty} h_{l,m} b_{l,m} g_{l-k,m} \quad (4.1-7)$$

It should be noted that in (4.1-6), the channel gains ($h_{k,m}$) are assumed to be constant over two symbol durations for the desired part of the received signal whereas the channel gain ($h_{l,m}$) is independent for every symbol considered in the ISI part of the received signal. This assumption does not affect the performance as confirmed by the match with simulation results described in the next section.

It is assumed that the receiver has perfect channel state information for decoding. Hence the decision statistic at the output of the linear combiner can be written as [9]

$$\begin{bmatrix} \hat{X}_1 \\ \hat{X}_2 \end{bmatrix} = \Re \{ \Gamma^H \mathbf{r} \} = \Re \left\{ \begin{bmatrix} h_{k,1}^* & -h_{k,2} \\ h_{k,2}^* & h_{k,1} \end{bmatrix} \begin{bmatrix} r_k \\ -r_{k+1}^* \end{bmatrix} \right\} \quad (4.1-8)$$

Due to symmetry considerations of the BPSK system, it will suffice to calculate the probability of error of one of the decision statistics at the output of the linear. Therefore we choose \hat{X}_1 which is given by

$$\left[\hat{X}_1 \right] = \Re \left\{ \begin{bmatrix} h_{k,1}^* & -h_{k,2} \end{bmatrix} \begin{bmatrix} \sum_{m=1}^2 h_{k,m} b_{k,m} g_{k,m} + \sum_{m=1}^2 \sum_{\substack{l=-\infty \\ l \neq k+1}}^{\infty} h_{l,m} b_{l,m} g_{k-l,m} + n_k \\ -\sum_{m=1}^2 h_{k,m}^* b_{k+1,m} g_{k+1,m} - \sum_{m=1}^2 \sum_{\substack{l=-\infty \\ l \neq k+1}}^{\infty} h_{l,m}^* b_{l,m} g_{k-l-1,m} - n_{k+1} \end{bmatrix} \right\} \quad (4.1-9)$$

Notice that conjugation does not affect binary bits, the pulse shaping function, and noise which are real valued. Now decoding the OSTBC block transmitted at k^{th} symbol time duration; (9) becomes

$$\hat{X}_1 = \Re \left\{ \begin{aligned} & \left(|h_{k,1}|^2 g_{k,1} + |h_{k,2}|^2 g_{k+1,2} \right) b_{k,1} + \left(h_{k,1}^* h_{k,2} g_{k,1} - h_{k,2} h_{k,1}^* g_{k+1,1} \right) b_{k,2} \\ & + h_{k,1}^* \sum_{m=1}^2 \sum_{\substack{l=-\infty \\ l \neq k+1}}^{\infty} h_{l,m} b_{l,m} g_{k-l,m} + h_{k,2} \sum_{m=1}^2 \sum_{\substack{l=-\infty \\ l \neq k+1}}^{\infty} h_{l,m}^* b_{l,m} g_{k-l-1,m} + h_{k,2} n_k + h_{k,1}^* n_{k+1} \end{aligned} \right\} \quad (4.1-10)$$

For a given time offset at the receiver, on signals received from a certain transmit antenna, the values $g_{k,m}$ are deterministic. To evaluate the ABER exclusively due to pulse shaping as a result of timing offset the procedure described in the next section can be followed. In the next section we present the analysis for evaluating the bit error probability where both the effect of pulse shaping and jitter are considered simultaneously by assuming $g_{k,m}$ to be a random variable.

- Bit Error Probability Using CHF Method

Time synchronization error arises due to sampling offset at the receiver and due to jitter of the clocks at the transmitting nodes which causes the pulses to overlap at the receiver. The combined effect can be characterized in the pulse shaped received symbol output as

$$s_{l,m}(t) = \sum_{l=-\infty}^{\infty} b_l g(t - lT - \tau_{l,m}) \quad (4.1-11)$$

where $\tau_{l,m}$ can be modeled as a random variable uniformly distributed on $U\left[\frac{-\Delta T}{2}, \frac{\Delta T}{2}\right]$ and $0 \leq \Delta T < T$. Hence all $g_{l,m}$ in (4.1-10) are also random variables whose outcome depends on $\tau_{l,m}$. Now assume that $b_{k,1} = -1$ was transmitted. Equation (4.1-10) can now be written as

$$\begin{aligned} \hat{X}_1 &= -\left(|h_{k,1}|^2 g_{k,1} + |h_{k,2}|^2 g_{k+1,2} \right) + \Re \left\{ \left(h_{k,1}^* h_{k,2} g_{k,1} - h_{k,2} h_{k,1}^* g_{k+1,1} \right) b_{k,2} \right\} \\ &+ \Re \left\{ h_{k,1}^* \sum_{m=1}^2 \sum_{\substack{l=-\infty \\ l \neq k+1}}^{\infty} h_{l,m} b_{l,m} g_{k-l,m} \right\} + \Re \left\{ h_{k,2} \sum_{m=1}^2 \sum_{\substack{l=-\infty \\ l \neq k+1}}^{\infty} h_{l,m}^* b_{l,m} g_{k-l-1,m} \right\} + \Re \{ h_{k,2} n_k + h_{k,1}^* n_{k+1} \} \\ &= -A + Z_1 + Z_2 + Z_3 + \eta \end{aligned} \quad (4.1-12)$$

where A is the contribution from desired symbol; Z_1 , Z_2 , and Z_3 correspond to the interference from adjacent symbols and cross signal interference; and η corresponds to the receiver noise at the decoder output.

The average probability of error under BPSK modulation P_e can be written as

$$P_e = \Pr(\hat{X}_1 > 0 | b_{k,1} = -1) \quad (4.1-13)$$

In (4.1-12), η is a Gaussian random variable whose mean is zero and variance is given by

$$\sigma_\eta = \frac{\sum_{m=1}^2 |h_{k,m}|^2}{2} \quad (4.1-14)$$

η can now be expressed as function of a zero mean unit variance Gaussian random variable n given by

$$\eta = \sigma_\eta n \quad (4.1-15)$$

Notice that Z_1 , Z_2 and Z_3 are random variables which are formed by a linear combination of other independent random variables due to the fast fading nature assumed for ISI terms. Now the average probability of bit error conditioned on A, Z_1, Z_2 and Z_3 can be written as

$$\begin{aligned} P_{e|A,Z_1,Z_2,Z_3} &= \Pr(-A + Z_1 + Z_2 + Z_3 + \eta > 0) = \Pr(\eta > A - Z_1 - Z_2 - Z_3) \\ &= \Pr\left(n > \frac{A - Z_1 - Z_2 - Z_3}{\sigma_\eta}\right) \end{aligned} \quad (4.1-16)$$

Using $Q(x)$ which is the tail probability of a zero-mean, unit variance Gaussian random variable (GRV) that exceeds x equation (4.1-16) can be written as

$$P_{e|A,Z_1,Z_2,Z_3} = Q\left(\frac{A - Z_1 - Z_2 - Z_3}{\sigma_\eta}\right) \quad (4.1-17)$$

Now we examine each of the terms inside the parentheses of equation (17). The first term can be written as

$$\frac{A}{\sigma_n} = \frac{\alpha_{k,1}^2 g_{k,1} + \alpha_{2,1}^2 g_{k+1,2}}{\sqrt{\alpha_{k,1}^2 + \alpha_{2,1}^2}} \approx \sqrt{\alpha_{k,1}^2 + \alpha_{2,1}^2} \quad (4.1-18)$$

where $\alpha_{k,m}$ is the random amplitude process representing the received channel envelope. The approximation in (4.1-18) is made to make the analysis simpler and becomes equal when the desired symbols are sampled at the right time instant. However, the analysis can still be performed without the approximation for perfect sampling as will be clear when we discuss the derivation using characteristic function method. The above approximation however does not affect on the ABER results.

The second term can be written as

$$\frac{Z_1}{\sigma_n} = \frac{(\alpha_{k,1} \alpha_{k,2} g_{k,2} - \alpha_{k,2} \alpha_{k,1} g_{k+1,1}) b_{k,2} \cos(\theta_{k,1} - \theta_{k,2})}{\sqrt{\alpha_{k,1}^2 + \alpha_{k,2}^2}} \approx 0 \quad (4.1-19)$$

where $\theta_{k,m}$ is the random phase associated with the fading process which is considered to be uniformly distributed between $[-\pi, \pi]$. The approximation holds when $g_{k,2} - g_{k+1,1} \approx 0$. The contribution of this ISI term to the error is very small and can be ignored for practical purposes. However the exact analysis can still include the above term at additional cost of computation.

The third term can be expressed as

$$\frac{Z_2}{\sigma_n} = \frac{\alpha_{k,1} \sum_{m=1}^2 \sum_{\substack{l=-\infty \\ l \neq k}}^{\infty} \alpha_{k,m} \cos(\theta_{l,m} - \theta_{k,1}) b_{l,m} g_{k-l,m}}{\sqrt{\alpha_{k,1}^2 + \alpha_{k,2}^2}} = \frac{\alpha_{k,1}}{\sqrt{\alpha_{k,1}^2 + \alpha_{k,2}^2}} I_2 \quad (4.1-20)$$

where I_2 is a random variable which is the result of the sum of the product of real independent random variables. The fourth can be similarly written as

$$\frac{Z_3}{\sigma_n} = \frac{\alpha_{k,2} \sum_{m=1}^2 \sum_{\substack{l=-\infty \\ l \neq k}}^{\infty} \alpha_{k,m} \cos(\theta_{l,m} - \theta_{k,1}) b_{l,m} g_{k-l,m}}{\sqrt{\alpha_{k,1}^2 + \alpha_{k,2}^2}} = \frac{\alpha_{k,2}}{\sqrt{\alpha_{k,1}^2 + \alpha_{k,2}^2}} I_3 \quad (4.1-21)$$

where I_3 is similar to I_2 . Examining the four terms the random variables within each of the terms are real and independent. The four terms are correlated to each other through the random variables $\alpha_{k,1}$ and $\alpha_{k,2}$. Ignoring the second term (4.1-19), the conditional bit error probability (4.1-17) can now be written as

$$P_{e|\alpha_{k,1}, \alpha_{k,2}, I_2, I_3} = Q\left(\frac{A - Z_2 - Z_3}{\sigma_\eta}\right) \quad (4.1-22)$$

Invoking Gil-Pelaez inversion theorem and using the CHF of Gaussian random variable (GRV) the expression for $Q(x)$ can be written as [10]

$$Q(x) = \frac{1}{2} + \frac{1}{\pi} \int_0^\infty \frac{1}{t} e^{-t^2/2} \Im\{e^{-jtx}\} dt \quad (4.1-23)$$

Averaging (4.1-23) over the random variables identified in (4.1-22) the actual ABER can now be evaluated as

$$\begin{aligned} P_e &= \int_0^\infty f_{\alpha_{k,1}} \int_0^\infty f_{\alpha_{k,2}} \int_{-\infty}^\infty f_{I_2} \int_{-\infty}^\infty f_{I_3} Q\left(\frac{A - Z_2 - Z_3}{\sigma_\eta}\right) dt \\ &= \frac{1}{2} + \frac{1}{\pi} \int_0^\infty \frac{1}{t} e^{-t^2/2} \Im\left(\int_0^\infty f_{\alpha_{k,1}} \int_0^\infty f_{\alpha_{k,2}} \int_{-\infty}^\infty f_{I_2} \int_{-\infty}^\infty f_{I_3} e^{-jt\left(\frac{A - Z_2 - Z_3}{\sigma_\eta}\right)} dI_2 dI_3 d\alpha_{k,2} d\alpha_{k,1} dt\right) \\ &= \frac{1}{2} + \frac{1}{\pi} \int_0^\infty \frac{1}{t} e^{-t^2/2} \Im\left(\int_0^\infty f_{\alpha_{k,1}} \int_0^\infty f_{\alpha_{k,2}} e^{-jt\left(\frac{A}{\sigma_\eta}\right)} \phi_{I_2}\left(\frac{Z_2}{\sigma_\eta}\right) \phi_{I_3}\left(\frac{Z_3}{\sigma_\eta}\right) d\alpha_{k,2} d\alpha_{k,1} dt\right) \end{aligned} \quad (4.1-24)$$

where $\phi_{I_2}(t)$ and $\phi_{I_3}(t)$ are CHF's of I_2 and I_3 respectively. The expression in (4.1-24) can be easily evaluated using numerical integration using Gauss-Chebyshev quadrature method for all the known fading distributions. It can be seen that the above expression allows the flexibility to analyze distributed links with different families of fading distributions as well as links with different average SNRs. Next we provide the computation of $\phi_{I_2}(t)$ and $\phi_{I_3}(t)$ for generalized fading distribution.

- Computing CHF

The following theorem regarding CHF involving the product of two real and independent random variables will be applied to derive the required CHF.

Theorem: Let X and Y be independent real random variables with characteristic functions ϕ and ψ respectively. The product XY has characteristic function given by

Proof:

$$E\{e^{j\mu XY}\} = E_Y\{\phi_X(tY)\} = E_X\{\psi_Y(tX)\} \quad (4.1-25)$$

$$E\{e^{j\mu XY}\} = \int_{-\infty}^{\infty} E_X\{e^{j\mu Xy} | Y=y\} f_Y(y) dy = E_X\left\{\int_{-\infty}^{\infty} e^{j\mu Xy} f_Y(y) dy\right\} = E_X\{\psi_Y(tX)\} \quad (4.1-26)$$

To CHF $\phi_{I_2}(t)$ can now be expressed as

$$\phi_{I_2}(t) = \phi_{\sum_{m=1}^2 \sum_{\substack{l=-p \\ l \neq k}}^p \alpha_{k,m} \cos(\theta'_{l,m}) b_{l,m} g_{k-l,m}}(t) = \prod_{m=1}^2 \prod_{\substack{l=-p \\ l \neq 0}}^p E_{\tau_{l,m}} \left\{ E_{b_{l,m}} \left\{ \phi_{\alpha_{k,m} \cos(\theta'_{l,m})}(tb_{l,m} g_{l,m}) \right\} \right\} \quad (4.1-27)$$

where $\theta'_{l,m} = \theta_{l,m} - \theta_{k,l}$ and the ISI is restricted to $2p$ adjacent symbols. The CHF $\phi_{\alpha_{k,m} \cos(\theta'_{l,m})}(t)$ can be evaluated using [13 Appendix A eq (36)-(42)]. The CHF in [13] have only been evaluated for Nakagami-m distribution. Table 4.1-1 shows the closed form expressions for CHF $\phi_{\alpha_{k,m} \cos(\theta'_{l,m})}(t)$ which are also derived for Rice and Nakagami-q distributions by applying [14 eq (6.333,4)] and [14 eq(6.651,6)] respectively to [13 Appendix A eq (42)]. For the special case of Weibull distribution the CHF $\phi_{\alpha_{k,m} \cos(\theta'_{l,m})}(t)$ will need to be calculated as $E_{\theta'_{l,m}} \left\{ \phi_{\alpha_{k,m}}(t \cos(\theta'_{l,m})) \right\}$. For BPSK modulation and uniform distribution of timing error over

$\left[\frac{-\Delta T}{2}, \frac{\Delta T}{2} \right]$ the expression in (29) can be written as

$$\phi_{I_2}(t) = \prod_{m=1}^2 \prod_{\substack{l=-p \\ l \neq 0}}^p \frac{1}{\Delta T} \int_{-\Delta T/2}^{\Delta T/2} \left[0.5 \phi_{\alpha_{k,m} \cos(\theta'_{l,m})}(-tg_{l,m}) + 0.5 \phi_{\alpha_{k,m} \cos(\theta'_{l,m})}(-tg_{l,m}) \right] d\tau_{l,m} \quad (4.1-28)$$

$\phi_{I_1}(t)$ can be computed in a similar manner resulting in an identical expression. Notice that these expressions for CHF's can accommodate distributed links with non-identical fading distributions as well as non identical channel gains.

In the next section we verify the analysis by comparing the numerical results with simulation for Rayleigh fading case and then discuss the performance of DOSTBC under different fading distributions and pulse shapes.

• Numerical Results

Analysis and simulation of a 2x1 distributed OSTBC system discussed in section III were performed with both links under flat Rayleigh fading channel. Figure 4.1-2 shows the results on ABER versus total average received SNR for increasing values of timing error which is uniformly distributed between $\left[\frac{-\Delta T}{2}, \frac{\Delta T}{2} \right]$. The average channel received SNR on each link is balanced

i.e.; the total received SNR is equally distributed across both links. Raised cosine pulse shaping is employed with a roll-off factor of $\alpha = 0.22$. As the timing error increases the ABER degrades rapidly. The performance under time synchronization is acceptable when the timing error is less than $\frac{\Delta T}{2} = 0.1T$. In terms of clock stability requirement, this corresponds to 50,000 ppm which is much higher than the stability of cheaper clocks available off-the-shelf. In terms of differential propagation delay due to transmitter placement this is equivalent to a distance of 1500m at a baud rate of 10 MHz. Hence, it can be said that implementation of a distributed OSTBC system is practically feasible under the above constraints for timing error. The figure also shows that the numerical results corresponding to analysis presented in section III matches perfectly with simulation. This validates our analytical approach. However it should be mentioned that at higher SNRs the numerical integration needs to be performed over higher number of points for greater accuracy.

Figure 4.1-3 shows the performance of DOSTBC when the links are unbalanced for different values of timing error. The distribution of average channel SNRs over each link is 0.75 and 0.25 times the total average received SNR. Both the links experience Rayleigh fading. Comparing corresponding performance with the balanced case it can be observed that the balanced case outperforms the unbalanced case by 2 dB. This means that when the channels experience fading corresponding to the same family of fading distribution optimum performance is achieved when the links are balanced.

In Figure 4.1-4, we plot the ABER performance of DOSTBC for the case where the two cooperative links undergo fading from two different families of distribution. This allows for evaluation of the effect of fading severity on the ISI. Specifically we chose a case where one of the links is lightly faded (Nakagami-m with $m = 6$) and the other link with a different family of distribution corresponding to a different fading severity. As reference two cases where both links undergo Rayleigh and Nakagami-m ($m=6$) respectively are also plotted. In all the cases

considered the timing error is uniformly distributed between $\left[\frac{-\Delta T}{2}, \frac{\Delta T}{2} \right]$ where $\frac{\Delta T}{2} = 0.2T$ and

the average channel SNRs are equally distributed. The performance is the best when both links have Nakagami-m fading distribution. The performance is the worst when the both links experience Rayleigh fading. Comparing the performance for the case where the links have different fading distribution the ordering from best to worst is given by Rice with K-factor at 4.7 dB ($K=3$) followed by Rayleigh and then by Nakagami-q with $b = 0.75$. From this observation it is evident that an increase in the effect of ISI is observed when the links under pulse shaping experience more severe fading. This is contrary to the intuition that a line of sight link with the same average power would cause more ISI.

One plausible explanation is given in [15] and also briefly explained in [13]. It is shown in [15] that when the noise due to interference is Gaussian and the probability of error is a Q -function that is concave up larger interference always results in higher probability of error. However, if the complementary function for calculating the probability of error is concave down, then the reverse may be true. It was further predicted that this will be caused when the noise has a PDF with more than one bump or in communication system with a different signaling and detection strategy. Now if we consider the case where AWGN is absent and only ISI is present, then the complementary function is the Laplace inverse transform of CHF given in (4.1-28) which in turn depends on $\phi_{\alpha_{k,m} \cos(\theta'_{l,m})}(t)$. [13 Fig.1] gives the PDF of $\phi_{\alpha_{k,m} \cos(\theta'_{l,m})}(t)$ for different fading

severity indexes for Nakagami-m fading distribution. It can clearly be seen that as the fading severity decreases for increasing values of m , the PDF has multiple bumps confirming the behavior of ABER performance under ISI for less severely faded links.

Figure 4.1-5 shows the performance of two DOSTBC links under Nakagami-m ($m=6$) and Rayleigh fading distributions respectively under different average channel SNR distribution and timing error uniformly distributed between $\left[-\frac{\Delta T}{2}, \frac{\Delta T}{2}\right]$ where $\frac{\Delta T}{2} = 0.2T$. Three cases are considered. In the first case, the Rayleigh faded link has less average channel SNR (0.25 time the total channel SNR) than the Nakagami-m faded link (0.75 time the total channel SNR). The second case has a balanced distribution and the third case is for the distribution that is the reverse of case one. It can be seen that the best performance is observed when the Nakagami-m faded link has higher average channel gain than the Rayleigh faded link. This scenario performs even better than the balanced case. This is in contrast to the results in Fig. 4.1-3 where for the same type of distribution balanced links resulted in optimum performance. This is important because power allocation for distributed transmission for optimum performance under timing error will also require the type of channel to be taken into consideration. The above results also confirm that higher ISI is observed for more severely faded channel.

In Figure 4.1-6 we show a comparison of the performance of different pulse shapes. Both links of DOSTBC system are considered to be balanced and experiencing Rayleigh fading. Three pulse shapes raised cosine (RC), better than raised cosine (BTRC) [13] and Gaussian $g(t) = \exp\left(-(8t/5T)^2\right)$ are considered. The timing error is uniformly distributed between $\left[-\frac{\Delta T}{2}, \frac{\Delta T}{2}\right]$ where $\frac{\Delta T}{2} = 0.2T$. It is observed that BTRC performs better than Nyquist RC pulse. The Gaussian pulse performs the best.

• References

- [1] J.N. Laneman, and G.W. Wornell, "Distributed space-time-coded protocols for exploiting cooperative diversity in wireless networks," *IEEE Trans Inform. Theory*, vol. 49, no. 10, pp. 2415 – 2425, Oct. 2003.
- [2] Shuguang Cui, A.J. Goldsmith, A. Bahai, "Energy-efficiency of MIMO and cooperative MIMO techniques in sensor networks," *IEEE JSAC*, vol. 22, pp.1089 – 1098, Aug. 2004.
- [3] P.A. Anghel, M. Kaveh, "Exact symbol error probability of a Cooperative network in a Rayleigh-fading environment," *IEEE Trans. Wireless Commun*, vol. 3, pp. 1416 – 1421 Sept. 2004.
- [4] A. Ribeiro, X. Cai, G.B. Giannakis, "Symbol Error Probabilities for General Cooperative Links," *IEEE Trans. Wireless Commun.*, vol. 4, pp. 1264 – 1273, May 2005.
- [5] S. Jagannathan, H. Aghajan, A. Goldsmith, "The effect of time synchronization errors on the performance of cooperative MISO systems," *IEEE GlobeCom*, pp.102 - 107, Nov 2004.
- [6] Yan Mei, Yingbo Hua, A. Swami, B. Daneshrad, "Combating Synchronization Errors in Cooperative Relays," *ICASSP*, vol. 3, pp. 369 – 372, Mar 2005.

- [7] A. Annamalai, C. Tellambura, V.K. Bhargava, "Equal-gain diversity receiver performance in wireless channels," *IEEE Trans. Commun.*, vol. 48, pp. 1732 – 1745, Oct. 2000.
- [8] S. Alamouti, "A simple transmitter diversity scheme for wireless communications," *IEEE Journal on Selected Areas in Communications*, vol. 16, pp. 1451 –1458, Oct. 1998.
- [9] Chunjun Gao, A.M. Haimovich, Debang Lao, "Bit error probability for space-time block code with coherent and differential detection, " *IEEE VTC 2002-Fall*, vol. 1, pp. 410 – 414, Sept. 2002.
- [10] C. Tellambura, A. Annamalai, "Derivation of Craig's formula for Gaussian probability function," *IEEE Electronics Letters*, vol. 35, pp.1424 - 1425 , Aug. 1999.
- [11] J. Abate, P. P. Valkó, "Multi-precision Laplace transform inversion," *International Journal for Numerical Methods in Engineering*, vol. 60, no. 5, pp. 979-993, May 2004.
- [12] A. Annamalai, C. Tellambura, V.K. Bhargava, "A general method for calculating error probabilities over fading channels," *IEEE Trans. Commun.*, vol. 53, pp. 841 – 852, May 2005.
- [13] N. C. Beaulieu and J. Cheng, "Precise error rate analysis of bandwidth efficient BPSK in Nakagami fading and cochannel interference," *IEEE Trans. Commun.*, vol. 52, pp. 149–158, Jan. 2004.
- [14] I. S. Gradshteyn and I. M. Ryzhik, *Table of Integrals, Series and Products*, San Diego, CA: Academic, 1995.
- [15] Y.-C. Jenq, "Does a Larger Intersymbol Interference Result in a Higher Probability of Error?," *IEEE Trans. Commun.*, vol. 28, pp. 1771 – 1773, Sep 1980.

Table 4.1-1 CHF of $\phi_{\alpha\cos(\theta)}(t)$ for several fading channel models

Channel Model	CHF $\phi_{\alpha\cos(\theta)}(t)$
Rice ($K \geq 0$)	$\exp\left(\frac{-\bar{\gamma}t^2}{4(1+K)}\right) J_0\left(\sqrt{\frac{K\bar{\gamma}}{K+1}}t\right)$ where $\bar{\gamma} = E\{\alpha^2\}$
Nakagami-m [13]	${}_1F_1\left(m;1;\frac{-\bar{\gamma}}{4m}t^2\right)$
Nakagami-q $-1 < b < 1$	$\exp\left(\frac{-\bar{\gamma}}{4}t^2\right) I_0\left(\frac{\bar{\gamma}}{4}bt^2\right)$

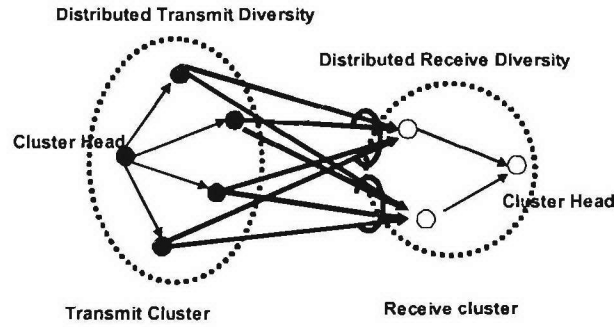


Figure 4.1-1 Cooperative communication between transmit cluster and receive cluster of wireless nodes using distributed transmit and receive diversity schemes.

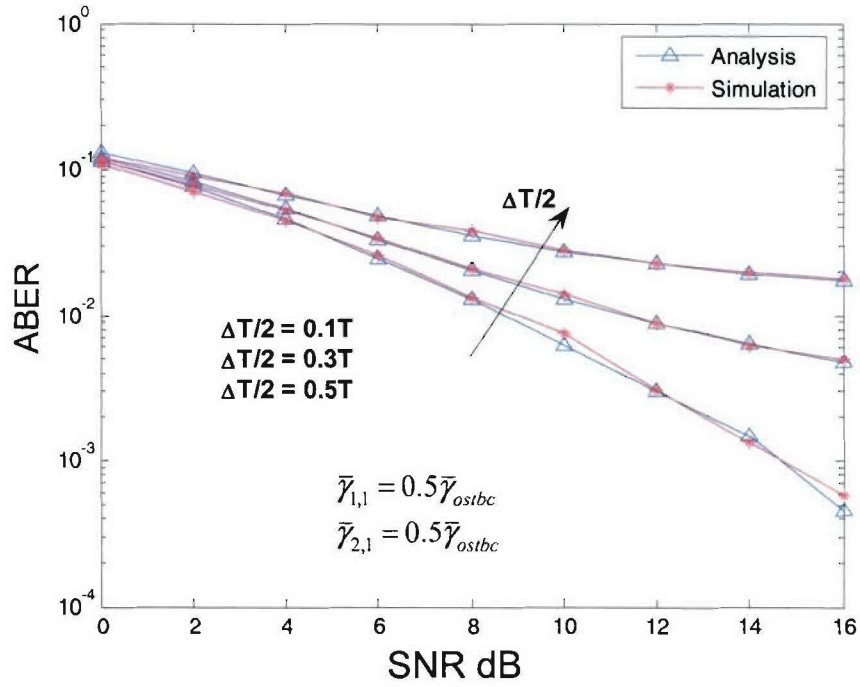


Figure 4.1-2 Analysis and simulation of ABER for 2x1 distributed OSTBC scheme under balanced Rayleigh fading channels with RC pulse shaping ($a = 0.22$).

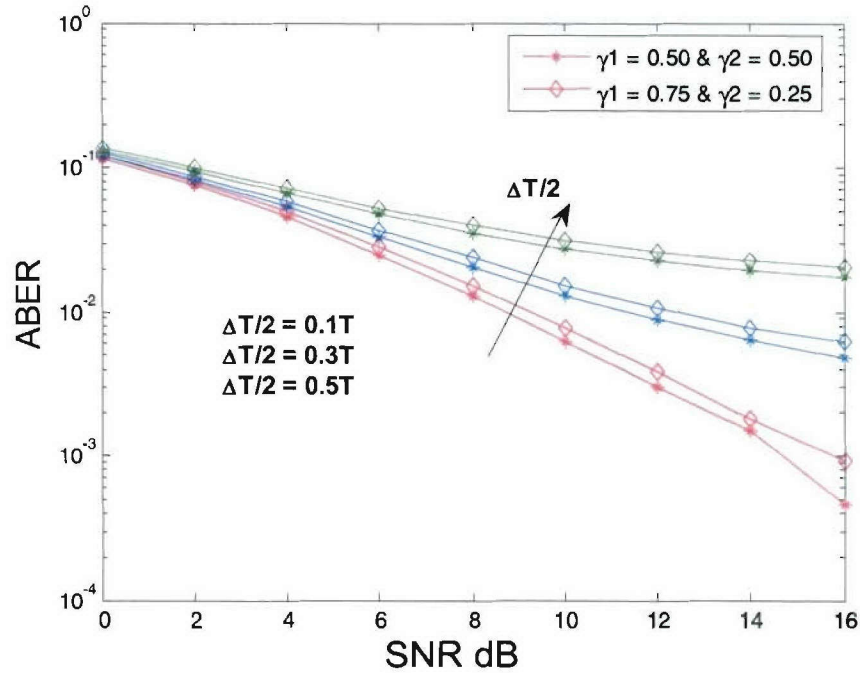


Figure 4.1-3 ABER for 2x1 distributed OSTBC scheme under unbalanced Rayleigh fading channels with RC pulse shaping ($a = 0.22$).

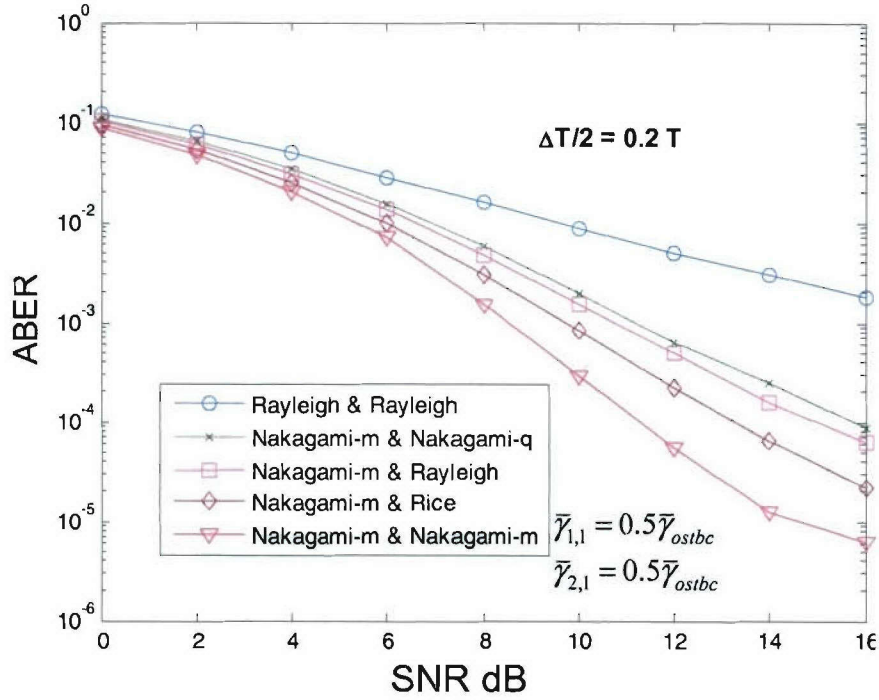


Figure 4.1-4 ABER for 2x1 distributed OSTBC scheme under balanced links with same and different families of fading distribution on both links with RC pulse shaping ($\alpha=0.22$) (Nakagami-m ($m=6$), Rice $K = 3$, Nakagami-q $b=0.75$).

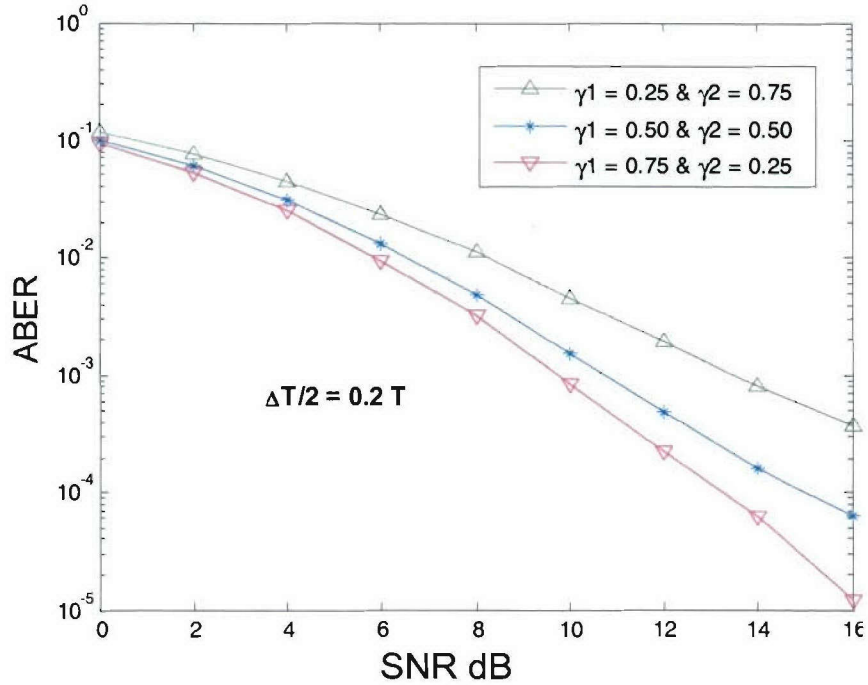


Figure 4.1-5 ABER for 2x1 distributed OSTBC scheme with first link under Nakagami-m ($m=6$) and second link under Rayleigh fading and varying distributions of average channel SNRs per link with RC pulse shaping ($\alpha = 0.22$).

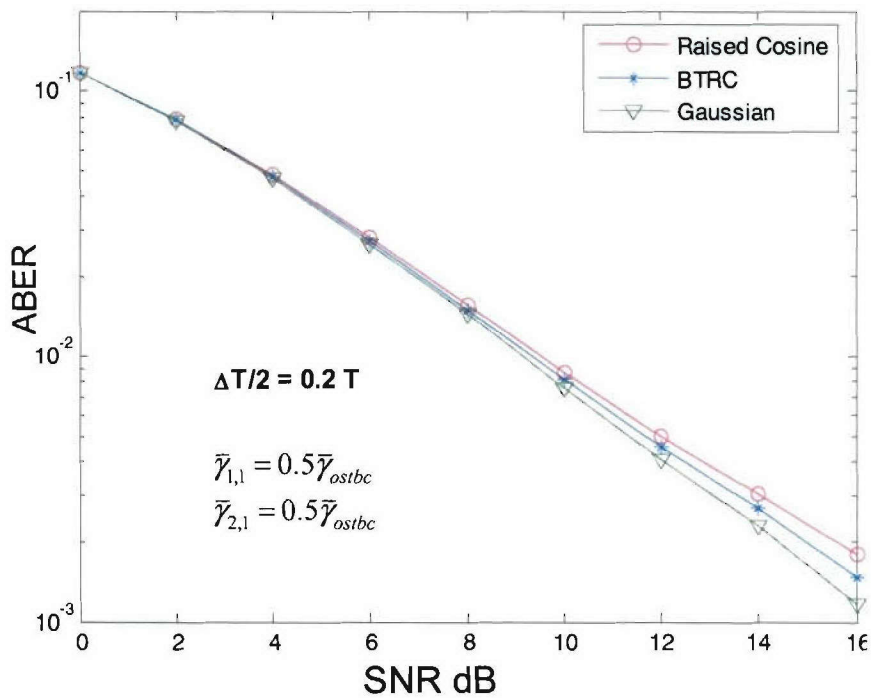


Figure 4.1-6 Comparison of ABER performance of distributed OSTBC with raised cosine and BTRC and Gaussian pulse shapes ($\alpha = 0.22$).

Schedule:

- January-Summer 2005
 - Develop UWB MIMO Algorithms
- Summer-Fall 2005
 - Simulate performance of UWB MIMO Algorithms
- Spring 2006
 - Begin Work on testing algorithms on Advanced SDR Receiver

Personnel:

Ramesh C. Palat

4.2 TIP#2 Close-in UWB wireless application to Sea Basing

Task objective: The objective of this subtask is to develop algorithms that allow UWB technology to provide precision position location, precision ranging, and imaging. With a low duty cycle and wide bandwidth, UWB is naturally suitable to radar and ranging applications. As the time duration of a pulse decreases, it provides finer resolution of reflected signals, such that the system can resolve distances with sub-centimeter accuracy using simple signal processing algorithms.

Accomplishments during reporting period: Continuing from the last quarter, the assembly of all required components for the demo was finished, the means of communications with the crane's control system was determined, and a demo was successfully carried out at Buruss 115.

The Demonstration

The communication with the crane's control system was determined to be an 8bit parallel port, which indicates that the ranging software could only give one update of 256 different values; therefore, the maximum range of the system was set to 255 mm, which is still a realistic range that translates to a range of about 6m (20ft) for the real system.

Update Rate

The update rate of the system was about of 15 updates/sec for one range and about of 3 updates/sec for the four sides ranging. The update rate was limited by the receiver used, the Tektronix CSA8000B, which was not able to clear and reacquire new data fast enough as a result of changing transmitting sides on the crate (as described in the previous report). Partially due to the update rate limitations, the ability of the system to obtain both range and orientation information was demonstrated without interaction with the crane.

Equipment Photos

Figure 4.2-1 shows the assembled crate with the antennas both the crate and the antennas were built by Randall Nealy, staff engineer of the VT Antenna group. The equipment setup is shown in Fig. 4.2-2. On the left, the crate is shown to be hanging above the shaker; on top of the shaker there is an aluminum foil covered carton, the reasons for the aluminum foil are that the shaker is full of holes, and the conductive plate ensures strong reflected signals. On the right, the pulse generator, the receiver, and the laptop used to run do the signal processing are shown.

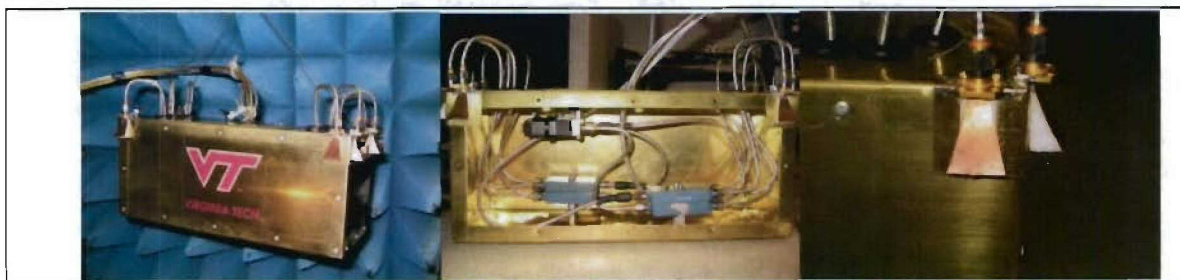


Figure 4.2-1 The Crate: outside, inside, and the antennas.

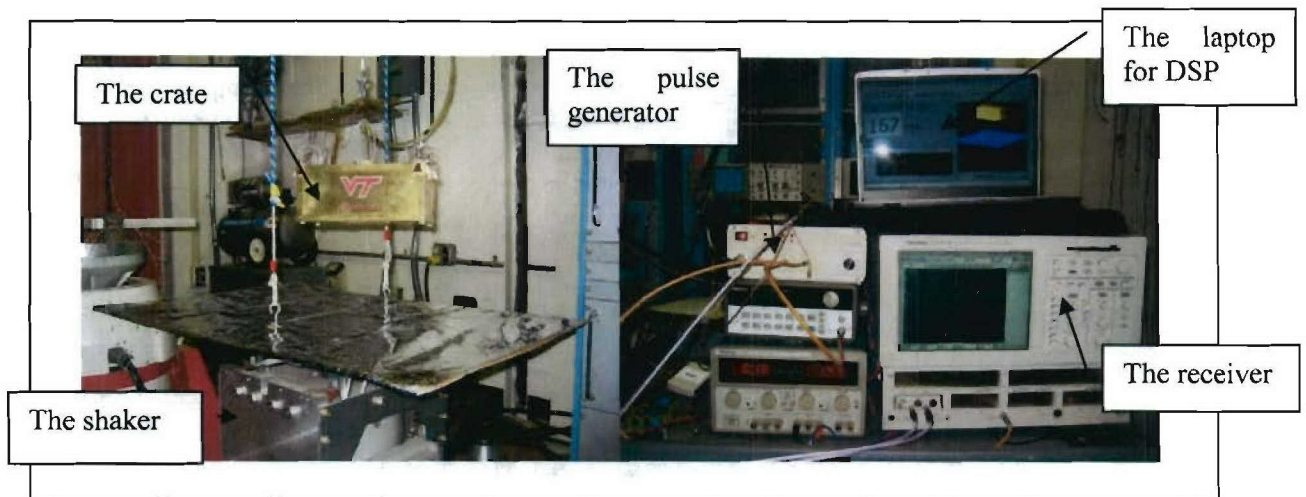


Figure 4.2-2 The equipment setup.

Application Screen Shots

Figure 4.2-3 shows sample screen shots from the UWB ranging application which was written on Labview. At the top left corner a screen shot of the single side range application is shown, and the rest of the screen shots are from the four sides of ranging application. As can be seen from the pictures, both programs provided both numeric and visual (3D) representation of the data, including the four ranges version which demonstrated the orientation of the floor below the crate.



Figure 4.2-3 Sample screen shots.

Automated Landing

The ranging setup was able to provide 1-mm resolution to the crane control system which was able to successfully land the crate to the oscillating floor with minimum impact. The range output to the crane control system is shown in Figure 4.2-4. In the figure there are three main regions: the oscillating region, the during landing region, and the landed region.

The salient points used in the ranging software follow:

- **Coupling elimination:** Because the antennas were very close to each other, the receive antennas were receiving a strong direct signal from the transmit antennas. This signal was recorded during the calibration phase of the program, and was subtracted from the received signal, thus eliminating it. Furthermore, it was found useful to continuously estimating that signal because it was observed to shift slightly with time. Coupling will not be of significant strength in the real application.
- **Pulse Tracking:** To enhance the detection process, when a reflected pulse was found that met the detection criteria, the program tracks pulses of subsequent detections by first looking at the last observed location of the pulse. If a pulse meeting the detection criteria is not found within that limited region, the program examines the whole received window again for detection.
- **Sudden Jumps Rejection:** Occasionally, the detector momentarily might assume detection far from the actual pulse's location and then return to the correct reading. For this reason, the program compares the output value with a couple of previous values and a couple of future values (this introduces a small delay of two updates) and if the value is found to be significantly different from the average of those values, that value was replaced by their average.

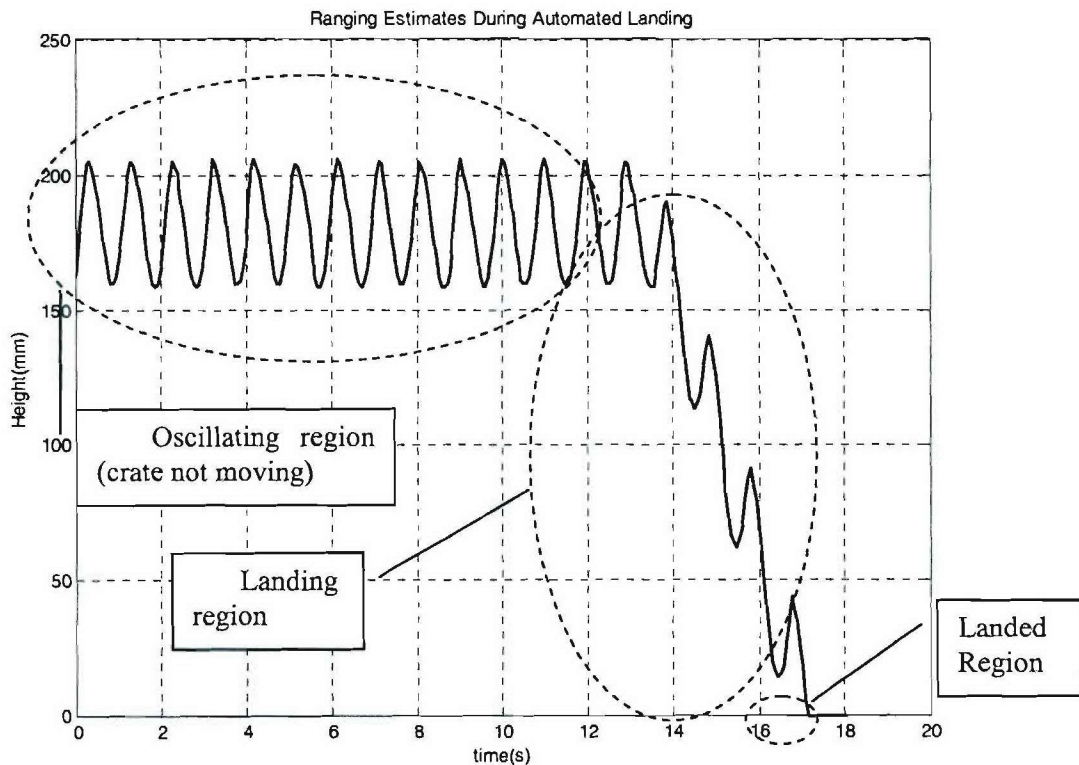


Figure 4.2-4 Ranging estimates during automated landing to the shaker (oscillating at 1Hz).

Future Development

The outcomes of the full system demo will be evaluated and future development of the project will be decided. Initial thoughts include characterizing the UWB reflection properties of various materials for ranging purposes and investigating methods for a robust ranging estimation in the environment of the real system.

Schedule:

- January-Summer 2005
 - Begin algorithm development
 - Test algorithms using the simple setups discussed above
- Summer-Fall 2005
 - Integrate ranging system into the crane hardware
 - Evaluate performance of position location algorithms in real-world environments
- January-Summer 2006
 - Finalize 3-D Ranging solution
 - Demonstrate passive and active position location system in laboratory environment.

Personnel:

Haris Volos – Ranging Algorithm Development and implementation

4.3 TIP#3 Secure Ad Hoc Networks

4.3.1 Project Description

The testing and demonstration of secure ad hoc networks involves integration and testing along three related tracks. Each of these will lead to a separate demonstration (or coupled set of demonstrations) using a common hardware and software base, as implemented in our test bed network (see discussion of Task 2.1).

- (a) Activities within Task 2.1 (Ad Hoc Networks) that support core network services will be integrated, tested, and demonstrated. Capabilities to be integrated include policy-based quality of service (QoS), security based on distributed certificate authorities (DCAs) for key management and trust grading, and mobile ad hoc network (MANET) routing support for QoS and security functionality and as a means to demonstrate cross-layer design. Cross-layer design techniques from Task 2.4 will be reviewed and incorporated as appropriate. Capabilities will be shown operating with Internet Protocol version 4 (IPv4) and, where feasible within the level of effort possible, Internet Protocol version 6 (IPv6).
- (b) A cross-layer approach to transporting multiple description (MD) video in ad hoc networks, also a part of Task 2.1, will be integrated, tested, and demonstrated. This task will utilize application-level routing to use application-specific optimal routes. It will integrate with the MANET routing effort of Task 2.1, e.g., with Open Shortest Path First-Multiple Connected Dominating Sets (OSPF-MCDS), to utilize the topology information efficiently obtained by the MANET routing protocol.
- (c) We will integrate real-time middleware from Task 2.2 with the combined QoS, security, and routing as discussed above and as investigated in Task 2.3. Specifically, we will investigate and develop methods and mechanisms to integrate policy-based quality of service (QoS) capabilities at the network level, and perhaps at the link layer, with real-time services offered by middleware.

4.3.2 Demonstration Description

Table 4.3-1 lists the themes, components, and leaders for the three demonstrations. Demonstration (a) focuses on core network services. Demonstration (b) involves network support for a video application. Demonstration (c) relates directly to Task 2.3 and involves the integration of network services with an application based on the time-utility function real-time middleware. We will adjust plans based on results from related tasks.

The components of the different demonstrations listed in Table 4.3-1 are currently envisioned to be the same except for the application – or application plus middleware in the case of Demonstration (b) – being supported. The security, QoS, and routing components are discussed further in this report in association with Task 2.1. Note that OSPF-MCDS-MC or, more simply, OMM, is a multi-channel version of the Open Shortest Path First with Minimum Connected Dominating Sets (OSPF-MCDS) MANET routing protocol. OLSR-MC is a multi-channel version of the Optimized Link State Routing (OLSR) MANET routing protocol. The topology viewer (TopoView) and topology emulation tools are carried over from the previous NAVCIIT project but have been modified to support new functions in the network and to work in an IPv6 environment as described in Subsection 2.1(f). It is envisioned that additional performance

monitoring and configuration control tools will be developed as part of Subtask 2.1(e) and used in the demonstrations.

Table 4.3-1 Demonstration Components and Leaders for the Three Demonstrations

Demonstration	Key Components	Leaders
a) Core network services	<ul style="list-style-type: none"> • Security and key management system • Policy-based quality of service • OSPF-MCDS-MC and/or OLSR-MC routing • TopoView network monitoring • Performance monitoring tools • Topology emulation 	<ul style="list-style-type: none"> • Scott Midkiff • Luiz DaSilva
b) Cross-layer approach to MD video routing	<ul style="list-style-type: none"> • OSPF-MCDS and/or OLSR routing • TopoView network monitoring • Performance monitoring tools • Topology emulation 	<ul style="list-style-type: none"> • Tom Hou • Scott Midkiff
c) Real-time middleware in an ad hoc network	<ul style="list-style-type: none"> • Real-time middleware • Security and key management system • Policy-based quality of service • OSPF-MCDS-MC and/or OLSR-MC routing • TopoView network monitoring • Performance monitoring tools • Topology emulation 	<ul style="list-style-type: none"> • Scott Midkiff • Luiz DaSilva • Binoy Ravindran

4.3.3 Cooperative AWINN Elements

This test and demonstration requires the inputs from AWINN tasks as specified in Table 4.3-2.

Table 4.3-2 Inputs from Cooperative AWINN Elements

Task (Subtask)	Inputs
2.1(a)	Prototype implementation of a policy-based QoS scheme
2.1(b)	Prototype implementation of MANET security and key management scheme
2.1(c)	Optimized prototype implementation of a MANET routing, specifically OSPF-MCDS-MC and/or OLSR-MC
2.1(f)	Performance monitoring tools; enhanced TopoView; enhanced topology emulation
2.1(d)	Video sensor application and test bed components
2.2	Real-time middleware
2.4	Cross-layer optimization elements that can be integrated into the test bed for testing and demonstration purposes.

4.3.4 Cooperative Non-AWINN Elements

At this time, no non-AWINN components are required (except for tools and equipment carried over from the NAVCIITI project).

4.3.5 Schedule of Activities

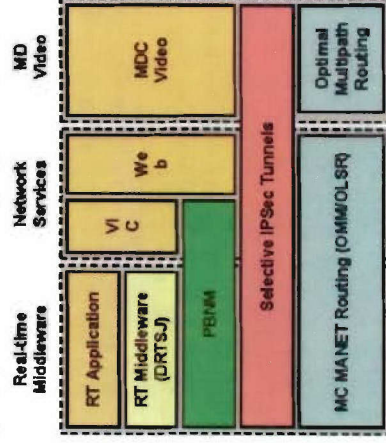
A general schedule listing major milestones is provided in Table 4.3-3. Note that the schedule is divided into four phases. The emphasis of Phase I was on core network services of Demonstration (a) running with IPv4 and, as much as possible, with IPv6. During Phase II, the emphasis was on core network services of Demonstration (a) running with both IPv4 and IPv6. Both Phases I and II have been completed and were successfully demonstrated on December 8, 2005. During Phase III, the emphasis is on integration of the MD video and real-time applications of Demonstrations (b) and (c), respectively. In Phase IV, the emphasis is on final demonstration of the MD video and real-time applications of Demonstrations (b) and (c), respectively.

Table 4.3-3 Schedule of Activities

<i>Activity</i>	<i>Date</i>
Phase I: Demonstrate core services using IPv4	4Q2005
Phase II: Demonstrate core services using IPv6	4Q2005
Phase III (b): Initial MD video integration	1Q2006
Phase III (c): Initial real-time middleware integration	1Q2006
Phase IV (b): Final demonstration of MD video	2Q2006
Phase IV (c): Final demonstration of real-time middleware	2Q2006

AWINN Technical Integration Project

TIP #3: Secure Ad Networks



TIP Description

- Network services
 - Demonstrate multi-channel routing, quality of service, and security in an integrated manner
- Multiple description video
 - Demonstrate resilience of MD video in the ad hoc network
 - Demonstrate importance of cross-layer design approach for multipath routing
- Real-time middleware
 - Distributed Real-Time Specification for Java
 - Use a futuristic, notional network-centric warfare application fragment
- Demonstrations will use a test bed of wired and wireless nodes

Experiments and Demonstrations

- 9/05: Demonstrate network services with IPv4
- 12/05: Demonstrate network services with IPv6
- 3/06: Initial demonstrations of MD video and real-time middleware
- 6/06: Final demonstrations of MD video and real-time middleware

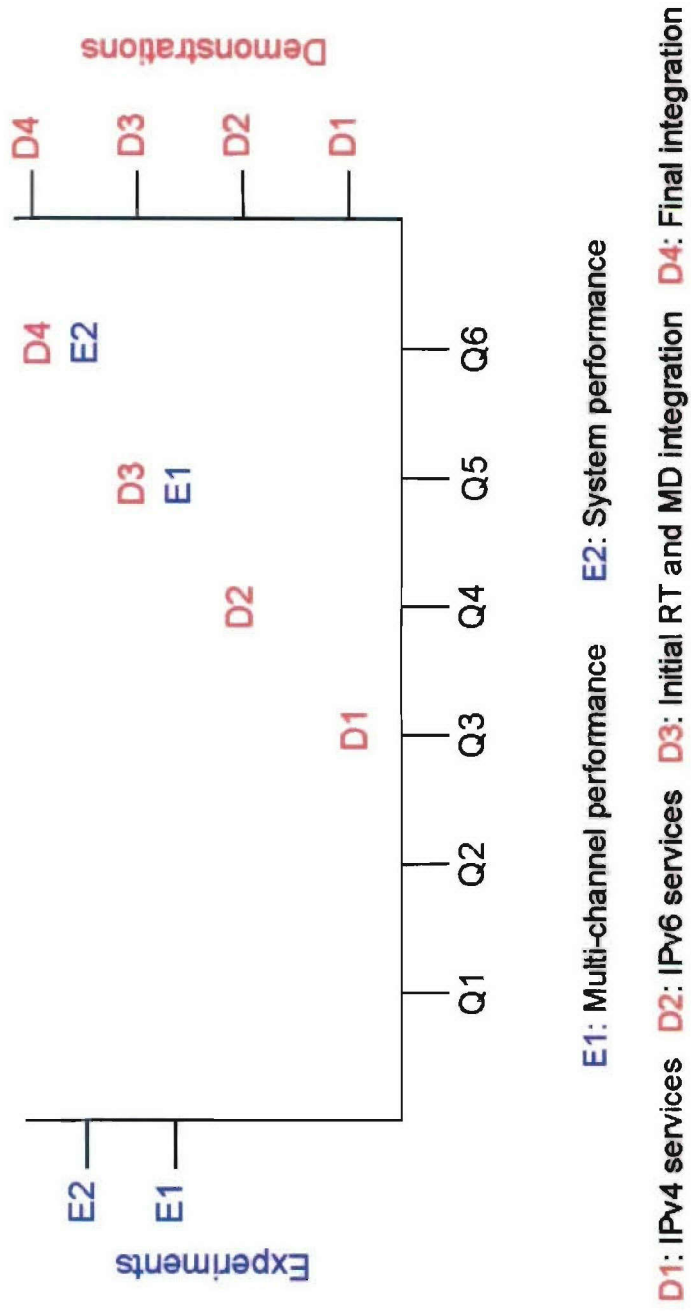
TIP Objectives

- To demonstrate adaptive, integrated core network services with multi-channel operation
- To demonstrate integrated application support for:
 - Multiple description (MD) video
 - Distributed real-time using Java

Team

Dr. S. F. Midkiff, Leader	Dr. G. Hadjichristofi
Dr. L. A. DaSilva	Dr. S. Mao
Dr. Y. T. Hou	U. Lee
Dr. B. Ravindran	W. M. de Sousa
	X. Wang

TIP #3: Secure Ad-hoc Networks



4.4 TIP#4 Integration of Close-in UWB Wireless with ESM Crane for Sea Basing Applications

Task Objective: The goal of this task is to demonstrate the usefulness of UWB in close-in communications, ship-to-ship cargo transfer for sea-basing operations, and cargo transfer from ship-to-shore and vice versa.

Organization: This task is managed by Dr. A. H. Nayfeh.

Dr. A.H. Nayfeh, Faculty

N.A. Nayfeh, GRA

Accomplishment During Reporting Period: Extensive coordination activities with the TIP#2 team have positioned us to demonstrate the usefulness of UWB systems for ship-to-ship cargo transfer. The hardware for the demonstration will be 1/24 scale model of the Navy TASC crane. Scaling down of the antennas presents a major challenge, so we have included a 1/10th scale model of the container crane as a back up.

We worked with the TIP#2 team to determine the range and update rates that need to be provided by the UWB system for the soft-landing experiment. However, according to the TIP#2 team, some of the range has to be sacrificed for the update rates due to hardware issues. Measurements taken by the UWB system will be transferred to the soft-landing system via 8 bit parallel digital I/Os. The UWB will periodically update the outputs at a given rate, while the soft-landing system will acquire the data when it needs it.

First tests of the soft-landing experiment with UWB sensors were successfully performed as a single-degree-of-freedom system with a large amplitude shaker as the target in Burruss 115. The UWB radar system designed by the MPRG provided excellent ranging information with low noise or error.

The UWB system was connected to the soft-landing routine and control system via a 8-bit parallel digital I/O interface. The ranging data was received from 0-255 mm at a sample rate of approximately 16 Hz. The system is approximately a 1:24 scale of a real crane-ship system.

The soft-landing system was demonstrated above a 900-lb shaker, which was excited sinusoidally with amplitudes ranging between 10-30 mm at 1 Hz. Scaling this excitation to a full-size ship gives a sinusoidal motion of approximately 0.25-0.75m at 0.2 Hz. This excitation is within the expected range of a ship at sea state 5.

Several runs of the experiment with the soft-landing system produced consistent impact velocities of less than 8 mm/s. While this value is hard to scale due to differences in motor and inertia, it is a promising value.

Simultaneously, we have pursued the golden opportunity of fielding the VT controller on a full-scale container crane at the Jeddah Port in Saudi Arabia. Using the contact sensors, we were able to do 30 moves per hour (more than their skilled operators can do) WITHOUT the memory feature of the SSC controller. We used a container and picked it up from a truck and took it to the sea side to a specific location (55 m distance) and then brought it back on the truck. This operation repeated and we were able to home on the container very easily. So far, we have been getting positive response from the operators. We have started training some of the operators on the system. We hope to be able to use the system to unload the next ship.

Once the UWB set up for container cranes is ready, we will field it either in Jeddah or Aqaba, Jordan.

Importance/Relevance

The proposed work has the potential of being very useful to the Navy's Transformational Sea-Basing System. The success of Sea Basing depends on the ability to sustain logistic operations with significantly reduced reliance on land bases. This requires the development of a high capacity, high reliability at-sea capability to transfer fuel, cargo, vehicle, and personnel in rough seas while underway from commercial container ships to large sea basing ships and then to smaller ships. The wave-induced motion of the crane ship can produce large pendulations of the cargo being hoisted and cause the operations to be suspended

Personnel:

N.A. Nayfeh, January, 2005-present

5. FINANCIAL REPORT

**Total Project Budget/Actual
(Equipment, Personnel and Other Direct Costs)**

